Alma Mater Studiorum · Università di Bologna

SCUOLA DI SCIENZE
Corso di Laurea Magistrale in Fisica del Sistema Terra

Numerical analysis of shedding vortices past a simplified supercell storm

Relatore:
Dr. Carlo Cintolesi

Laureando:
Marcello Grenzi

Correlatore:
Prof. Federico Porcù

Sessione III
Anno accademico 2022/2023

Sommario

Il 5 settembre 2015 un temporale con caratteristiche di supercella ha interessato l'area del Golfo di Napoli, con intensità eccezionale per l'area mediterranea. In occasione di questo evento, si è evidenziata la presenza di una scia di vortici sottovento al temporale, simile ad una von Kármán vortex street (VKVS), tipica dell'interazione di flussi con ostacoli solidi di simmetria cilindrica. Tuttavia, in questo caso alcun ostacolo solido sembra essere presente, suggerendo che il temporale stesso, caratterizzato da violente correnti ascensionali (updraft), abbia agito da ostacolo al vento in troposfera dando origine ai vortici osservati. Questo fenomeno meteorologico, che non trova precedenti nella letteratura scientifica, viene indagato nel presente lavoro tramite Large-Eddy Simulation, un approccio numerico ad alta risoluzione, utilizzando il software open-source OpenFOAM. La simulazione numerica impostata riproduce in modo semplificato la struttura della supercella, affrontando il problema a partire dal classico caso di buoyant jet in crossflow (BJICF). Le condizioni iniziali e la geometria della griglia computazionale sono stimate sulla base del dataset di reanalisi ERA5 e dei dati osservati da radar e da satellite durante l'evento. Il lavoro si sviluppa partendo da una griglia computazionale grezza e procedendo con raffinamenti successivi; vengono poi valutati i contributi della bouyancy, della rotazione e del diametro dell'updraft, tramite simulazioni a 250m di raffinamento. I risultati finali hanno permesso di riprodurre le caratteristiche essenziali del temporale e la presenza dei vortici nella scia dell'updraft, con analogie e differenze rispetto al caso reale: vengono riprodotti vortici con rotazione alternata, dal marcato sviluppo verticale, con una distanza dall'asse centrale di simmetria coerente con le osservazioni, ma un periodo di distacco in disaccordo con il caso reale. Viene anche messa in luce la differenza nel meccanismo di formazione dei vortici simulati rispetto al caso di una VKVS dovuta ad un ostacolo puramente solido: i primi sono riconducibili all'entrainment nell'updraft di aria del crossflow, che genera moti elicoidali verticali simili a quelli prodotti dai counter-rotating vortices nel BJICF; la classica VKVS, invece, trae origine dal boundary layer viscoso intorno all'ostacolo. L'obiettivo del presente lavoro è quello di proporre una metodologia per l'impostazione di una simulazione numerica ad alta risoluzione per lo studio di un fenomeno meteorologico complesso, e fornire una prima, approssimata, rappresentazione della dinamica e dell'origine dei vortici osservati in questo singolare evento atmosferico.

Abstract

On 5^{th} September 2015 a supercell storm occurred in the Gulf of Naples, with exceptional intensity for the Mediterranean area. During this event, the development of shedding vortices was observed past the storm, resembling the von Kármán vortex street (VKVS) typical of flows interacting with solid cylindrical obstacles. However, in this case no solid obstacles are present, suggesting that the storm itself, with its strong vertical updraft, acted as an obstacle to the tropospheric wind, triggering the vortices. This meteorological phenomenon, which has never been reported in literature, is analysed in this work by setting a Large-Eddy Simulation, a high-resolution numerical approach, with the open-source software OpenFOAM. The simulation reproduces a simplified supercell structure, starting from the classical problem of a buoyant jet in crossflow (BJICF). The initial conditions and the computational grid geometry are estimated from ERA5 reanalysis dataset and data from satellite and ground radar collected during the event. Starting from a coarse grid and gradually improving the resolution, the contributions of buoyancy, updraft rotation and variation of updraft diameter are investigated, running the final simulations with 250m resolution. The results reproduce the essential features of the storm and the presence of shedding vortices in the wake, showing differences and similarities with the real case: the simulated vortices have alternate rotation, pronounced vertical development, distance from the central axis coherent with observations, but the shedding period does not match with the real event. Furthermore, the difference is pointed out between the process of formation of the simulated vortices, ascribable to the entrainment of crossflow air into the updraft giving rise to vertical helicoidal motions similar to the counter-rotating vortices in the BJICF, and the one typical of VKVS past a solid body, originating from the viscous boundary layer of the obstacle.

Acknowledgements

The author acknowledges the use of computational resources from the parallel computing cluster of the Open Physics Hub (https://site.unibo.it/openphysicshub/en) at the Physics and Astronomy Department in Bologna.

Contents

Introduction

The interaction between human activities and severe atmospheric events is becoming an increasingly considerable issue nowadays, due to the higher occurrence of these hazardous phenomena together with the rising urban sprawl. From this perspective, the need of preventing risks certainly requires and motivates the scientific purpose of improving both the understanding and the forecasting of potentially dangerous weather events. Despite exceptional advances in Numerical Weather Predictions (NWP) have been achieved since the half of the past century, starting from Charney's pioneering works [1], our skill in resolving a number of severe phenomena still lacks of accuracy and many progresses are necessary for different reasons. First, the typical spatial scales associated with the dynamical evolution of some atmospheric events is very small and difficult to be resolved even by the most accurate present models. Furthermore, surface friction, roughness, heat and moisture transport, etc... all contribute together to make the atmosphere a complex fluid in highly turbulent motion. As formalized by Kolmogorov [2], turbulence is a highly nonlinear phenomenon which is characterized by continuous, chaotic evolution, high Reynolds numbers, mixing effects, dissipative properties and a wide spectrum of scales of motion of the eddies down to millimetric size. Thus, a complete description would need an extremely fine computational mesh, impossible for applications on atmospheric-sized domains. In addition, the microphysical processes such as cloud drops or crystals nucleation, precipitation formation and evaporation further complicate the modeling of the system and require very refined parameterizations. The numerical description of severe thunderstorms resulting from deep convection deals with all of these problems.

In order to partially deal with these issues, a possible method is based on the Large Eddy Simulation (LES) approach, which is the one that will be adopted in this thesis. Developed in the second half of last century from the works of Smagorinsky [3] and Lilly [4],[5], LES apply a spatial filter to the complete Navier–Stokes equations and aim to explicitly resolve motions in the so-called inertial sub-range of the Kolmogorov spectrum, which is usually not attained by atmospheric models, thus giving a much finer description of the system. However, this can be achieved only with a sufficiently dense computational grid (cells width $\leq 250\,\mathrm{m}$ for deep convective systems, according to Lebo and Morrison [6]), implying a relevant computational cost. This has made LES unlikely suitable on large scale domains for a long time, and especially for weather and meteorological studies. Thus it is not surprising that the most widespread LES application to atmospheric physics, starting from the early works of Deardorff [7], mainly concerns the Planetary Boundary Layer (PBL) which is a notably turbulent portion of the troposphere whose motions tend to remain confined in a limited region near the ground. The extension of these studies to deep convective systems (e.g. thunderstorms), whose dynamics occupies the entire troposphere and even slightly more, was prevented up to the new millennium by insufficient computational resources. A few attempts to apply LES techniques to deep

convective systems have been presented in the last 15/20 years, even fewer concerning supercell thunderstorms (Huang et al. [8], Khairoutdinov et al. [9]), and in general LES applications to weather modeling are still scarce but very promising.

This thesis focuses on the analysis of some singular features observed during a supercell event, using a LES approach developed within the open-source Computational Fluid Dynamics (CFD) software OpenFOAM. The phenomenon analyzed in the present study is a heavy supercell hailstorm which grew over the Tyrrhenian Sea and hit the Gulf and the city of Naples, Italy, on September 5^{th}, 2015. This event, whose detailed technical analysis is explained in Marra et al. [10], showed extremely rare intensity for the Mediterranean area, being also one of the most globally relevant storms over more than two years, reaching at certain frequencies the lowest Brightness Temperature (T_B) measured over a 26-month period of NASA Global Precipitation Measurement (GPM) observations. Furthermore, reflectivity data from the operational dual polarization weather radar located in Monte il Monte, Abruzzo, Italy (41.94°N, 14.62°E, 710 m ASL) revealed an unusual shedding of vortices in the wake of the storm towards the coast in the front side of the system, resembling the pattern of a von Kármán vortex street (VKVS). Such behaviour is typical of the flow past solid obstacles and is widely observed in atmosphere in presence of a tracer (e.g. low-level clouds) in the flow around isolated mountains or islands ([11], [12]). However, in the case study examined here no solid obstacles are present, since the storm develops on the sea, suggesting that the storm itself, with its strong upward winds (updraft) driven by deep convection, acts as an obstacle to the mean tropospheric flow. Even though the similarity of storm updrafts and topographic obstacles has been already investigated in a few works (O'Neill et al. [13]), no numerical or physical evidence of VKVS has never been observed yet in the wake of this kind of convective systems until the Naples storm, which makes this event worth analyzing in detail.

The main purpose of this thesis is to set up a numerical simulation of a simplified supercell, in order to investigate and improve the understanding of such unusual shedding vortices, comparing the results with the observations of the real case study of Naples. The work is conducted in different steps:

- analysis of the real Naples supercell storm, in order to estimate the physical and geometrical aspects of the supercell core and its wake. Data available from several instruments are employed in order to compare together different methods, starting from the thesis work of Guidetti [14]. This analysis is included in Chapter 2.
- setup and running of the numerical simulation. We simplify the system in terms of a buoyant jet in cross flow, that simulates the strong updraft struck by the environmental wind. Only the most essential and relevant aspects of the system are included, using the initial and boundary conditions in agreement with the quantities estimated at the previous step. This is the matter of Chapter 3.
- A working methodology is presented, starting from the numerical mesh assessment in order to find an optimal grid to run the final simulation. Furthermore, increasing levels of complexity are added gradually, in order to understand their individual effect on the system, starting from a purely dynamical system and adding the thermal contribution later. These are the topics of Chapter 4.
- analysis of the results of the final numerical simulations and comparison with the real case study, topic of Chapter 5.

Chapter 1

Theoretical background and literature review

This Chapter illustrates the theoretical features of supercell storms and their mechanism of formation, giving also a brief review of the numerical approaches to the study of such meteorological events. Coherently with the main topic of this thesis, an overview of the theory of classical von Kármán vortex streets is then presented, as typical features of the flow past solid obstacles. Finally, we describe the state-of-the-art knowledge of wake vortices in presence of fluid obstacles.

1.1 The supercell thunderstorm

Supercells are probably the least common storm type worldwide, but they nonetheless are responsible for a large fraction of severe weather reports. Almost all reports of hail having a diameter of 5 cm or larger are associated with supercell storms, as are virtually all strong and violent tornadoes. Supercells can also produce extremely high lightning flash rates, with rates exceeding 200 flashes per minute possible. Supercells are frequently long-lived (1–4 h lifetimes are common, and some have been observed to persist as long as 8 h); in fact, this is one reason why they were originally called supercells. The analysis of the formation of this kind of storm is the topic of the following two Sections.

1.1.1 General structure of convective thunderstorms

The mechanism at the basis of the generation of thunderstorms is deep moist convection (DMC), which arises when air is lifted to saturation and subsequently achieves positive buoyancy, such that it may rise to great heights. The initiation of DMC, which we shall simply refer to as convection initiation, requires that air parcels reach their Level of Free Convection (LFC), that is the first height at which the saturated air particle has a higher temperature than its surroundings, and subsequently remain positively buoyant over a significant upward vertical excursion.

This requires as necessary, albeit insufficient, condition the presence of a Convective Available Potential Energy (CAPE), which is the maximum amount of potential energy that a lifted air parcel starting from the ground has available for convection. A high value of CAPE is an indication of strong atmospheric instability that favors, but not ensures, the initiation of convective motions that determine the formation of storm clouds. In fact, the CAPE itself does not guarantee the beginning of convection, since the ground-based

parcel has to overcome a certain amount of energy per unit mass, called Convective Inhibition (CIN), before becoming buoyant compared to the surrounding environment. If this happens, thanks to various possible causes (e.g. forced lifting due to a cold front, a mountain, low-levels wind convergence, etc.), the parcel reaches the Level of Free Convection (LFC), which is the first height at which the saturated air particle has a higher temperature than its surroundings. Once this level is reached, the buoyancy force becomes positive making the particle free to continue its upward motion along a moist adiabatic transformation, without opposing restorative forces tending to bring it back to a previous equilibrium position. Therefore, the particle continues to rise converting the available potential energy into kinetic energy up to the Equilibrium Level (EL), where it returns to have the same temperature as the surrounding environment, being again in a stable equilibrium condition.

Given these necessary definitions, formally the CAPE is expressed, in z or log-p coordinates, as:

$$CAPE = g \int_{LFC}^{EL} \frac{T_p^v - T_e^v}{T_e^v}\, dz = -R \int_{p(LFC)}^{p(EL)} (T_p^v - T_e^v)\, d(ln\, p) \tag{1.1}$$

$$\text{where} \quad T_{p,e}^v = T_{p,e} \frac{w_{p,e} + \epsilon}{\epsilon(1 + w_{p,e})} \sim T_{p,e}(1 + 0.608 w_{p,e})$$

where T_p^v and T_e^v are the virtual temperatures of the lifted parcel and of the environment, respectively, g is gravity, R the gas constant, ϵ the mole fraction of water vapor in dry air and w the water vapor mixing ratio.

In light of these basic arguments, the process of formation of thunderstorms is extremely complex, leading to a wide spectrum of possible evolution scenarios. However, some typical elements can be pointed out in the development of the storm cloud, the cumulonimbus. The fundamental structure of the storm is always the so-called convective cell, which undergoes a typical life cycle divided into three main stages (Fig.1.1), as discussed by Byers and Braham [15].

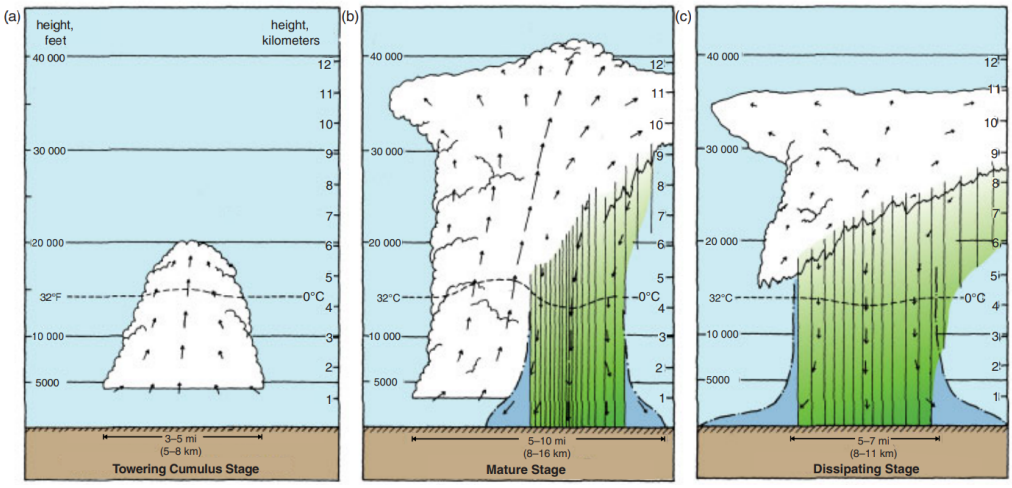

Figure 1.1: The three stages of cumulonimbus life, as in Byers and Braham model [15].

From Fig.1.1 it is possible to distinguish between:

- **Cumulus stage:** formation of the convective cell. Air that is warmer than the environment starts to rise driven by convection. When this warm, moist air rises, it also cools and condenses, forming a cumulus cloud. Due to its instability, this air

experiences an increasing acceleration with height, forming the ascendant current named *updraft*. The updraft is able to suspend and push up the small raindrops even further in the cloud, which begin to grow into larger raindrops that are big enough to collide and merge with one another. The clouds can grow even above the freezing level, where supercooled water molecules exist, crucial for the formation of hail and ice particles. In this stage, no rain has reached the ground yet.

- **Mature stage:** formation of cumulonimbus with occurrence of rain. The rising air reaches the tropopause where spreads out and the typical *anvil* shape cloud becomes visible (see Fig.1.2). If the updraft is strong enough, an *overshooting top* forms above the tropopause. When finally the updraft becomes colder than the surrounding air, the downdraft takes form, that is a fast descending current where also evaporative cooling takes place, due to the relative dry air below the cloud. The evaporative cooling acts to further strenghten the downdraft, that hits the ground and spreads out in all directions forming an outflow and the subsequent gust front. In this stage, showers, hail and lightning activity can be observed and as long as the updraft is sustained.

- **Dissipating stage:** during this stage, the rain-cooled air spreads far from the updraft; the updraft is then cut off from the buoyant inflow and cannot be maintained anymore. New cells may or may not be initiated by the gust front, depending on the environmental CIN. Eventually the old convective cloud is reduced to an orphan anvil composed entirely of ice crystals. The anvil slowly sublimates into oblivion (this can take many hours).

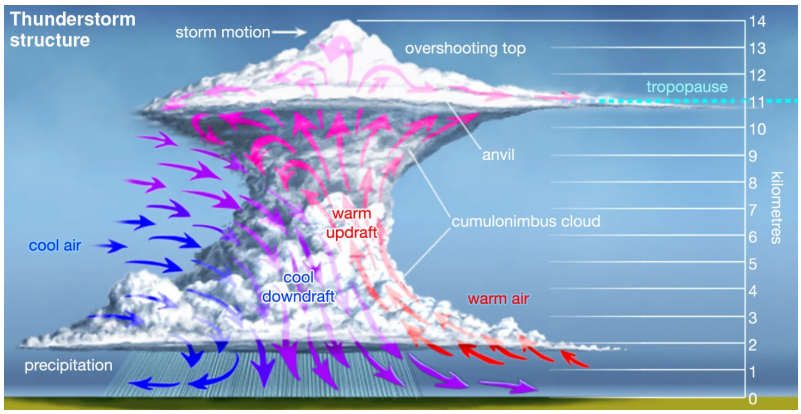

Figure 1.2: Diagram of the typical structure of a cumulonimbus.

Depending on the environmental conditions, the DMC can lead to the formation of three general kinds of deep convective systems, different for structure, lifetime and intensity: single-cell storms, multicell storms and supercell storms. The last type is the one that is now analysed in detail.

1.1.2 General structure of supercell storms

A supercell thunderstorm is a large, quasi-steady, unicellular storm that propagates with extreme intensity and causes hazardous events like hailstorm or tornadoes. Vertical velocities can exceed 50 m/s within the most intense supercell updrafts. The widely accepted dynamical criterion is the presence of a persistent, deep *mesocyclone* within the updraft. A mesocyclone is a region of vertical vorticity of magnitude of $O(10^{-2})\text{s}^{-1}$, characterised

by rotation. The mesocyclone should persist long enough for an air parcel to pass through the entire updraft (∼20 min), and it should extend over at least half the depth of the updraft. Supercells can also be distinguished dynamically from nonsupercells by way of their propagation, which, in contrast to nonsupercells, is not dominated by the triggering of new cells by the gust front. A crucial ingredient for the formation of supercells is the presence of a large vertical wind shear in the environment, that is the variation of the wind vector with height. In other words, typical long *hodographs* characterise supercell environments (Fig.1.3a).

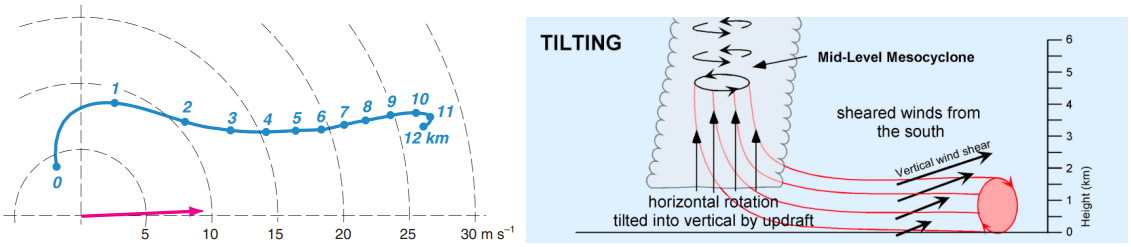

(a) (b)

Figure 1.3: Fig.1.3a: typical supercell hodograph, showing the variation of the wind vector with height (blue numbers along the curve). The distance from the center indicates the module, while the angle from the positive horizontal axis indicates the direction (from [16]). Fig.1.3b: process of tilting of horizontal vorticity in the generation of rotation in the mid-level mesocyclone.

The horizontal vorticity associated with the large vertical wind shear in supercell environments is the source of vertical vorticity for the midlevel mesocyclone by way of the tilting term in the vorticity equation. The equation for vertical vorticity ζ can be written as:

$$\frac{\partial \zeta}{\partial t} = -\boldsymbol{U} \cdot \boldsymbol{\nabla}\zeta + \boldsymbol{\omega} \cdot \boldsymbol{\nabla} w \tag{1.2}$$

where $\boldsymbol{U} = (u, v, w)$ is the velocity vector, $\omega = (\xi, \eta, \zeta)$ is the vorticity vector. We have neglected the Coriolis force which does not contribute to $\partial\zeta/\partial t$ in a major way. If we perform a linearisation $u = \overline{u}(z) + u'$, $v = \overline{v}(z) + v'$, $w = w'$ and $\zeta = \zeta'$, and we rewrite the equation in the moving reference frame of the updraft that is supposed to move at constant velocity $\boldsymbol{c}$, then:

$$\left(\frac{\partial \zeta'}{\partial t}\right)_{sr} = \underbrace{-(\overline{\boldsymbol{U}} - \boldsymbol{c}) \cdot \boldsymbol{\nabla}_h \zeta'}_{\text{advection}} + \underbrace{\frac{\partial \overline{\boldsymbol{U}}}{\partial z} \times \boldsymbol{\nabla}_h w' \cdot \boldsymbol{k}}_{\text{tilting}} \tag{1.3}$$

where $\overline{\boldsymbol{U}} - \boldsymbol{c}$ is the storm-relative wind, $\partial\overline{\boldsymbol{U}}/\partial z$ is the vertical wind shear and $(\partial\zeta'/\partial t)_{sr}$ the vertical vorticity tendency in the storm-relative reference frame. Therefore, the generation of vertical vorticity, which is the basis of updraft rotation, is partially due to the advection of ζ' by the (horizontal) storm-relative wind; partially by the vertical tilting, caused by the rising air of the updraft w' forced by convection, of the horizontal vorticity generated by the mean vertical wind shear of the environment $\partial\overline{\boldsymbol{U}}/\partial z$. See Fig.1.3b.

The vertical wind shear present in supercell environments tends to extend over a significant depth of the troposphere (Fig.1.3a), rather than being confined to the atmospheric planetary boundary layer (PBL, i.e. the lowest part of the atmosphere whose behaviour is directly influenced by the interaction with the Earth surface), which is the case in some multicell storm environments. The fact that the vertical shear in supercell environments

tends to span a significant depth of the troposphere results in significant storm-relative winds throughout most of the troposphere. Vertical pressure gradients arising from the interaction of an updraft with vertical wind shear, as well as dynamical effects associated with the mesocyclone, can also enhance the updraft. It is in this way that supercells differ from ordinary cells, which are driven almost solely by buoyancy. Although CAPE tends to be significant ($> 1000\,\mathrm{J/kg^{-1}}$) in supercell environments, extreme values of CAPE are not necessary for supercells. Furthermore, the motion of supercells generally tends to deviate significantly from the mean wind, with cyclonically (anticyclonically) rotating supercells having a propagation component to the right (left) of the mean wind: these supercells are defined, respectively, right-movers or left-movers. Therefore, the supercell updraft can rotate clockwise or counterclockwise in both hemispheres (Coriolis is a higher order effect in their dynamics), although the former (right-movers) are more frequent in the Northern Hemisphere. In summary, conditions likely to develop a supercell are the following:

- strong thermal and hygrometric (humidity) contrast along the vertical direction between wet warm rising air and dry cold air embedded in the same region
- significant heating from the ground, which enhances the process of convection
- the presence of vertical wind shear in the lower levels which enhances the rotation in the cumulonimbus

Now it is important to describe the visual structure that distinguishes the supercell storms from the single- and multi-cell storms. Many of these features are observed also in the Naples supercell, as described in Marra et al. [10]. A locally lowered cloud base called a *wall cloud* is often present at the base of the updraft, where humid, rain-cooled air originating from the precipitation regions is drawn into the updraft, reaching saturation at a lower altitude than the height at which ambient environmental air becomes saturated via lifting. An attendant flanking line of updrafts also can occasionally be seen, typically located on the right-rear flank (with respect to storm motion) and shallower than the dominant updraft. In Fig.1.4 some schemes generalizing the main features of the supercell.

The updraft of a supercell is typically associated with a reflectivity minimum in radar data, called the *bounded weak-echo region* or BWER (Fig.1.4b). The BWER is assumed to signify a region of updraft too strong to allow the descent of hydrometeors. At low levels, the BWER may not be 'bounded', in which case a *weak-echo region* (WER) exists. The downward extension of the rear side of the echo overhang that caps the BWER forms a pendant-shaped *hook echo* in radar imagery at low elevations (Fig.1.4c). The hook echo is the best-recognized reflectivity feature associated with a supercell storm.

Supercells contain two main downdraft regions. The first is associated with the hook echo region to the rear of the storm. This downdraft is referred to as the *rear-flank downdraft* or RFD (Fig.1.4c). RFD is a complex thermodynamically and dynamically region of subsiding air: its formation can occur due to the vertical pressure gradient forces. The rotating updraft acts as an obstruction to the mid-upper level flow. As soon as the air builds up in the upper level due to the updraft, it begins to sink forming an RFD on the back side of the supercell. As a result of the deep-layer wind shear and upperlevel storm-relative winds, the majority of the hydrometeors are deposited on the forward flank of the updraft. Evaporation of rain and the melting and sublimation of ice lead to the development of negative buoyancy and a *forward-flank downdraft* (FFD) is created, with heavy rain. When hit the ground, the FFD and RFD collectively produce a surface gust front structure that can cause significant straight-line wind damage.

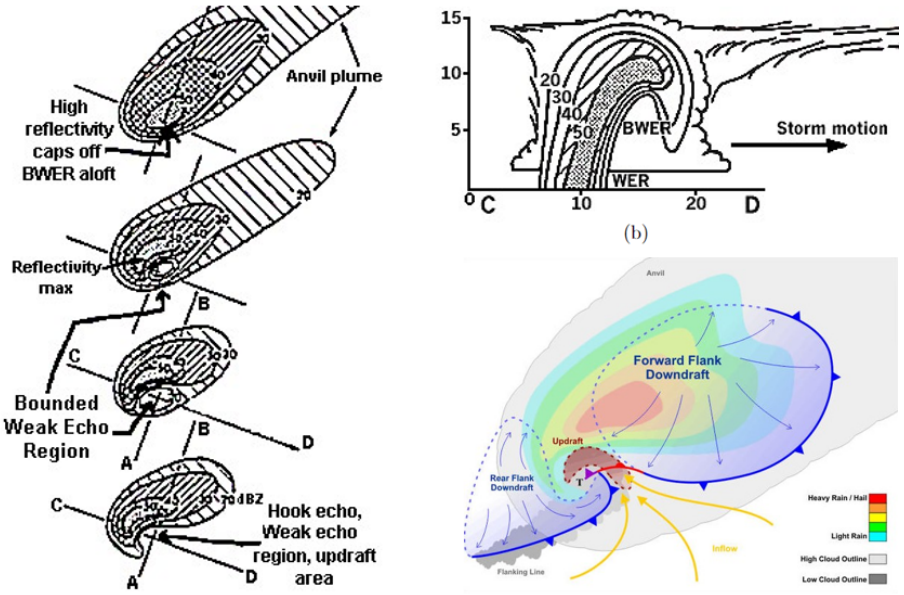

(a) (b) (c)

Figure 1.4: Fig.1.4a: adapted from [17], schematic representation of echo regions of a typical supercell (contours are reflectivity in dBZ), at different heights. Fig.1.4b: vertical section along CD direction in Fig.1.4a (contours are reflectivity in dBZ). Fig.1.4c: Schematic representation of the supercell structure showing the FFD and RFD.

Finally, another significant feature typical of mid-latitudes supercell storms is the so called above-anvil cirrus plume (AACP). An AACP consists of a thin cirrus plume, located downstream the overshooting top and often visible by satellite, which shoots several kilometers above the much larger anvil cloud directly into the lower stratosphere where it spreads downwind. AACPs exhibit a high correspondence with the most severe conditions on the ground, including major tornado and hail events. Therefore, AACPs can aid in the predictability of severe hail and tornadoes, as AACPs are visible above the cloud tops an average of 31 min before severe conditions are reported.

1.1.3 Review of numerical approaches for supercells description

The risk associated to supercell storms, together with the exceptionality of these events, has pushed meteorologists to investigate their nature not only with experimental campaigns (e.g. Marwitz [18], Browning and Donaldson [19]) but also with numerical models of increasing level of complexity. From the beginning of these studies, the main approach to this problem has been based on the use of Cloud Resolving Models (CRMs). A CRM allows performing numerical simulations of convective clouds, such as shallow cumulus, stratocumulus or cumulonimbus, with a resolution on the order of a few tens of metres to a few kilometres over a limited-area 4D (time and space) domain. CRMs are used in a variety of ways, from the exploration of cloud phenomenology and process-understanding studies to the development of algorithms for satellite products, as well as to address climate issues and to develop convective and cloud parametrizations for large-scale weather and climate models. Generally speaking, CRMs need:

- equation of state
- prognostic equations for the three components of velocity u, v, w

- prognostic equations for a temperature variable
- prognostic equations for water variables
- continuity equation (conservation of mass)
- non-hydrostatic dynamics

Together with CRMs, a similar but more refined approach applied to cloud physics has been Large-Eddy Simulation (LES), inherited from Computational Fluid Dynamics. An exhaustive description of LES approach, that will be the one used in this thesis work, is given in Chapter 3. LES were first used for atmospheric turbulence in the 60s (Smagorinsky [3]; Lilly [5]; Deardorff [7]). A LES is a self-consistent technique, which applies a high-pass filter to the Navier–Stokes equations in order to avoid the computational cost of resolving all the scales of motion and makes use of models (or parametrizations) to represent sub-grid scale motions. This task, anyway, still requires a very remarkable computational cost, that for a long time has made LES very well suited for the simulation of turbulent motions only in atmospheric boundary layer (that is, on a limited portion of the atmosphere). By contrast, the motivation underlying the development of CRM was, from the start, to better understand deep convective cloud motions, such as supercell storms, involving water phase changes in the atmosphere. However, beyond differences in their formulation of sub-grid processes (see Chapter 3), the underlying equations of CRMs and LES are similar, and the distinction between the two now often refers to the use of finer (LES) vs. coarser (CRM) grids in numerical simulations.

The first attempts to the numerical simulation of supercell storms through CRMs go back to 1960s. Fujita and Grandoso [20] developed a simple model to investigate the behaviour of a supercell after the storm splitting, that is the division of the updraft in two parts, with one side propagating to the left (left mover) and the other to the right (right mover). They actually didn't reproduce the process of splitting, but initialised the simulation with an already splitted storm. In this paper, the author suggested that the presence of two vortices (cyclonic and anticyclonic) in the wake of the updraft could form new clouds when the gust front produced by the downdraft interacts with them, by forcing warm air to rise into them. In this sense the updraft should act as a solid-like cylindrical obstacle, forming the two counter rotating vortices. However, in the following years this interpretation of the splitting process was completely abandoned, after the numerical simulations performed by Schlesinger (1975 [21], 1978 [22], 1980 [23]). Anyway, the cylindrical-like behaviour of cumulus clouds is actually observed in different works: in agreement with the conceptual model of Newton and Newton [24] and the observations reported by Fankhauser [25], Wilhelmson ([26], 1974) found that the predicted three-dimensional wind field around a supercell exhibited features reminiscent of flow about a cylinder (deflection of the flow around the obstacle). However, *no evidence* of the formation of shedding vortices (typical of solid cylinders) behind supercell storms has ever been reported in literature.

The pioneering works of Schlesinger and Wilhelmson can be considered one of the first attempts to reproduce severe storms in three dimensional models. Both their models are composed of seven equations for the same dynamical and thermodinamical variables, but differ for the spatial resolution (1.8 km for Schlesinger [22], 600 m for Wilhelmson [26]). In both models, Coriolis force is neglected, the incompressible fluid (anelastic) approximation is applied and the ice phase of water is neglected. Their work revealed many aspects on the formation of supercell storms, confirming the crucial importance of the tilting of horizontal vorticity due to vertical wind shear for the generation of updraft rotation and its impact

on the storm life time. These models are the basis for the development of more complex and accurate models in the following years. Klemp and Wilhelmson - 1978 ([27], [28]) confirmed the results of Schlesinger by relaxing the anelastic approximation (compressible flow), using also more accurate parameterisations of microphysics and turbulence, with horizontal resolution 1 km. They also introduced Coriolis force, confirming that it is only responsible of small asymmetries between right- and left-movers supercells. The approach of Klemp and Wilhelmson is recalled by many following authors. Within this framework, Tripoli and Cotton ([29], 1981; [30], 1982) introduced ice phase in the equations; Wang and Straka ([31], 1992) developed the Wisconsin Dynamical-Microphysical Model (WISC-DYMM) to study the effect of ice phase parameterisations on the lifetime, propagation and intensity of supercells, with remarkable results.

In the last 20 years, the main focus has been posed on the refinement of microphysics and atmospheric boundary layer parameterisations in the models and the increase in spatial resolution permitted by the growing computational resources. Many works are now based on one of the best state-of-the-art CRMs, the Bryan Cloud Model [32], which is run now at resolutions typical of many LES approaches (100/200 m). This allows to perform very accurate numerical studies of small-scale turbulent processes involving the interaction between supercell storms and the convective atmospheric boundary layer (Nowotarski et al. [33], [34]) or the generation of the typical supercell AACP (O'Neill et al. [13]).

Also LES have started to be applied to deep convective systems with very promising results, focusing on the interaction between supercell storms and the underlying boundary layer and on sensitivity analyses to the spatial resolution of the simulation. Bryan et al. [35] showed that grid spacings of 250 m or less are required for Large-Eddy Simulations to perform according to their design. Huang et al. [8] showed using LES that the initiation of deep convection was favoured with certain regular organization of boundary-layer convective motions of warm moist air (thermals). This complements the results of Khairoutdinov and Randall [36], who found with another LES that the rapid growth of deep convection can be related to boundary-layer heterogeneities created by the evaporation of rainfall.

The gap between LES and CRMs is steadily closing, primarily because of rapid advances in massively parallel supercomputing. Nevertheless, so far, there have been only very few LES studies of deep convection with a horizontal grid spacing of $O(100/200\,\mathrm{m})$.

1.2 Shedding vortices past obstacles

The main topic of this thesis requires a brief description of the theory of shedding vortices in the wake of obstacles with cylindrical shape. A necessary distinction is made between the classical case of a solid body and the less common situation of a fluid obstacle, which is however the one that is observed in the Naples event.

1.2.1 Flow past solid obstacles: von Kármán vortex streets

In fluid dynamics a von Kármán vortex street (VKVS) is a well known pattern of vortexes shed with a certain frequency and observable when a fluid circulates around a blunt solid body. In particular, the flow past a circular cylinder is a classic problem in fluid dynamics. At first, we have to explain the Reynolds Number and the very important concept of the viscous Boundary Layer. The Reynolds number (R_e) is the ratio of inertial forces to viscous forces in a fluid. It is a dimensionless number used to determine whether a fluid is in a laminar (small R_e) or turbulent motion (large R_e):

$$R_e = \frac{UD}{\nu} \tag{1.4}$$

where U is the fluid velocity, D is the characteristic length (or scale length) of the system, ν is the kinematic viscosity.

The concept of the boundary layer is considered one of the cornerstones in the history of fluid dynamics. In 1905 Ludwig Prandtl hypothesized that, for small viscosity, the viscous forces are negligible everywhere except close to the solid boundaries where the *no-slip* condition has to be satisfied (velocity field vanishes at the solid boundaries). The thickness of these boundary layers approaches zero as the viscosity goes to zero. The higher the Reynolds Number, the thinner the boundary layer, hence the equation of motion is simplified, with the velocity varying rapidly enough for the viscous force to be important. Viscous boundary layers exist not only next to solid walls, but also in the form of wakes and shear layers if the Reynolds number is sufficiently high. The continuity and Navier–Stokes equations for a two-dimensional steady incompressible flow in Cartesian coordinates (x tangential to the wall, y orthogonal to it) are given by:

$$\begin{cases} \dfrac{\partial u}{\partial x} + \dfrac{\partial v}{\partial y} = 0 \\ u\dfrac{\partial u}{\partial x} + v\dfrac{\partial u}{\partial y} = -\dfrac{1}{\rho}\dfrac{\partial p}{\partial x} + \nu\left(\dfrac{\partial^2 u}{\partial x^2} + \dfrac{\partial^2 u}{\partial y^2}\right) \xrightarrow{\text{BLA}} u\dfrac{\partial u}{\partial x} + v\dfrac{\partial u}{\partial y} = -\dfrac{1}{\rho}\dfrac{\partial p}{\partial x} + \nu\dfrac{\partial^2 u}{\partial y^2} \\ u\dfrac{\partial v}{\partial x} + v\dfrac{\partial v}{\partial y} = -\dfrac{1}{\rho}\dfrac{\partial p}{\partial y} + \nu\left(\dfrac{\partial^2 v}{\partial x^2} + \dfrac{\partial^2 v}{\partial y^2}\right) \xrightarrow{\text{BLA}} \dfrac{\partial p}{\partial y} = 0 \end{cases} \tag{1.5}$$

where u and v are the velocity components, ρ is the density, p is the pressure, and ν is the kinematic viscosity of the fluid. In Eq.1.5 we applied the so-called Boundary Layer Approximation (BLA), obtained through a scale analysis: we assume the streamwise characteristic length is significantly larger than the transverse one, inside the boundary layer. It follows that *variations* (i.e. derivatives) of properties in the streamwise direction are generally much lower than those in the wall normal direction: $\partial/\partial x << \partial/\partial y$ and $\partial^2/\partial^2 x << \partial^2/\partial^2 y$. Apply this to the continuity equation shows also that v, the wall normal velocity, is small compared with u, the streamwise velocity: $v << u$.

If we apply the no-slip condition $u(x,0) = 0$, $v(x,0) = 0$ and we impose that the streamwise velocity inside the boundary layer approaches smoothly the unperturbed background velocity $U(x)$ outside the boundary layer ($u(0,\infty) = U(x)$), Eq.1.5 computed at the solid wall ($y = 0$) simplify to:

$$\begin{cases} v(y) = -\displaystyle\int_0^y \frac{\partial u}{\partial x}\, dy' \\ \nu\dfrac{\partial^2 u}{\partial y^2} = \dfrac{1}{\rho}\dfrac{\partial p}{\partial x} \\ \dfrac{\partial p}{\partial y} = 0 \end{cases} \tag{1.6}$$

When the obstacle is a curved object (see Fig.1.5), upstream of the highest point the streamlines of the background flow converge, with a subsequent increase of $U(x)$ and a fall of pressure. Conversely, downstream of the highest point the streamlines diverge, $U(x)$ decreases with x, while pressure increases with x. So, in the upstream stretch $\partial p/\partial x < 0$ and in the downstream stretch $\partial p/\partial x < 0$. From second equation in Eq.1.6, this means that in the upstream stretch u has a negative concavity and boundary layer becomes thinner. In the downstream stretch, there is the opposite situation and the boundary layer leads to increase its thickness. From first equation in Eq.1.6 in the downstream part, the normal component of the velocity increases. The increase of the thickness and

of the v-component causes the *separation* phenomenon: the flow next to the wall reverses its direction at some point S and separates from the wall boundary layer. S is called the *separation point*, and approximately determines the beginning of the wake region. Downstream of the separation point, the pressure remains fairly uniform, but *lower* than pressure on the upstream side, resulting in a net pressure difference between the upstream and downstream sides of the obstacle. In the downstream, the BLA is valid only till the point of separation, since the layer is still thin enough. The position of the separation point depends on the value of the R_e: when $R_e < 3 \cdot 10^5$ the boundary layer remains laminar and separates at $\sim 82°$ from the forward stagnation point; above this value the boundary layer becomes turbulent and the separation point is moved further from the stagnation point, at about 125°.

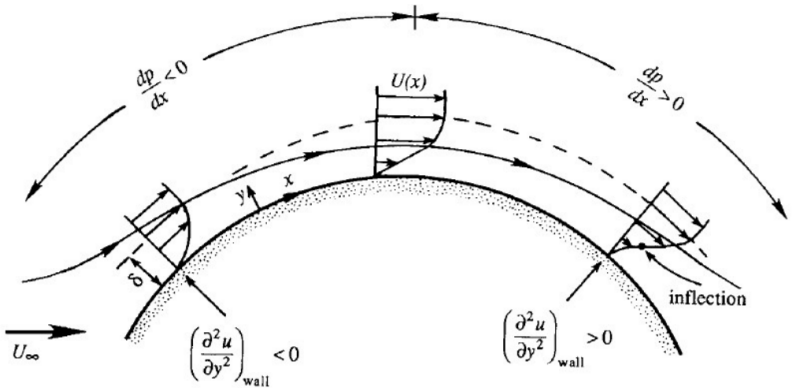

Figure 1.5: Velocity profiles across boundary layer with favorable and adverse pressure gradients (taken from [37]).

For the case in consideration of the flow past a circular cylinder, analytical solutions exist only if $R_e << 1$ (the inertia forces are negligible across most of the flow field) or if $Re >> 1$ (the viscous forces are negligible everywhere except close to the surface). For intermediate values of Re, an analytical solution does not exist. Possible solutions exist only through experiments or numerical methods:

- At low Reynolds Numbers, if $Re < 1$, the vorticity is confined close to the surface due to the no-slip boundary condition. If $R_e > 1$ it is confined behind the cylinder due to the advection that becomes more important (Fig.1.6a). If $R_e > 4$, two small attached or "standing" eddies appear behind the cylinder (Fig.1.6b). The wake is completely laminar.

- When $R_e > 40$, the von Kármán vortex street forms behind the cylinder, the wake becomes unstable and develops a slow oscillation in which the velocity is periodic in time, with the amplitude of the oscillation increasing downstream. The oscillating wake rolls up into two staggered rows of vortices with opposite sense of rotation. When $R_e > 80$, the vortex street forms closer to the cylinder, and the attached eddies begin to oscillate (Fig.1.6c). The frequency of vortex shedding is expressed as a nondimensional parameter known as the Strouhal number, defined as:

$$S_t = \frac{f\, d}{U_\infty} \tag{1.7}$$

  where f is the frequency of shedding, d is the cylinder diameter and U_∞ is the crossflow velocity. S_t remains close to 0.21 for a large range of R_e.

- For $R_e > 200$, the vortex street becomes unstable and the flow within the vortexes themselves becomes turbulent; S_t is always close to 0.21. An upper value of R_e for the formation of VKVS has never been established definitely, quasi-periodic coherent vortex shedding is observed even in highly turbulent laboratory flows with R_e of the order of 10^6 (Williamson, [38]).

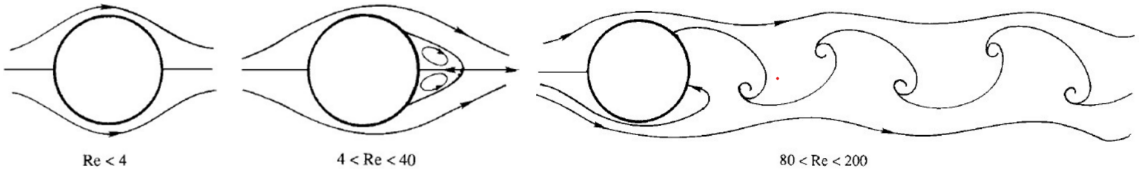

(a) (b) (c)

Figure 1.6: Flow around circular cylinder and VKVS at different values of R_e.

In the atmosphere, VKVS are regularly observed in low marine stratocumulus downstream mountain islands (Fig.1.7), trapped in the first 1/2 kilometers of atmosphere in presence of a stable vertical temperature profile. In these cases, the $R_e \sim 10^8/10^{10}$ is extremely higher than in common circular cylinder experiments. An oscillating wake with a quasi-regular vortex shedding period of 2–4 hr is reproduced by numerical simulations [12]. The periodicity of numerically modelled atmospheric vortex streets was investigated by Nunalee and Basu [39]. Varying the diameter and height of an idealized axisymmetric bell-shaped island, they found the shedding period generally increasing with crosswind island diameter. The Strouhal number fluctuated within the broad range of 0.15–0.22; however, S_t did not exhibit any obvious dependence on R_e, unlike for circular cylinders.

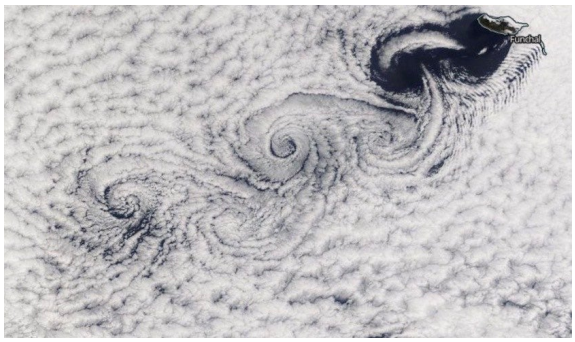

Figure 1.7: A Von Karman vortex street downwind the Canary Islands, Feb. 27, 2015.

1.2.2 Vertical jet in cross-flow: theory and review

The existence of wake vortices in presence of a fluid obstacle is a much less common case study, which is found almost only in laboratory experiments of fluid mechanics, engineering or numerical analyses in computational fluid dynamics. A fluid obstacle can have many possible origins, but generally can be addressed as a region of fluid with different velocity direction and/or density that interacts with a background flow. The typical example that can be found in literature is the case of a transversal *jet in cross flow* (JICF), that is a jet of fluid that exits a nozzle, to interact with the surrounding fluid. If the jet density doesn't differ from the background flow, it is generally addressed as a *momentum jet*; on the other hand, the more general case where the jet has also a different temperature/salinity is described as a (negatively or positively) *bouyant plume* or BJICF. The literature studies on JICF are abundant, but the vast majority focus of the jet description instead of the

wake region. For the purposes of this thesis, it is important however to give a brief overview on the main overall features of JICF.

The general case of the buoyant plume shows that the dynamics is characterised by at least three phases:

- momentum phase, the plume is mainly driven by the initial momentum;
- buoyancy phase, the buoyancy force strongly pushes the plume upward/downward;
- entrainment phase, the cross-flow deviates the plume in horizontal direction.

If the jet has no buoyancy, simply the buoyancy phase is not present. Such phases can occur simultaneously in a same spatial region. For example, if the buoyant force is weak with respect to the initial momentum, the second and first phases partially overlap; hence a pure buoyancy driven phase does not exist even if the plume undergoes to the effects of buoyancy force. Fischer et al. [40] derived two parameters that estimate the height at which the momentum and the buoyancy force strongly exercise their influence on the plume. The vertical length scale for the influence of initial momentum z_M and the one for the influence of buoyancy z_B are:

$$z_M = \sqrt{\frac{\pi}{4}}\frac{u_j}{u_{cf}}D \qquad z_B = \frac{B_j}{u_{cf}^3} \tag{1.8}$$

where u_j is the initial plume vertical velocity, u_{cf} is the crossflow velocity, D is the nozzle diameter (the jet exit), B_j is the initial buoyancy flux of the plume. The entrainment region starts for $z > z_B$ or, in absence of buoyancy, for $z > z_M$. Jet trajectories in the $x-z$ plane, generally computed for the far-field where the main structures are fully formed (that is, approximately in the entrainment region), are usually parameterised as:

$$\frac{z}{\kappa D} = \alpha\left(\frac{x}{\kappa D}\right)^{\gamma} \qquad \text{with } \kappa = \frac{u_j}{u_{cf}} \tag{1.9}$$

where α and γ are constants deduced from empirical or scaling arguments. Apart from more sophisticated forms, the typical profile for the buoyant plume is $\gamma = 2/3$ and for the momentum jet is $\gamma = 1/2$ (Cintolesi et al. [41]), although in this latter case there is not a clear consensus (see Mahesh [42]).

The instantaneous behavior of a jet/plume is unsteady and violent. As the jet fluid approaches the exit, it experiences an adverse pressure gradient on the upward side of the nozzle, owing to the high-pressure region created above the jet exit by the crossflow (as it was for the case of the solid cylinder). This causes the jet profile to be skewed toward the downstream side. In general, both small-scale turbulence and large-scale coherent features are observed. Several coherent vortex systems have been identified, summarised in Fig.1.8a:

- **Counter-rotating vortex pair (CVP):** CVP has long been considered a signature feature of jets in crossflow and persists far downstream. The CVP is a steady feature of the jet which is observed also in the time-averaged field. Early experiments showed how, far downstream, the original jet seemed to disappear while a pair of vortices dominated the flow field. CVP formation is delayed as the jet velocity ratio increases. Different mechanisms leading to the CVP have been suggested, and almost all locate the origin of the CVP formation in the near field ([41]). The mechanism of formation will be investigated later in this work, together with the results of the numerical simulations.

- **Shear-layer vortices:** jet shear-layer vortices are typically observed on the upward side of the jet, where the jet strongly deflects under the action of the crossflow. They assume the shape of annular rings which encompass the top part of the jet, are highly unsteady, and are not observed in the time-averaged solution.
- **Horseshoe vortex:** horseshoe vortices form upstream of the jet's leading edge and persist downstream. These vortices form because the crossflow boundary layer encounters the adverse pressure gradient upstream of the jet (as in the solid cylinder case), separates, and forms the horseshoe vortex that move around the jet. The horseshoe vortex can be observed also in the time-averaged field.
- **Wake vortices:** wake vortices are the upright vortices observed downstream of the jet, extending from the bottom wall to the leeward side of the jet. These vortices are unsteady and disappear in the time averaged field. When visualized in planes parallel to the wall, the vortices resemble the vortex street observed behind solid cylinders. However, as noted by Fric and Roshko (1994) with a momentum jet, the wake of a transverse jet is *noticeably different* from that of a circular cylinder at the same Reynolds number (Fig.1.8b). By introducing smoke in the bottom boundary layer, and from spectral measurements, they suggested that the wake vortices originate from separation events in the bottom boundary layer downstream of the jet, and not from the jet itself. This finding, that the wake vorticity comes from the crossflow boundary layer, is obtained for a momentum jet, that is when the jet and crossflow have the same density. Even though wake vortices are observed also in case of buoyant plumes ([41]), no relevant literature is found on the mechanism of formation of wake vortices in this case. Laboratory experiment by Kelso et al. [43] verified these observations, and pointed out also that the wake vortices do not strictly alternate in sign but occasionally can occur in pairs of vortices with the same rotation. The results of Fric and Roshko [44] are confirmed also by more recent LES numerical experiments [45].

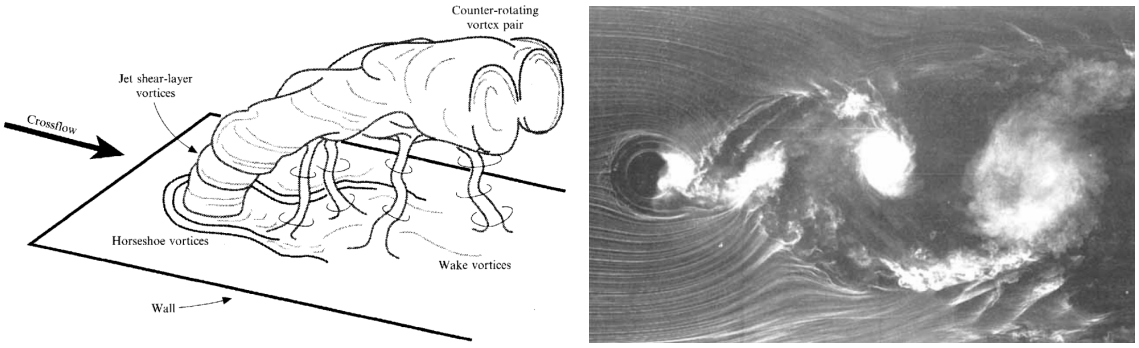

(a) (b)

Figure 1.8: Fig.1.8a: summary of the vortex systems in JICF (adapted from [44]). Fig.1.8b: wake vortices similar to VKVS observed by Roshko in laboratory experiment.

Even if these studies of JICF/BJICF revealed the presence of organised wake vortices (despite different for their origin respect to the classical VKVS from solid cylinders), no evidence of shedding vortices from fluid obstacles has ever been pointed out in meteorology, even more so in rare systems like supercell storms. This makes the Naples supercell a particularly interesting case study.

Chapter 2

The Naples supercell storm

The Naples hailstorm of 5 September 2015 originated in the early morning from a southward plunge of the jet stream that carved into Western Europe, sending an upper disturbance into the Italian peninsula. That instability, associated with high Sea Surface Temperature (SST) and low-level wind convergence, stirred up an impressive severe thunderstorm with intense lightning activity and strong winds. The storm, that is a typical example of a cyclonic, right-mover supercell, was exceptionally violent, dropping 10/12 cm diameter hailstones along its path over the sea and over land. The exceptionality of this storm is confirmed by the brightness temperature measured by the NASA Global Precipitation Measurement satellite at 18.7 GHz, which ranks as the lowest one the over a 26-month period of global observation. It is also worth noting that operational and research Numerical Weather Prediction (NWP) models completely missed the forecast of this storm. Following the approach of Marra et al. [10], which takes into account all available ground- and space-based observations to analyse the event, in this Chapter the main features of the storm are estimated, using the data coming from many different instruments, that are reported below in Section 2.1. This good availability of data allows also to compare together different methods to compute our estimations.

2.1 Observational dataset description

In this thesis work the following instruments and datasets are employed:

1) ERA5 reanalysis dataset

ERA5 dataset is the fifth generation ECMWF (European Centre for Medium-Range Weather Forecasts) for atmospheric reanalysis of the global climate, covering the period from January 1950 to present. ERA5 reanalysis is produced by the European Centre for Medium-Range Weather Forecasts (ECMWF), providing hourly data on many atmospheric, land-surface and sea-state parameters together with estimates of uncertainty. Reanalysis combines past observations with models to generate consistent time series of multiple meteorological variables and provide, on 3D grids at sub-daily intervals, a comprehensive description of the state of the atmosphere. The obtained datasets form a regular system of grids whose size and characteristics depend on the specific required application. Starting from an adequate base of observations, the reanalysis is able to generate meteorological datasets with the following characteristics:

- a complete coverage of the Earth system

- elimination or reduction of spatial and temporal discontinuities and inhomogeneities.

ERA5 data are available in the Climate Data Store on regular latitude-longitude grids at $0.25° \times 0.25°$ resolution and a temporal frequency of one hour. For this thesis, a dataset on 14 pressure levels is used: 1000 hPa, 950 hPa, 925 hPa, 850 hPa, 800 hPa, 750 hPa, 700 hPa, 650 hPa, 600 hPa, 500 hPa, 400 hPa, 250 hPa, 200 hPa and 100 hPa. The meteorological variables extracted from this dataset are: the relative humidity (%), the horizontal wind components (m/s), the vertical velocity component (Pa/s), the temperature (K), the specific humidity (kg/kg).

2) Ground radar

The operational dual polarization weather radar located in Monte il Monte, Abruzzo (41.94°N, 14.62°E, 710 m ASL) managed by the Civil Protection Department of Italy. Weather radars work by emitting microwaves into the atmosphere; part of this beam of energy bounces back and is measured by the radar, providing information about the observed volume of atmosphere. The quantity that is actually measured by the radar is the backscattered energy, which depends on the size, shape, aspect, and dielectric properties of the targets in atmosphere through the sixth moment of the hydrometeors size distribution (*reflectivity factor*) in the scanned volume. Reflectivity factor Z is measured in $\mathrm{mm}^6/\mathrm{m}^3$; however, the values of the reflectivity factor cover a wide range, hence they are commonly expressed in dBZ, a logarithmic dimensionless unit.

Precisely, the radar in Monte il Monte is a C-band polarimetric radar, since it works at microwave frequencies between $4.0 - 8.0$ GHz at two different polarizations of the beam. In this thesis, we will only deal with measurements of reflectivity factor at horizontal polarization (Z_h). The acquisition geometry is based on a scanner of the atmosphere for sequence of 12 conical sweeps at the elevation angles of 0.5°, 1.5°, 2.5°, 3.5°, 4.6°, 5.5°, 7°, 9°, 11°, 13.5°, 16° and 90°. For each elevation angle, the radar performs a scanning on a range of 360° in azimuth with 1° spacing (Plan Position Indicator (PPI) mode). The radar can also scan along the vertical at fixed azimuth angles, in the so-called Range Height Indicator (RHI) mode (this however won't be used in thesis). Furthermore, the radar can work in Doppler mode, by sending a microwave signal towards a desired target and analyzing how the object's motion has altered the frequency of the returned signal (Doppler effect). This is useful to measure the radial component of the velocity of hydrometeors relative to the radar. Due to the interception of radar beam by the peaks of the Apennines range, measurements from the lowest elevation angle (0.5°) are blocked, hence the data at this elevation are neglected. The measurements are taken starting from elevation angle of 1.5°. The range resolution is 150 m for all the elevation angles. Data are available from 08:00 UTC to 11:55 UTC with a mainly frequency of five minutes. In some cases there are time gaps of 10 minutes and this happens between 08:20 and 08:30, 09:40 and 09:50, 10:30 and 10:40, 10:55 and 11:05, 11:10 and 11:20, 11:35 and 11:45. Anyway, in this thesis we focus primarily on data between 08:00 UTC and 09:00 UTC.

3) Global Precipitation Measurement mission Core Observatory (GPM-CO)

The GPM-CO is a joint mission between JAXA and NASA and consists of an international network of satellites carrying an advanced radar/radiometer system to measure precipitations and hydrometeors from space at different frequencies, and serves a reference standard to unify precipitation measurements from a constellation of research and

operational satellites. Among the instruments used by the GPM-CO, there are the GPM Microwave Imager (GMI) and the Dual-frequency Precipitation Radar (DPR). Only the first one is used in this thesis. The GMI offers the richest set of microwave frequencies available, from March 4th 2014, with ten dual polarization (horizontal and vertical) window channels at 10.6, 18.7, 36.5, 89, and 166 GHz, and three single polarization water vapor absorption channels, one at 23.8 GHz and two at 183.31 GHz. The GPM Microwave Imager (GMI) has a swath 550 miles (885 kilometers) wide. In this thesis, we use only the one at 183.31 ± 3 GHz, vertically polarized, due to its better sensitivity to large ice particles [10]. The dataset is downloaded from [46]. The spatial resolution at this frequency in the region of interest is approximately 7.2 km in the direction of flight of the satellite (cross-scan direction in Fig.2.1) and 4.4 km in the along-scan direction. Luckily, the GPM-CO captured the hailstorm at its mature stage, at 08:47 UTC at 40.79°N, 13.86°E on a descending orbit (from North to South), when the most intense portion of the storm was approaching the coast of Naples.

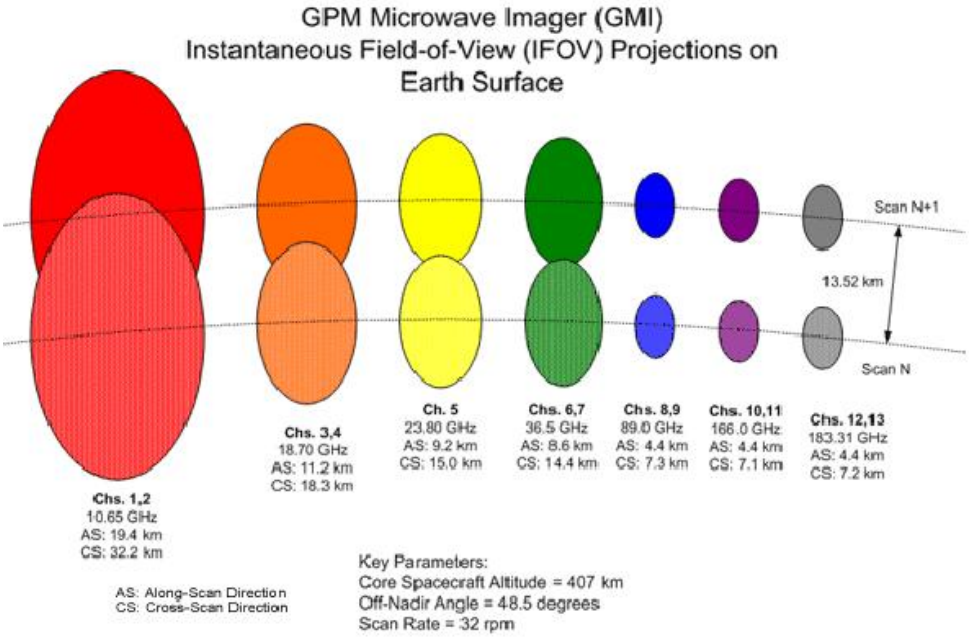

Figure 2.1: Dimensions of the Instantaneous Field-of-View (IFOV) for GPM-GMI (IFOV determines the footprint on the Earth soil from which an individual detector of the satellite captures radiance). Image from NASA GMI site.

4) European Severe Weather Database (ESWD): the ESWD, provided by the European Severe Storms Laboratory (ESSL), is used to get the values of the diameter of the hailstones collected at the ground during the event, that are used as a proxy to retrieve the maximum updraft velocity.

2.2 Updraft and background environment analysis

This Section illustrates the estimations of the fundamental features of the storm, using the instruments presented above. Much of the analysis in this section starts and develops from the work of Marra et al. [10] and Guidetti [14], who focused on the technical description of the Naples storm. The analysis in this Section will be crucial for the imposition of initial and boundary conditions of the numerical simulation (ICs and BCs). The specification of

proper ICs and BCs in the numerical resolution of Partial Differential Equations (PDEs), as the Navier-Stokes Equations, is essential in order to have a well-posed problem. If too many ICs/BCs are specified, there will be no solution, while if too few are specified, the solution will not be unique. Even if the number of ICs/BCs is right, but they are specified at the wrong place or time, the solution will be unique, but it will not depend smoothly on ICs/BCs. In any of these cases, the problem will be ill-posed and there won't be any chance for the integration to work [47]. Thus an accurate setting of ICs and BCs has to be considered as a crucial step for the following numerical solution.

According to Marra et al. [10], the storm started developing before 06:00 UTC (precisely, at 05:57 UTC) over the Tyrrhenian Sea off the coast of Naples and reached the equilibrium level by 06:17 UTC, hitting the coast around 09:00 UTC and moving inland afterwards until its complete dissipation around 12:00 UTC. Fig.2.2 illustrates a timeline of the event taken from [10], made from Meteosat Second Generation (MSG) Spinning Enhanced Visible and Infrared Imager (SEVIRI) data at 10.8 μm (IR) channel, with 3×3 km resolution at nadir. These data are used to look at the cloud top structures and analyze of the cloud life. According to Guidetti [14], the first observation of the vortices from ground radar is approximately at 08:00 UTC and the system reaches a quasi-stationary state during its mature stage in the 08:00-09:00 UTC interval, when the center of mass travels at almost constant speed following a very straight path. Then, the storm strikes the land and starts showing a more irregular behaviour until its dissipation.

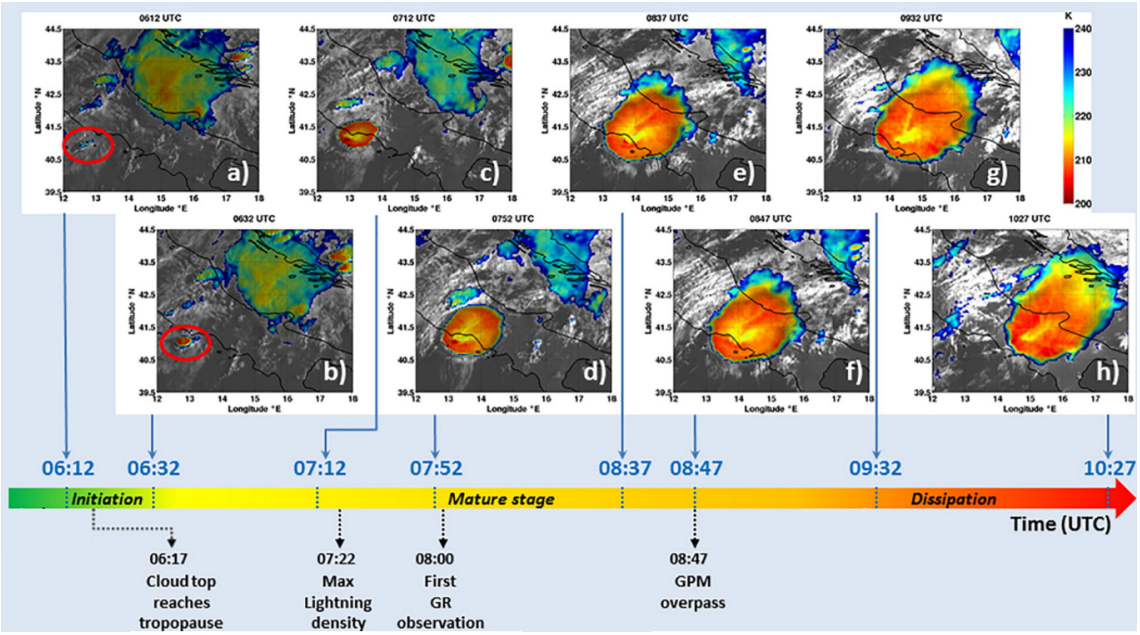

Figure 2.2: edited from Fig.2 in Marra et al. [10]. Sequence of eight MSG snapshots depicting different storm evolution phases at (from left to right) 06:12 UTC, 06:32 UTC, 07:12 UTC, 07:52 UTC, 08:37 UTC, 08:47 UTC, 09:32 UTC, 10:27 UTC. Red circles indicate early development of the cell. A time-line at the bottom of the eight panels indicates key features in the storm development and observations available throughout the storm evolution. GR stands for Ground Radar.

2.2.1 Updraft velocity

Firstly, we focus on the estimation of the updraft velocity. Direct observations of the updraft speed are a rather challenging task, since a few instruments can be introduced

successfully into the supercell updrafts, due to extreme conditions. Thus, despite supercell updrafts' importance for atmospheric processes, these have seldom been observed in situ. The first of these infrequent in situ observations came from armored aircraft penetrations through the WERs (Marwitz [18]). These observations were usually made near cloud base and in the inflow air ahead of the supercell and were typically taken in the High Plains of the United States and Canada. These initial estimations generally resulted in the $15/30\,\mathrm{m\,s^{-1}}$ range, a large underestimation of the real velocities of many updrafts. In situ estimates of updraft velocities can also be achieved via releasing sensors or trackable objects into supercell updrafts from the storm's proximity. Chaff packets have been released from aircraft at thunderstorms' cloud bases and tracked with radar to estimate vertical velocities within supercells. Results from this approach have generally been consistent with those from in situ aircraft penetrations [18]. Radiosondes have also been used throughout the past 50 years to estimate the vertical velocities in supercells, from the early work by Davies-Jones [48] to the more recent study in Martinescu et al. [49], providing some of the most precise measurements of updraft speed. Finally, due to the previous mentioned challenges associated with in situ observations, remote sensing measurements with Doppler radars have been largely employed to determine the horizontal components of the wind, and then using the mass continuity equation to calculate the vertical component, which is the updraft estimation.

Unfortunately, no in situ observations data are available for the Naples storm, due to the absence of radiosounding sites in the proximity of Naples (the closer one is located in Pratica di Mare, Rome, more than 100 km north) and also due to the storm evolution which develops mainly over the sea and far from the land. Furthermore, the inflow region of the supercell is located behind the highest reflectivity zone (FFD) respect to the position of the ground radar in Monte il Monte. This results in a strong attenuation of the radar beam due to the high water content in the FFD, causing a poor description of the updraft behind. Consequently, the Doppler measurements result very noisy, affected by strong attenuation and thus not efficiently usable for precise estimations of velocity. Therefore, it is necessary to analyze different indicators to retrieve approximately the updraft speed. A number of approaches is possible, based upon the available instruments and measurements:

a) Cloud top cooling rate

The cooling rate of the cloud top observed from the SEVIRI IR data in the first stages of growth of the storm cloud. This approach is explained and applied in Marra et al. [10] and is based on the assumption that the rising speed of the cloud during its initial growth is comparable to the vertical velocity of the wind inside the cloud itself. As computed in [10], the cooling rate of the updraft top is estimated by SEVIRI around $1\,\mathrm{K\,min^{-1}}$ at the beginning and reaches its maximum of $4.5\,\mathrm{K\,min^{-1}}$ around 06:02 UTC, that, compared to the radiosounding of Pratica di Mare, yields an estimate of the updraft speed around $11.8\,\mathrm{m\,s^{-1}}$. However, due to satellite uncertainties this is an underestimation of the real updraft speed, which is then corrected in [10] following Adler and Fenn [50], giving a final estimation of $v_{max} \sim 50\,\mathrm{m\,s^{-1}}$.

b) Hailstones size

Hailstones size observed at the ground is an important proxy for the estimation of the updraft maximum speed able to hold up such hydrometeors before they fall downward. The first coastal areas struck by the storm in its mature stage were the surroundings

of Pozzuoli (NA), where hailstones with maximum diameters of 11/12 cm were reported in the European Severe Weather Database (ESWD). These values, exceptional for the Mediterranean basin, conform to the ones observed in the strongest High Plains supercell storms in the USA. Small hailstones, trapped in the strong updraft, can grow by means of a process called riming, which basically takes place when the environment surrounding the hailstones is rich of supercooled droplets, that are liquid droplets of few tens of micrometer radius which can survive in a metastable state at temperature well below 0°C (even below −30°C). However, as soon as one of these droplets touches a solid particle, the delicate equilibrium is broken and the drop quickly freezes on the solid substrate. Due to the high latent heat release during the droplet freezing, the temperature of the substrate can locally exceed 0°C, opposing the complete freezing of the supercooled drop. Depending on the environmental conditions found by the hailstone during its life inside the cloud and on the ability of the solid substrate to dissipate rapidly the excess of heat, the riming growth can be classified as dry (if finally all the supercooled water freezes) or wet (if some water remains trapped in the solid substrate without being able to freeze completely). Generally, the hailstones growth mainly develops as wet-type, resulting in highly dense hydrometeors ($\sim 0.9\,\mathrm{kg\,m^{-3}}$). This growth process can continue until the hailstone can be held up by the strong updraft currents, before it becomes too heavy and finally falls downward. Therefore, by observing the maximum sizes of the hailstones at the ground it is possible to get an indirect estimation of the maximum updraft speed, which is given by the terminal velocity V_T of those hailstones in air. Since the motion of those large hydrometeors is highly turbulent ($R_e \sim 10^5$), no analytical formula can be obtained to relate their dimension to V_T, so empirical relationships have been found to express V_T as function of hailstones diameter. Following Heymsfield and Wright [51], in this work the underlying empirical formula has been used, valid for wet-grown particles with density $0.9\,\mathrm{kg\,m^{-3}}$:

$$V_T = 1207^{\,0.64} \tag{2.1}$$

with D hailstone diameter in cm and V_T in $\mathrm{cm\,s^{-1}}$. For the largest hailstone observed in the Naples storm, $D = 12\,\mathrm{cm}$, we obtain $v_{max} = V_T \sim 59\,\mathrm{m\,s^{-1}}$, which is also the maximum updraft speed estimated by this method. Finally, it is important to remark that, during the fall, the hailstones can find themselves in warmer environments at low levels, where temperature rises above the freezing level and melting can occur. This results in a slightly smaller size of the hailstones at the ground if compared to the upper levels of the cloud, so that in the Naples storm maximum stones dimensions could have exceeded a bit $D = 12\,\mathrm{cm}$. However, even if this process surely took place, we expect that, due to the evolution of this system in the early morning and the so large dimension of the storm core, the temperature under the supercell downdraft should have been notably low and should not have reduced much hailstones dimension by the time they touched the ground.

3) Convective Available Potential Energy (CAPE)

One more approach used to deduce indirect estimations of the maximum updraft speed is the calculation of the Convective Available Potential Energy (CAPE), as defined in Eq.1.1. The CAPE can be recognized more easily as the net positive area on a pseudo-adiabatic chart. Precisely, the area enclosed between the environment virtual temperature profile and the moist adiabatic curve followed by the rising parcel, between the LFC and EL, on a chart with temperature as the abscissa and height (or log pressure) as the ordinate, such as the SkewT-logP chart. If once the parcel reaches the EL all the available potential energy is converted into kinetic energy, then the maximum updraft speed can be

simply estimated as:

$$w_{max} = \sqrt{2\,CAPE} \tag{2.2}$$

As we explained below, this is an upper limit to the updraft velocity, which is usually not registered, since we have neglected in this calculation the contribution of many factors:

- no mixing with the environment, thus the entrainment of cold air into the updraft is not considered
- negligence of vertical perturbation pressure
- no hydrometeors are admitted
- no frictional forces

Among all these processes, the one that usually contributes more to slow down the vertical velocity is probably the entrainment of cold air. Therefore, we will take into account for this process in order to have a more accurate estimation.

Generally, in order to perform CAPE calculation, as well as the evaluation of the CIN, LFC, EL and other relevant meteorological quantities, is necessary to start from the data collected by a radiosounding of the atmosphere. It consists in a sounding balloon released at the ground level, equipped with many sensors, that typically travels up to an altitude of $25 - 30$ km before exploding and falling via parachute. Radiosoundings obtain direct measurements of the vertical profiles of basic meteorological quantities. Thanks to this information, radiosoundings turn out to be extremely useful to provide the initial conditions needed by the physical-mathematical models developed for weather forecasting. However, the radiosounding nearest to the area interested by the storm was performed in Pratica di Mare at 00:00 UTC, almost 6 hours before the development of the supercell and more than 100 km north. Therefore, we consider these data unrepresentative of the real environmental conditions in which the storm evolved.

In order to get more useful data for our purpose, following the work of Guidetti [14], a pseudo-radiosounding is reproduced using the pressure levels ERA5 reanalysis data, fixing a point at certain latitude and longitude and extracting the corresponding vertical profile of the previously mentioned variables (Fig.2.3). The calculation of CAPE is obtained through the discretization starting from the MATLAB code written by Guidetti, but implementing some relevant refinements.

- a different ERA5 grid point is chosen, at [41°N, 13.25°E], closer to the storm core path when it approached the coast of Pozzuoli. The pseudo-radiosounding is performed at 06:00 UTC, almost 2 hours before the arrival of the storm, in order to avoid possible perturbations in the vertical profile of the variables due to the presence of the storm itself.
- a virtual correction on temperature is included, namely in the calculation of CAPE is used the virtual temperature as written in the definition in Eq.1.1, instead of the mere absolute temperature as done in [14]. This more accurate correction generally contributes to increase slightly the value of CAPE. Note that the ERA5 reanalysis provides data for specific humidity q, that has to be converted to water vapor mixing ratio w in order to apply Eq.1.1, using the following simple expression:

  $$w_{p,e} = \frac{q_{p,e}}{1 - q_{p,e}} \tag{2.3}$$

  where p and e stand for parcel and environment.

- the contribution of entrainment is included, computing the so-called Entrainment CAPE (ECAPE). Substantial mixing occurs between the updraft and the surrounding comparatively dry environmental air, through a process called entrainment. Entrainment controls thunderstorm intensity via its diluting effect on the buoyancy of air within the updraft. Following Peters et al. [52], the formula used to compute ECAPE is:

$$ECAPE = \frac{CAPE - \frac{\eta EL}{2} NCAPE}{1 + \frac{\eta EL}{2}} \tag{2.4}$$

where:

$$NCAPE = -\int_{LFC}^{EL} \frac{g}{c_p T_e} \left(\frac{1}{z} \int_0^z h_e \, d\tilde{z} \; - \; h_e \right) dz$$

$$h_e = c_p T_e + L_v q_e + gz$$

$$\eta = \frac{2k^2 L_{mix}}{P_r R^2}$$

CAPE is computed as in Eq.1.1, h_e is the moist static energy of the environment and $L_v = 2.26 \cdot 10^6 \, \mathrm{J\,kg^{-1}}$ is the water latent heat of vaporization. $k^2 = 0.18$ is the square of von Karman constant, $L_{mix} = 120 \, \mathrm{m}$ is the turbulent mixing length scale, $P_r = 1/3$ is the turbulent Prandtl number: these last three values are chosen in agreement with [52]. R is the updraft radius which is selected in agreement with the following Section 2.2.2.

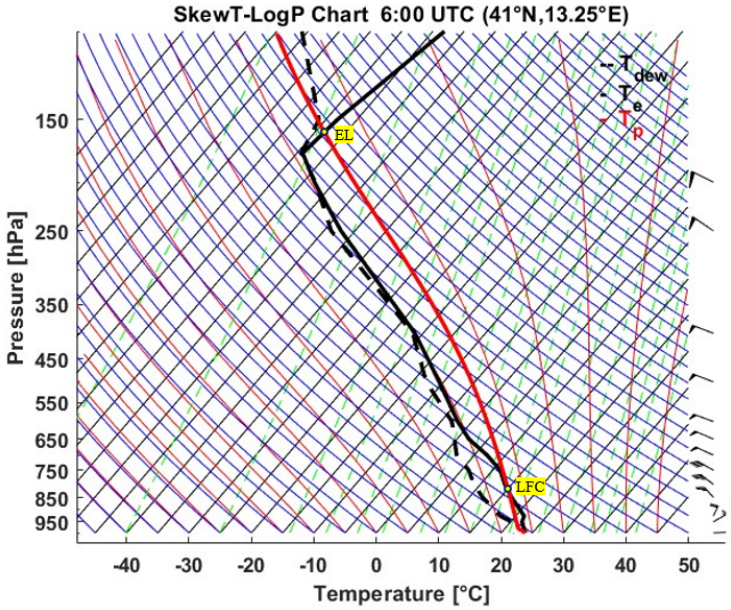

Figure 2.3: Figure 4.5: SkewT-LogP chart at [41°N, 13.25°E]: on the horizontal axis there is the temperature, while on the vertical axis the logarithm of pressure is represented. In background of the chart: black solid lines are isotherms, blue solid lines are the dry adiabatic ones, red solid lines are the saturated adiabatic ones and green dashed lines are the lines at constant humidity. In the foreground: the black solid bold line is the vertical temperature profile, the black dashed bold line is the dew point temperature vertical profile and the red solid bold line is the convective rise of an air particle. On the right side of the chart are reported the wind barbs. Highlighted in yellow the Level of Free Convection (LFC) and the Equilibrium Level (EL).

With these implementations, using an updraft radius of $R = 10\,000\,\text{m}$, roughly in agreement with the results in Section 2.2.2, it is possible to obtain a value of ECAPE $\sim 2250\,\text{J}\,\text{kg}^{-1}$, which, even if not extreme, reflects a strong instability of the environment over the Tyrrhenian Sea in the early morning. Applying Eq.2.2 substituting CAPE with ECAPE, gives a final value of $w_{max} \sim 67\,\text{m}\,\text{s}^{-1}$.

To sum up, the results of the three different methods are reported below:

Method	Cooling rate cloud top	Hailstones size	ECAPE
$\boldsymbol{w_{max}}$ **(m/s)**	~ 50	~ 59	~ 67

Table 2.1: Maximum updraft velocity estimated from three different methods.

These results of maximum updraft velocity obtained with three completely different methods are in good agreement together. The smaller value of w_{max} computed with cloud top cooling rate can be justified considering that this estimation is made in the first stages of growth of the cloud, about two hours before the first observation of von Karman vortices. Generally the maximum updraft speed during the lifetime of a supercell storm is observed in the mature stage (e.g. see Fig.2 from [31]), so this value of w_{max}, which refers to the early growth, is reasonably a bit lower than the other two estimations. Furthermore, also the results obtained with hailstones size and ECAPE, which both refer to the mature stage of the storm, differ of a few meters per second ($\sim 10\%$). Despite this small difference could be justified with inevitable uncertainties inherent in these two methods, we can also observe that it is also in agreement with the process of hailstones melting described before. Due to this phenomenon, we expect hailstones measured at the ground level to be slightly smaller than the ones at higher altitude where the updraft peaks. Thus, using a bit larger value for the hailstones diameter than the one of $D = 12\,\text{cm}$ in Eq.2.1, we can obtain a higher maximum updraft speed, very similar to $w_{max} = 67\,\text{m}\,\text{s}^{-1}$ computed with ECAPE. In light of these investigations, we conclude that the three measurements are consistent with each other and we can therefore give as final estimation of the maximum updraft speed the value obtained with ECAPE: $w_{max} = 67\,\text{m}\,\text{s}^{-1}$.

2.2.2 Updraft width

Another essential parameter to estimate accurately is the width of the rising updraft. As for the previous case of updraft velocity, also for width estimation different methods have been applied in literature, depending on the available instruments. In contrast to updraft speed measurements, now in situ observations as radiosoundings or aircaft flights turn out to be less useful since they often provide local measurements, while updraft width often extends for many kilometers. Therefore, remote sensing instruments are best suitable for this kind of analysis:

1) Ground Radar Reflectivity

The most classical approach is applied by means of ground radar observations, which can provide a precise measurement of updraft width by using reflectivity Z. This quantity gives information about the water content of the cloud and thus an estimation of the Weak Echo Region of the supercell, which appears as an area of low or zero reflectivity. Combined information from PPI and RHI mode scans at different angles results in an evaluation the dimension of the WER, that is a reasonable assessment of the updraft area.

This approach has a long tradition in meteorology, starting from the early investigations by Marwitz [18] to more recent automatic identifications by Shi et al. [53]. Unfortunately, as pointed out before, the updraft is located behind the FFD of the supercell respect to the position of the ground radar in Monte il Monte, so that the radar beam suffers of strong attenuation due to the high concentration of hydrometeors along the path. This results in a very poor description of the WER, combined with the fact that, during the vortex shedding, the storm is situated almost at the end of the radar range of observation ($\sim 150\,\text{km}$) and the data at elevations $\geq 3.5°$, which could be very useful in this case, are not available for such distance. We conclude that ground radar reflectivity measurements are not best-suited for the updraft width estimation in this case study.

2) Overshooting Top Area

With the advent of more widespread satellite measurements, as the ones provided by the previous mentioned GPM mission, other approaches have been promoted to perform updraft width estimation from cloud top features. More precisely, simulations and physical reasoning indicated a robust correlation between midlevel updraft area and the horizontal Overshooting Top Area (OTA) measurable from satellite, as suggested in Marion et al [54]. OTA can be obtained by looking at the brightness temperature (T_B) measured from satellite at a certain frequency band, which should be sensitive to cloud top properties ascribable to the strong updraft (such as the presence of large hail) and possibly not affected much by the background surface. For this purpose, the higher frequency GMI band at $(183.31 \pm 3)\,\text{GHz}$ is selected, due to its better sensitivity to large ice particles, that are expected to populate especially the OT region (data available at NASA GES DISC site). In this band, the ground appears as a very hot area while the storm is well detectable as a cold spot (Fig.2.4a). Furthermore, while the T_Bs at 166 GHz and, to a less extent, at $(183.31 \pm 7)\,\text{GHz}$ penetrate deeper in the cloud and receive a marked signal from ice even under the anvil, the T_B at $(183.31 \pm 3)\,\text{GHz}$ is sensitive to the higher cloud layers only [10]. The GMI overpass is at 08:47 UTC, inside the time interval of 08:00-09:00 UTC when the system undergoes a quasi-stationary evolution.

Once obtained the data from the selected band, the method developed in [54] for the OTA estimation is applied. Precisely, it establishes to select the minimum T_B pixel and, moving radially from it, to compute the 1D second derivative along the radial direction r at different angles (scheme in Fig.2.4b), using a simple finite difference approximation:

$$\frac{d^2 T_B}{dr^2} \longrightarrow \frac{T_B^{n+1} - 2T_B^n + T_B^{n-1}}{\Delta r^2} \tag{2.5}$$

The edge of the OT along each radial direction is defined as the first point where the second derivative becomes negative, in other words we are looking for the inflection points of the T_B field around the OT. This process is repeated along four different orthogonal radial directions and finally computing a mean of the four different values obtained in order to have an optimal estimation of the OT radius. Since the coordinates of the pixels are given in degrees in latitude and longitude, it is necessary to convert them into kilometers. This is done by using the calculation in Eq.3.9 and Eq.3.10 in Guidetti thesis [14], where the eccentricity of the Earth is taken into account in order to find the most suitable degree-km relation for the specific latitude at which the storm developed. The following conversion is obtained:

$$\Delta^{\text{km}}_{\text{lat}} = R\,\frac{\pi}{180}\,\Delta^{\circ}_{\text{lat}} \qquad \text{with } R = 6362.92\,\text{km} \tag{2.6}$$

$$\Delta^{\text{km}}_{\text{lon}} = r\,\frac{\pi}{180}\,\Delta^{\circ}_{\text{lon}} \qquad \text{with } r = 4821.43\,\text{km} \tag{2.7}$$

Due to the finite size of the pixel, a non negligible error is made on the updraft radius estimation. Given that the T_B has a constant value all over the pixel, we can assume for simplicity that the true position of the OT edge (along each direction) is uniformly distributed all over the pixel. Thus, the error on the OT radius (along each i^{th}-direction) is given by the standard deviation of the uniform distribution, multiplied by $\sqrt{2}$ because the error affects both the estimation of the edge and the estimation of the OT centre: $\sigma^i_{rad} = \sqrt{2}\,(pix^i_{width}/\sqrt{12})$, where pix^i_{width} is the width of the pixel in km along the i^{th}-direction. Then the error of the mean of the four radii, each one with its error, is given by:

$$\sigma^{tot}_{rad} = \frac{1}{N}\sqrt{\sum_{i=1}^{N}(\sigma^i_{rad})^2} \quad \text{with } N = 4 \tag{2.8}$$

Multiplying by two the mean radius and its error computed with Eq.2.8, we finally obtain an estimation of the updraft width (diameter): $D_u = 22 \pm 3\,\text{km}$. All these calculations are done by means of a MATLAB code.

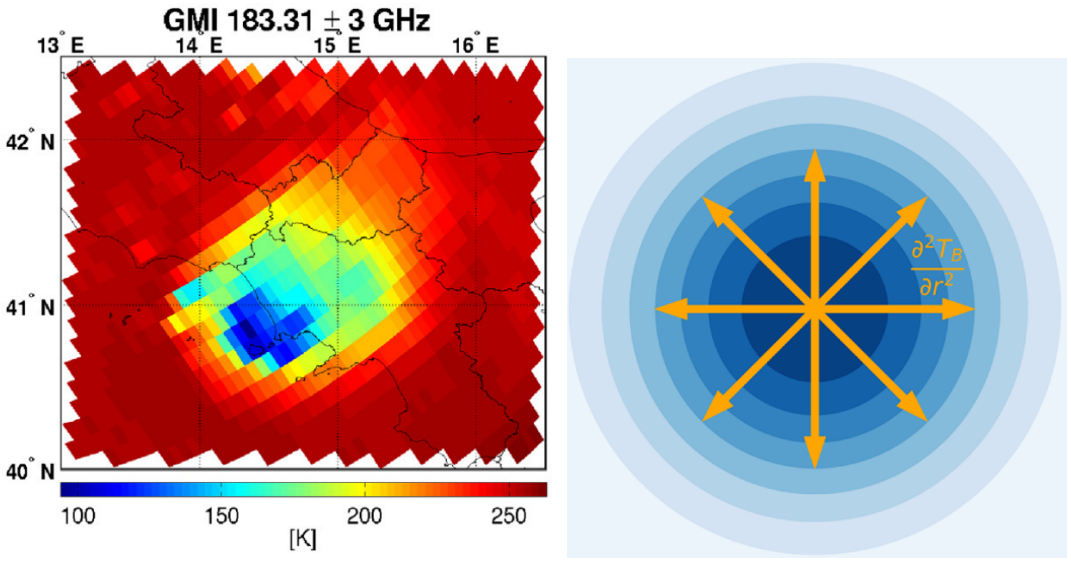

(a) (b)

Figure 2.4: Fig.2.4a: brightness temperature plot from GMI data at 183.31 ± 3GHz (taken from [10]). Fig.2.4b: diagram of the approach used to compute the overshooting top area from the second derivative of T_B (taken from [54]).

3) Ground Radar Doppler Velocity

Finally, as for the updraft velocity estimation, also in the case of updraft width Doppler velocity measurements can give important information, since they detect the relative radial velocity between the observed hydrometeors and the ground radar. This method is very suitable in order to measure the rotating components of the cloud, which appear as regions with a sharp change in the sign of the radial velocity, being negative where winds are going towards the radar and positive where winds are blowing away from the radar. Thanks to this mode of operation, Doppler radars are also able to distinguish easily between cyclonic and anticyclonic rotation, so they result very useful to detect the dimension of supercell mesocyclone, where the rotating updraft is located (e.g. French et al. [55], Snyder et al. [56]). This can be then considered an almost direct measurement of updraft width. However, as pointed out previously, the Doppler data for the ground radar turn out to

be very noisy and hardly useful for precise measurements. Anyway, it is possible to use these data to confirm qualitatively the previous estimation given from GMI. Therefore, we plot the radar Doppler velocity (m/s) at 08:30 UTC, in the middle of the window 08:00-09:00 UTC that we consider for the analysis. The results are plotted in Fig.2.7. From the image is possible to observe the typical Doppler signal from a cyclonically rotating cloud, identified with the black rectangle. This is coherent with the expectations, since the storm is right-moving which implies the presence of a cyclonic mesocyclone, as explained in Chapter 1. Then we manually select the two points along the direction of maximum extension of the mesocyclone and compute their distance with Eq.2.6 and Eq.2.7, obtaining a rough estimation of $\sim 21.6\,\text{km}$, coherent with D_u.

To sum up, the final updraft width estimation obtained from the different available instruments is $D_u = 22 \pm 3\,\text{km}$, which is a really high value, bigger than powerful supercell storms observed in the USA (Wang [57] Table 1). This should be considered as a maximum updraft extension; clearly, the vertical velocity w_{max} is approximately reached only in the updraft core, which is inevitably smaller than D_u.

2.2.3 Crossflow velocity

The crossflow velocity is a crucial quantity for the system, because it should be critical for the development of vortices in the wake. We perform the estimation of the crossflow velocity in the steady reference frame of the Earth surface and then transform the result in the reference frame of the supercell center-of-mass (CM). This will be useful for the numerical simulation: due to the movement of the supercell, the numerical simulation is performed in the CM reference frame of the storm, in order to simplify the description and avoid the escape of the system from the computational domain.

The crossflow estimation is carried out starting from the ERA5 reanalysis, reproducing a pseudo-radiosounding using the pressure levels data as we did before concerning the CAPE calculation. Precisely, we are interested now in wind velocity and direction data at all the different pressure levels. In order to select the appropriate ERA5 grid points to extract the vertical profiles, we firstly decide to estimate the direction of motion of the shedding vortices observed from ground radar reflectivity data. This is important to give a qualitative evaluation of the streamwise and spanwise directions of the wind, where with "streamwise" and "spanwise" we mean respectively the direction parallel and orthogonal to the direction of the vortices. However these directions change slightly during the storm approach to the coast and also a proper identification of the center of each vortex is quite complex, thus a rigorous calculation could be very challenging and cumbersome. Therefore, we prefer to give a rough estimation by manually selecting the optimal streamwise direction looking at the radar frame at 08:00 UTC, that is at the beginning of the period under consideration. In this frame, the supercell wake is almost perfectly aligned on the direction of the radar beam, which is easy to compute. It results that the streamwise direction points North-East, with an angle of 45° respect to the zonal direction.

Then we select three ERA5 grid points aligned in the spanwise direction ([40.75°N, 13.25°E], [40.5°N, 13.5°E], [40.25°N, 13.75°E]), immediately upstream the supercell using data at 08:00 UTC: they identify a vertical plane normal to the streamwise direction. Then the vertical profiles of the wind are extracted on each grid point, decomposed onto the streamwise and spanwise direction, and averaged over the three different points. Thus we finally obtain one vertical profile for the streamwise component and one for the spanwise component of the wind, which are taken as our best estimations (see Fig.2.5). The errors are simply computed as the standard error of the mean.

As will be explained better in Section 2.3, the radar images show clearly the presence of

vortices at 1.5°, 2.5°and 3.5°of elevation (see Fig.2.9), that roughly correspond to a thick layer of atmosphere from 3 km to 10 km height (considering the effect of Earth curvature, given that the wake of the supercell lies 100/150km far from the ground radar position). Coherently with the radar images, we decide to estimate a constant value for the crossflow in this layer. We extract an average of the velocities at three levels of ERA5 data that completely fall inside this vertical layer, precisely the ones at 400, 500 and 600 hPa (points A, B, C in Fig.2.5). This average provides the final estimation of the crosswind vector V_{wind} in the reference frame of the Earth surface.

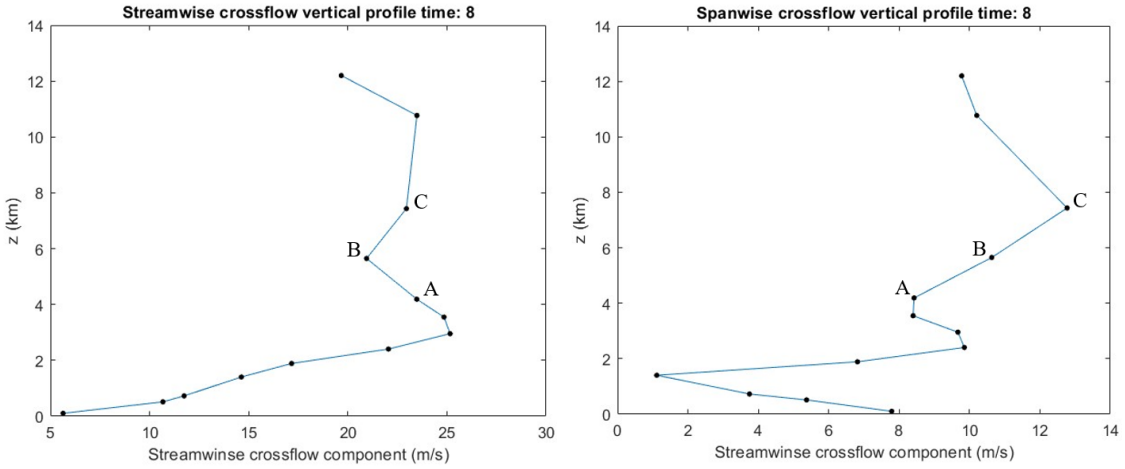

(a) (b)

Figure 2.5: Streamwise (Fig.2.5a) and spanwise (Fig.2.5b) components of tropospheric crossflow.

Now this result is converted in the supercell CM reference frame: in order to do so, an estimation of the center-of-mass velocity V_{CM} is crucial. This calculation is performed with the data taken from Guidetti's thesis [14] obtained through the radar reflectivity analysis. An average of the CM velocity values is computed on the time interval between 08:00 UTC and 09:00 UTC and adding a correction due to the conversion from pixel to km. Finally, the wind vector in the CM reference frame (V^{CM}_{wind}) is computed from V_{wind} with the Galilean Transformations. For a good estimation, we should obtain that the direction of propagation of the vortices should almost coincide with the one of V^{CM}_{wind}. The different vectors are shown in Fig.2.6.

The results are reported in Tab.2.2, where the angles are computed respect to the spanwise direction (the abscissa of the Cartesian axes in Fig.2.6). The errors of the wind components and angles in the CM reference frame are computed with the stochastic errors propagation formula.

V_{wind} (m/s)	α_{wind} (°)	V_{CM} (m/s)	α_{CM} (°)	V^{CM}_{wind} (m/s)	α^{CM}_{wind} (°)
24.8 ± 0.7	65 ± 2	14.3 ± 1.0	47.1 ± 0.4	12.0 ± 1.0	86 ± 6

Table 2.2: Cross-flow values with corresponding errors. Angles are computed respect to the spanwise direction (thus, 45° is exactly the East direction).

The results show a good agreement between the direction of V^{CM}_{wind} and the direction of propagation of the vortices (that is, the streamwise one), because the angle α^{CM}_{wind} formed

by V_{wind}^{CM} differs less than 1 standard deviation from 90°. This is important also to check the rationality of our initial estimation of the streamwise direction.

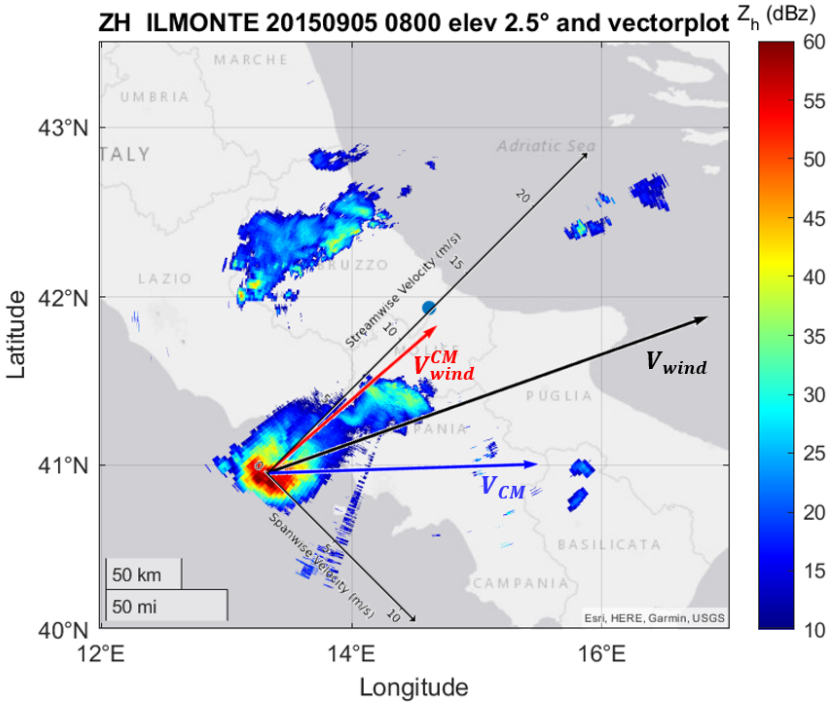

Figure 2.6: Vector plot of the center-of-mass velocity V_{CM}, environmental wind velocity from ERA5 V_{wind} and environmental wind velocity in the CM reference frame V_{wind}^{CM}. In the background, the reflectivity plot from ground radar data at 08:00 UTC. The blue dot in the middle of the figure represents the position of the ground radar.

2.2.4 Updraft rotation

Another relevant features of supercell storms, as explained in Chapter 1, is the rotation of the updraft with the formation of a mesocyclone. The estimation of the magnitude of this rotation can be performed through the Doppler radar data which have already been presented for the calculation of the updraft width. This task is very challenging due to the bad quality of Doppler data available, and the uncertainty is large. We focus on the region where the mesocyclone appears on the south flank of the supercell core, where an evident cyclonic rotation can be isolated from the surroundings. The data for this analysis are taken at 08:30 UTC at 2.5° of elevation in PPI mode, and represent the relative *radial* velocity of the hydrometeors and the ground radar. In Fig.2.7, the area of analysis is framed by the black rectangle, which is selected manually and covers an area between [40°40′N,40°55′N] and [13°40′E,14°00′E]. Inside this box, we distinguish the pixels with negative velocity and the ones with positive velocity, and perform an arithmetic mean of the velocities in these two groups separately. These two values, obtained in the Earth reference system, are the estimations of the mean radial velocity of the wind moving, respectively, towards and away from the radar in the mesocyclone region.

We can also compute these two values in the CM reference frame as we did for the environmental wind velocity. This requires an estimation of the radial component of CM velocity V_{CM} at 08:30 UTC. The magnitude of $V_{CM} = 14.3 \pm 1.0$m/s is fairly constant during the period of analysis, so we only need to estimate the direction passing through the supercell CM and the radar at 08:30 UTC, in order to decompose V_{CM} along that

direction. The CM position is easily obtained from Guidetti data used for the estimation of V_{CM}, while the radar position is fixed at [41.94°N, 14.62°E]. This calculation reveals that at 08:30 UTC the supercell is moving towards the radar at 6.8 ± 0.5 m/s. This value is finally subtracted from the previous estimations of updraft rotation computed in the Earth reference system, using the simple Galileian Transformations. Therefore we obtain two quantities that represent the mean *tangential* velocity of rotation for the right and left flank of the updraft, respect to the updraft core, and call them $V^r_{rot} = 19 \pm 5$ m/s and $V^l_{rot} = 29 \pm 6$ m/s. These values are affected by very large errors (computed as the error of the mean); furthermore, they are quite different and it is difficult to give a unique value representative of the updraft rotation. To do so, we simply perform a weighted average of V^r_{rot} and V^l_{rot} obtaining a final estimation of the updraft rotation equal to $V_{rot} = 25 \pm 4$m/s. Of course, the uncertainty on this quantity can be even larger, considering the strong attenuation of the radar beam due to the presence of the FFD of the supercell on the path between the radar and the updraft.

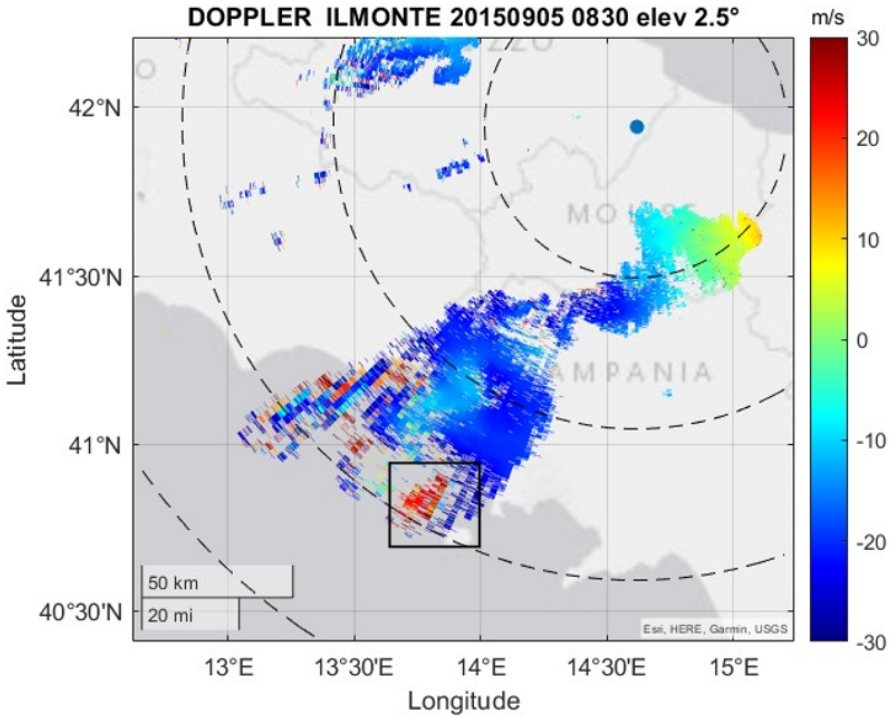

Figure 2.7: Doppler velocity measured from ground radar at 08:30 UTC and 2.5° of elevation in PPI mode. The black box identifies the region of analysis surrounding the mesocyclone, used for the estimation of the updraft rotation.

2.2.5 Vertical temperature profile

Up to now, only elements concerning the mere dynamics of the system have been considered. However, the thermodynamics is a crucial contribution for the development of a supercell storm, which is indeed driven by deep convection. Therefore, in this Section an analysis of the thermal stratification of the environment is performed.

The vertical temperature profile is obtained from the same pseudo-radiosounding computed from ERA5 data that was used for the ECAPE calculation, at the grid point [41°N, 13.25°E] (see Fig.2.8) The profile is very regular, and three regions can be identified: a nearly constant unstable lapse rate in the troposphere $\Gamma_{trop} = 7.0$ K/km (from the ground

to point A), a quasi-isothermal layer (from A to B) and the stable profile of the stratosphere (B-C). The tropopause (point A) is located at $\sim 12.7\,\mathrm{km}$. The value of Γ_{trop} is obtained through a linear interpolation of the observed temperature, from the ground to point A. The temperature gradient of the stratosphere is instead estimated simply from the data in points B and C, obtaining a value of $\Gamma_{strat} \sim 2.5\,\mathrm{K/km}$.

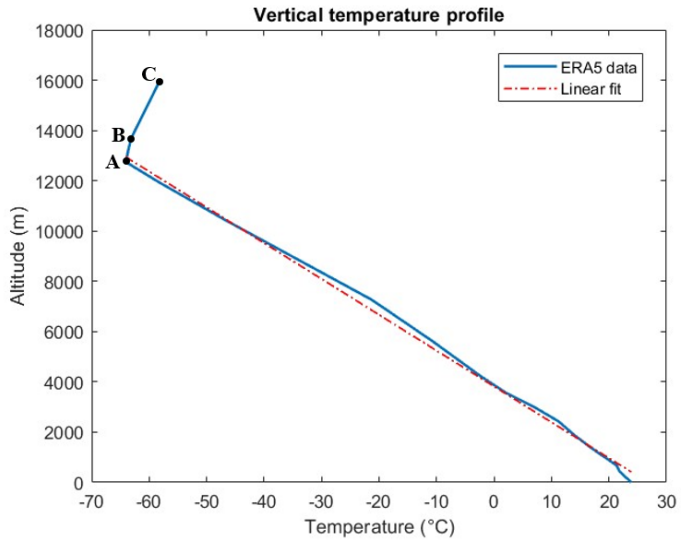

Figure 2.8: Vertical temperature profile at 08:00 UTC on ERA5 grid point [41°N, 13.25°E]. Dashed red line shows the linear fit representing the unstable lapse rate of the troposphere Γ_{trop}. Point A identifies the tropopause height ($z = 12700\,\mathrm{m}$), point B and point C are the ones used for the computation of the stable stratification of stratosphere Γ_{strat}.

The analysis of ECAPE in Section 2.2.1 allows also to give a useful estimation of the mean temperature difference T_{diff} between the environment and the updraft. The updraft vertical temperature profile can be only inferred from the saturated adiabatic lapse rate (red solid line in Fig.2.3), in absence of direct data. The saturated adiabatic lapse rate is the vertical profile that a saturated air parcel (as the ones in the updraft core) follows if it is lifted upward. We perform an average of T_{diff} along the vertical direction from the LFC to the EL, obtaining a single value $\overline{T_{diff}} = 4.7\,\mathrm{K}$. If multiplied by $\beta\, g$, where β is the thermal expansion coefficient of the air and g is gravity, then $\overline{T_{diff}}$ represents the mean *buoyancy force* per unit mass acting on the rising parcel during the ascent from the LFC.

In conclusion, the parameters estimated for the updraft and the crossflow in the CM reference frame of the supercell are summarised in the following Tab.2.3:

w_{max}(m/s)	D_u(km)	V_{wind}^{CM}(m/s)	V_{rot}(m/s)	Γ_{strat}(K/km)	Γ_{trop}(K/km)	$\overline{T_{diff}}$(K)
67	22 ± 3	12.0 ± 1.0	25 ± 4	2.5	7.0	4.7

Table 2.3: Summary of most relevant parameters of the updraft and crossflow estimated in this Section 2.2.

2.3 Vortices analysis

After the description of the fundamental physical and geometrical parameters characterising the updraft and its surrounding environment, the focus is now centered on the analysis of the shedding vortices observed in the Naples supercell, that are the main subject of this thesis. These vortices, which appear from ground radar reflectivity images, are shed downstream the updraft, that is located on the south/south-west region of the supercell as observed from Doppler data (Fig.2.7). Therefore, the updraft could have acted as an obstacle to the environmental wind, generating vortices in its wake. The vortices are visible as regions of enhanced reflectivity North-East the supercell FFD (the dark red spot in Fig.2.9, where heavy rain and hail are detected), suggesting that the vortices, once generated from the updraft, collect the hydrometeors from the FFD and drag them into the wake. This Section presents the estimation of the geometrical and structural parameters of the vortices, computed with reflectivity data from the ground radar in Monte il Monte, collected at time intervals of 5 minutes. The analysis is based on the data collected by Guidetti ([14], Fig.4.7), who performed the detection of the center of the vortices observed in reflectivity plots at 2.5° of elevation of the radar beam. According to these data, during the event six vortices are observed (three on the right and three on the left of the supercell core), and can be identified from reflectivity up to $\sim 80\,\text{km}$ downstream the supercell core. However, as explained previously, in this work we focus on the properties observed from 08:00 UTC and 09:00 UTC, when the system shows an almost stationary evolution on the sea. In this time window, the first three vortices and the beginning of the fourth are detected in the wake, which are considered enough to collect a sufficient statistics. We will refer to these vortices as Vortex 1, 2, 3, 4. Using these data, we are able to compute the fundamental parameters characterising the structure of the vortices:

- distance between vortices of the same sign ℓ (that is, shedding from the same flank of the system)
- distance of the vortices from the central axis of the wake h
- velocity of shedding vortices V
- period of shedding T

The computation of the distance between vortices of the same sign is obtained by simply applying the Pythagorean theorem to the longitude-latitude data. The distances are computed between Vortex 1 and Vortex 3, and between Vortex 2 and Vortex 4 for each frame in which they are visible, then an arithmetic mean of all the distances is computed. The result is finally converted to km with Eq.2.7, 2.6, reported in Tab.2.4.

The calculation of h is more tricky because the central axis of the wake is not stationary but moves together with the system. In order to give an estimation of the central axis direction at each instant of time, the centroid of the vortices is computed at each frame, as the mean of the (lon, lat) coordinates of the vortices visible at that specific frame. The central axis is then computed as the line passing through the pixel of maximum reflectivity and the computed centroid of the vortices. Then the distance h_i between the i^{th} vortex and the central axis is easily computed, obtaining a collection of h_i that are averaged together over all the different frames to get a final estimation of h (see Tab.2.4). The pixel of maximum reflectivity is preferred to the center-of-mass because it is considered a better estimation of the updraft position.

The velocity of the vortices is simply calculated as the mean of the values obtained by Guidetti ([14], Fig.4.10), applying the above mentioned correction due to the conversion

from pixel to km. Only the velocities of Vortex 1, 2 and 3 are considered, because Vortex 4 develops especially after 09:00 UTC. From the calculation of the average, the values of velocity $> 50\,\mathrm{m/s}$ are neglected because considered outliers and not realistic. The final result $V = 12.6 \pm 1.3\,\mathrm{m/s}$ (Tab.2.4) is very close to the previous estimation of V_{wind}^{CM}, and can be considered a validation of the goodness of this results.

Finally, once given the estimation of V and ℓ, the calculation of the period of shedding is trivial, and can be obtain simply as: $T = \ell/V$.

ℓ (km)	h (km)	V (m/s)	T (min)
33.0 ± 1.2	9.4 ± 0.6	12.6 ± 1.3	44 ± 5

Table 2.4: Vortices parameters estimated from ground radar reflectivity data.

The last remarkable feature related to the observed vortices is pointed out by looking at radar reflectivity plots, taken at the same instant of time at three different elevations in PPI mode (1.5°, 2.5°, 3.5°). The structure of the vortices is visible in all three elevations, without significant changes in their relative position (Fig.2.9, taken for a representative frame at 08:45 UTC). Given the distance of the vortices from the ground radar (100/150 km), for the effect of the Earth curvature the layer occupied by the vertical vortices goes from approximately 3 km altitude up to 10 km, which is almost the height of the supercell anvil (remind that the tropopause is located at 12.7 km). Unfortunately, no data are available at for smaller radar elevations. However, this observation suggests that the shedding vortices are advected in the wake, have a well-defined vertical development and occupy a column of atmosphere starting at the ground (or slightly above) and reaching the anvil near the tropopause.

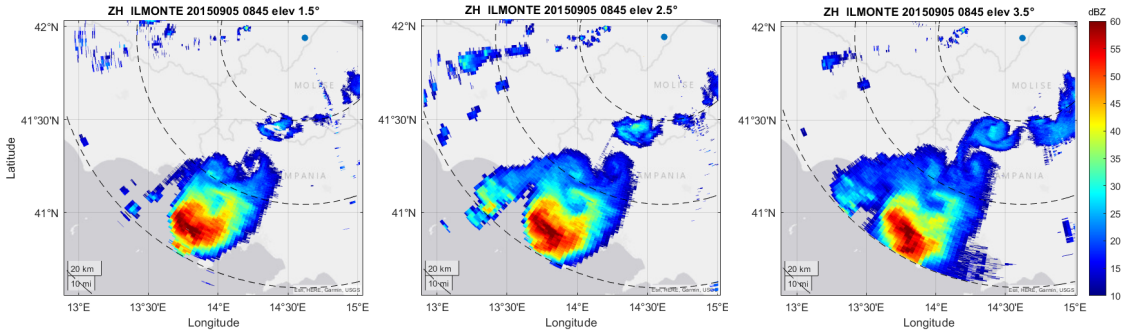

(a) (b) (c)

Figure 2.9: Reflectivity plot from ground radar data at 08:45 UTC at three different elevations in PPI mode (NB: at 3.5° the radar data reach only 150 km from the radar).

Chapter 3

Numerical simulation setup

This Chapter presents the description of the numerical approach, the model and the simulation setup adopted to investigate the formation of the wake vortices in the Naples supercell. As shown in Chapter 1, the progresses in the description of supercell storms have been remarkable, reaching very high resolutions in the last 10 years in Cloud Resolving Models. Following these steps, we would like to implement a high resolution simulation, able to capture the turbulent, unsteady motions at scales which are usually not reached by meteorological models. The vortex streets are in fact unsteady patterns, which would be filtered out by little computationally demanding approaches, like Reynolds Averaged Navier-Stokes (RANS) which employs a time-averaged form of the Navier-Stokes equations. Therefore, more sophisticated methods are needed, which are much more computationally expensive but crucial for our purposes.

The NS equations for a turbulent flow can be numerically solved by means of a Large-Eddy Simulation (LES), which is the approach we choose in this thesis work. Although the exact physical nature of turbulence has not been fully understood, it can be modelled to a sufficient degree of accuracy in numerical simulations ([58]). Turbulence is always three-dimensional and unsteady with a large range of motion scales that must be resolved and this has a high computational cost. The size of the computational domain must typically be at least an order of magnitude larger than the scales characterising the turbulent motions, while the computational mesh must be fine enough to resolve the smallest dynamically significant length-scale for accurate simulation. In this context Large-Eddy Simulation, typical of the field of Computational Fluid Dynamics, is a good compromise [58]. Furthermore, it is an innovative application, still little used in meteorology, of high resolution simulations to such large and complex phenomena like supercell storms, as explained in Chapter 1.

3.1 Kolmogorov theory of turbulence

Before describing the LES technique, it is worth introducing the theory of turbulence and the concept of energy cascade. Defining turbulence is a challenging task, but according to Lesieur [59] it has three main features:

- chaotic and three-dimensional
- ability to transport and mix fluid much more effectively than a comparable laminar flow
- the scales at which this mixing occurs include a wide range of spatial wave lengths.

The turbulent motions range in size from the dimension of the flow geometry to much finer scales, which become progressively smaller as the Reynolds number increases. Despite the high complexity of this phenomenon, the universally accepted turbulence theory is based on the study of Kolmogorov [2], whose main results are summarised in this Section. The Kolmogorov theory is based on the idea of the energy cascade, proposed by Richardson (1922). The idea is that the kinetic energy feeds the turbulence, trough the production mechanism, at the largest scales of motion. The energy is then transferred by inviscid processes to smaller scales until, at the smallest scales, viscosity dissipates the kinetic energy into thermal energy. Let us consider a turbulent flow with high Reynolds number, defined as $R_e = UL/\nu$, where ν is the kinematic viscosity term and v is the velocity on a length scale L. In Kolmogorov's view, turbulence can be considered to be composed of eddies of different size L; each eddy is characterized by a velocity $U(L)$, a timescale $\tau(L) = L/U(L)$ and a Reynolds number $R_e(L) = U(L)\,L/\nu$. The energy cascade continues until the $R_e(L)$ is sufficiently small and the viscosity is effective in dissipating kinetic energy. These eddies have energy of order U^2, so the rate of the transfer of energy can be supposed to scale as $U^2/\tau = U^3/L$.

Kolmogorov added to this scenario some hypothesis: the first hypothesis concerns the isotropy of the small-scale motions. In general, largest eddies are anisotropic and affected by the boundary conditions, but Kolmogorov supposed that these biases of the largest scales are lost in the chaotic cascade to smaller scales. Hence:

Kolmogorov's hypothesis of local isotropy: at high Reynolds numbers, the turbulent motions at small scales are statistically isotropic.

As the directional information, the geometry of the largest eddies is also lost. As a consequence, the statistics of the small scales is similar in every turbulent fluid with R_e enough large. Since in the energy cascade the dominant processes are the transfer of energy and the viscous dissipation, the parameters that govern the statistically universal state are the dissipation rate of energy ϵ and the kinematic viscosity ν. This leads to the second hypothesis:

Kolmogorov's first similarity hypothesis: in every turbulent flow at high Reynolds number, the statistics of the small scales have a self-similar form that is uniquely determined by ν and ϵ.

Defining ℓ_{EI} as the scale at which the information on the geometry and direction are lost, the size range $L < \ell_{EI}$ is referred to as the universal equilibrium range. Given the two parameters ϵ and ν, a unique length, velocity and time scale can be defined. These are called the Kolmogorov scales:

$$\eta = (\frac{\nu^3}{\epsilon})^{1/4} \qquad t_\eta = (\frac{\nu}{\epsilon})^{1/2} \qquad u_\eta = (\nu\epsilon)^{1/4} \tag{3.1}$$

Considering L_0, U_0 and τ_0, respectively, the size, the velocity and the dynamical time of the largest eddies, and the scaling $\epsilon \sim U_0^3/L_0$, we find, from Eq.3.1, the following result:

$$\frac{\eta}{L_0} \propto R_e^{-3/4} \qquad \frac{U_\eta}{U_0} \propto R_e^{-1/4} \qquad \frac{\tau_\eta}{\tau_0} \propto R_e^{-1/2} \tag{3.2}$$

Evidently, at high Reynolds number the smallest scales are even smaller compared with those of the largest eddies. As a consequence, at sufficiently high Reynolds number, there is a range of scales that are small compared to L_0, and bigger than η, i.e. $\eta << L << L_0$.

This range is called *inertial subrange*, and it is particularly important in LES because, as will be explained in the following Section, a good LES aims to resolve about the 80% of this interval. Since eddies in this range are much bigger than the dissipative eddies, it may be supposed that their Reynolds number is large and consequently that their motion is little affected by viscosity. Hence:

Kolmogorov's second similarity hypothesis: in every turbulent flow at high Reynolds number, the statistics of the motions in the inertial subrange have a self-similar form that is uniquely determined by ϵ, independent of ν.

Once the basic processes of the turbulence cascade are known, Kolmogorov theory provides the determination of the turbulent kinetic energy (TKE) distribution, which is particularly useful in the inertial subrange due to its importance in LES. The TKE is defined as follows:

$$\text{TKE} = \frac{1}{2}\sum_i \overline{u_i' u_i'} = \int_0^\infty E(k)\, dk \tag{3.3}$$

where the apex stands for the time fluctuation from the mean and the overbar indicates the time average. k is the wavenumber of the turbulent modes, $E(k)$ is the TKE power spectrum and represents the contribution to the turbulent kinetic energy from all the modes with $|k|$ in the range $k \leq |k| \leq k + dk$. Using a dimensional analysis and the three Kolmogorov's hypotesis presented before, the power spectrum $E(k)$ takes a simple form in the inertial subrange:

$$E(k) = C_k \epsilon^{2/3} k^{-5/3} \tag{3.4}$$

where $C_k \sim 1.5$ is the Kolmogorov constant. This relation shows that there is a wide range of scales in which the spectrum can be considered universal, and it is independent of the mechanism responsible of converting kinetic energy into heat through dissipation. In Fig.3.1 is plotted the Kolmogorov power spectrum, which clearly shows the separation between different ranges of the size of the eddies.

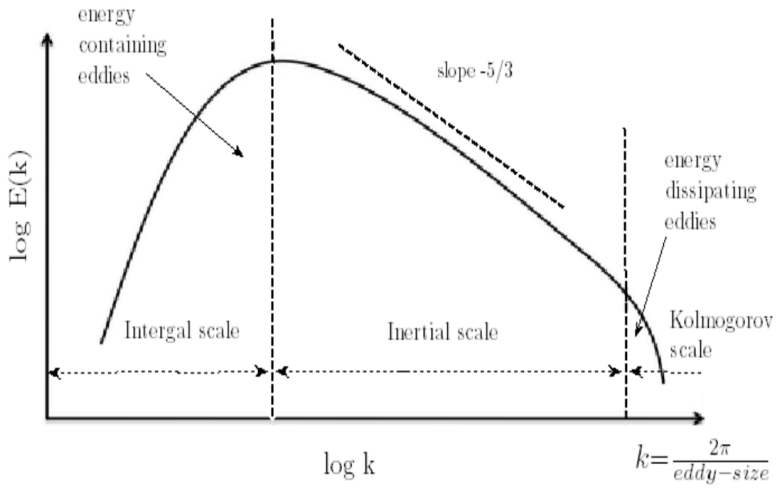

Figure 3.1: Scheme of turbulent kinetic energy spectrum.

At the smaller wavenumbers, the power spectrum $E(k) \propto k^2$ and turbulent kinetic energy production takes place (energy containing range); at medium scales (inertial subrange) the $-5/3$ slope from Eq.3.4 is visible; at the biggest k, turbulence is affected by viscosity which dissipates the kinetic energy generating an exponential cut off (energy dissipating range).

3.2 Large-Eddy Simulation approach

3.2.1 LES advantages

Mathematically speaking, turbulence arises from the nonlinear advection term inside Navier-Stokes equations (the complete governing equations for a fluid), so we can solve these motions only by applying numerical techniques. However, the presence of a wide range of scales down to a millimetric size as predicted by Kolmogorov, would require an extremely dense spatial grid for the numerical simulation and also a very short time step. This approach is effectively used and it is known as Direct Navier-Stokes (DNS): the full Navier–Stokes equations are numerically solved using very fine mesh to capture all the turbulent scales (Fig.3.2), therefore a DNS has a very elevated computational cost which makes it inapplicable to large domains and complex geometries.

On the other hand, in the Reynolds-Averaged Navier-Stokes simulation (RANS) a time average is applied to the variables and only the evolution of mean quantities is described. Thus the whole turbulent energy spectrum needs to be modelled through a turbulence model. The computational cost is in this case much smaller and for this reason RANS are widely applied in computational fluid dynamics for atmosphere and ocean on large domains. However, if the knowledge of the unsteady behaviour of the flow is necessary, the RANS approach is not sufficient to predict the flow behaviour. A partial solution is obtained with the so-called Unsteady RANS (URANS).

Between RANS and DNS, in the LES approach the large scale motions (large eddies) of turbulent flow are computed explicitly and only small scale (sub-grid scale, SGS) motions are modelled, resulting in a significant reduction in computational cost compared to DNS. LES is generally more accurate than the RANS and URANS approach since the large eddies contain most of the turbulent energy and are responsible for most of the momentum transfer and turbulent mixing. The LES captures large eddies directly in full detail, while they are modelled in the RANS approach.

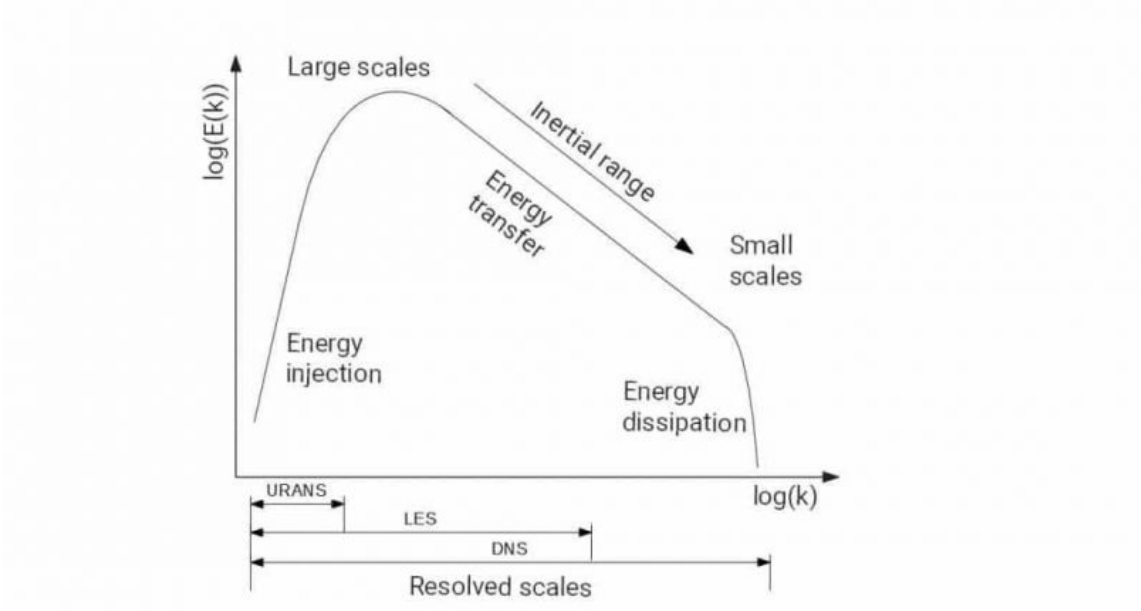

Figure 3.2: Comparison between the resolved scales in the TKE spectrum for URANS, LES and DNS.

Furthermore, the small scales tend to be more isotropic and homogeneous than the

large ones, and thus modelling the SGS motions is easier than modelling all scales within a single model as in the RANS approach. For all the reasons above, LES is a good compromise for simulating realistic turbolent flows. A reliable LES is such that it resolves the vortices responsible for at least 80% of the total turbulent energy, i.e., it cuts the spectrum in the inertial sub-range, near the dissipation region (see Fig.3.2).

3.2.2 LES equations

LES could be considered a 2-steps method:

1. the solution of the large scales of turbulence on a relatively coarse grid
2. the modelling of the smaller unresolved scales (sub-grid scales), based on the resolved velocity field

A generic variable ψ can be seen as the sum of a large scale component $\overline{\psi}$ and a small scale one ψ'. The separation of a turbulent motion into large scales to be resolved, and small scales to be modelled, derives from a spatial filtering operation that consists of a convolution of a kernel G_ℓ with the variable, function of the space and time, over a width ℓ. For a generic quantity ψ it is written (only in x direction) as:

$$\overline{\psi}(x,t) = \int \psi(\xi,t) G_\ell(x-\xi) d\xi \quad \Rightarrow \quad \psi = \overline{\psi} + \psi' \tag{3.5}$$

Typically, for LES the filter width ℓ is equal to the mesh width Δ, so that $\ell = \Delta = (\Delta_x \Delta_y \Delta_z)^{1/3}$. Many different choices are possible for the shape of the filter G_ℓ and the most common ones are the Gaussian filter and the so-called top-hat filter which assumes a constant value within the cell. Examples are shown in Fig.3.3

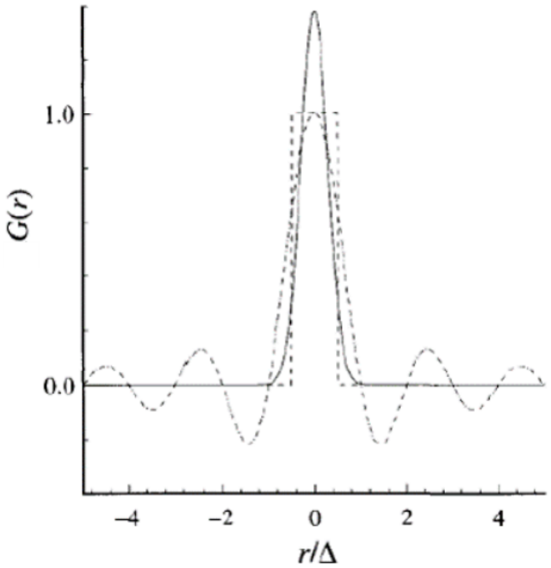

Figure 3.3: Examples of spatial filters for LES: dash, square line is the top-hat filter; continuous line is the Gaussian; the dashed, oscillating line is the top-hat in Fourier space. r is the spatial coordinate.

Applying this filtering operation to the velocity field u and pressure p in Navier-Stokes equations for momentum and continuity equation, gives the following result:

$$\begin{cases} \dfrac{\partial \overline{u_i}}{\partial x_i} = 0 \\ \\ \dfrac{\partial \overline{u}_i}{\partial t} + \overline{u_j}\dfrac{\partial \overline{u_i}}{\partial x_j} = -\dfrac{1}{\rho_0}\dfrac{\partial \overline{p}}{\partial x_i} + \nu\dfrac{\partial^2 \overline{u_i}}{\partial x_j \partial x_j} - \dfrac{\partial\left(\overline{u_i' u_j'} - \overline{u_i}\ \overline{u_j}\right)}{\partial x_j} \end{cases} \tag{3.6}$$

where $\overline{u_i' u_j'} - \overline{u_i}\ \overline{u_j} = \tau_{ij}^{SGS}$ is the sub-grid scale tensor that contains the contribution of unresolved scales and has to be modelled, because, as they are written, Eq.3.6 are not closed (more variables than equations). Respect to the complete Reynolds stress tensor τ_{ij}, τ_{ij}^{SGS} contains the contribution of small scale turbulence, which is characterized by isotropic, homogeneous, dissipative and geometry-independent eddies. The universality of those eddies is an advantage since it allows to define a general model without taking into account the geometry of each single problem. There are several ways to model sub-grid stresses, the first of which was proposed by Smagorinsky [3]. The Smagorinsky model is an Eddy-Viscosity model, because it relates the turbulence stresses to the mean flow shear by means of a turbulent viscosity parameter, which is parameterised to close the system of equations. In this model, the deviatoric part of τ_{ij}^{SGS} is expressed as:

$$\tau_{ij}^{SGS} - \frac{1}{3}\tau_{kk}^{SGS} = -2\nu_{SGS}\overline{S_{ij}} \tag{3.7}$$

where ν_{SGS} is a sub-grid scale viscosity that has to be parameterised and τ_{kk}^{SGS} is the sub-grid kinetic energy, also called k^{SGS}. This is performed applying a dimensional analysis using the the cell size of the computational mesh $\overline{\Delta}$ and the resolved strain-rate tensor $\overline{S_{ij}}$ that accounts for turbulent deformation:

$$\nu_{SGS} = c_s^2\,\overline{\Delta}^2\,|\overline{S_{ij}}| \qquad \text{with} \qquad S_{ij} = \frac{1}{2}\left(\frac{\partial u_i}{\partial x_j} + \frac{\partial u_j}{\partial x_i}\right) \tag{3.8}$$

where $c_s^2 = 0.4225$ is the Smagorisky constant. Due to the fact that ν_{SGS} is always positive and never goes to zero near the solid surface, it is also necessary to account for the almost laminar viscous sublayer where we should observe that $\nu_{SGS} \sim 0$. A classical and simple way to apply this correction is by using the van Driest function for near-wall damping of the dynamic viscosity [60].

Then, the budget equation for the resolved kinetic energy can be written, showing the impact in LES of sub-grid scales on the resolved scales:

$$\frac{\partial \overline{K}}{\partial t} + \overline{u}_j\frac{\partial \overline{K}}{\partial x_j} = -\nu\frac{\partial^2 \overline{u}_i}{\partial x_j^2} - \frac{\partial}{\partial x_i}\left(\overline{u}_i\overline{p} + \nu\frac{\partial \overline{K}}{\partial x_i} - \overline{u}_i\tau_{ij}\right) + \tau_{ij}^{SGS}\overline{S_{ij}} \tag{3.9}$$

On the left hand side there is the advection; the first term on right hand side term is the viscous dissipation, the second right term is the diffusion term and the third right term is the opposite of sub-grid scales dissipation and it is a negative term. Since LES by definition are carried out for large scales and grid scales is larger than the Kolmogorov one, the viscous dissipation is negligible compared to the others terms; diffusion term represents only a transfer of energy in space, but not properly between scales. Therefore an additional term is required in order to reproduce the correct energy transfer from the large to the smaller scales. Sub-grids scales dissipation covers that role (last term on the

right). Therefore, for completeness, we report also the budget of sub-grid kinetic energy $\tau_{kk}^{SGS} = k^{SGS}$:

$$\frac{\partial k^{SGS}}{\partial t} + \overline{u}_j \frac{\partial k^{SGS}}{\partial x_j} = -\frac{\partial}{\partial t}(\overline{u_i u_i u_j} - \overline{u_i u_i}\ \overline{u}_j) - 2\frac{\partial}{\partial x_j}(\overline{p\, u_j} - \overline{u}_j \overline{p}) + \frac{\partial}{\partial x_j}\left(\nu \frac{\partial k_{SGS}}{\partial x_j}\right) + \\ + 2\frac{\partial}{\partial x_j}(\tau_{ij}\overline{u}_i) - 2\nu\left(\overline{\frac{\partial u_i}{\partial x_j}\frac{\partial u_i}{\partial x_j}} - \overline{\frac{\partial u_i}{\partial x_j}}\ \overline{\frac{\partial u_i}{\partial x_j}}\right) - 2\tau_{ij}^{SGS}\overline{S_{ij}} \tag{3.10}$$

All energy redistribution terms appear except the last two, of which: the first is the viscous dissipation which represents a net energy loss due to viscosity and the second is the sub-grid scales dissipation which represents the energy exchange between resolved and unresolved scales mentioned above. To be noted, in fact, that this last term appears with opposite signs in Eq.3.9 and Eq.3.10, indicating that the energy that is subtracted from the larger vortices becomes available energy at the sub-grid scales. This is coherent with the energy cascade explained by the Kolmogorov theory in Section 3.1

Now the problem is closed and it is possible to setup the numerical simulation.

3.3 Physical assumptions and mathematical model

As explained in Chapter 2, the Naples hailstorm was a very complex event influenced by a numbers of factors. First,it was dominated by convection due to the intrusion of cold air over the warmer Mediterranean sea, as shown in Marra et al. [10] and Guidetti [14]. This intrusion introduced a temperature gradient that, together with the presence of vertical wind shear, contributed to the formation of a thunderstorm convective cell, with the development of a strong updraft. All these factors concurred to the growth of a cumulonimbus with a complex micro-physical structure, characterized by the phase transition of water and the formation of big ice particles, present at high altitudes.

Due to the complexity of the observed event, the setup of a simulation requires some simplifications. Furthermore, this approach is also driven by a methodological reason: the reduction of the system to its essential components also allows to isolate the contribution of each of them, which is important in order to investigate the origin of such an unusual phenomenon like the observed vortex street. For the purpose of the simulation, only some of the above factors will be considered to replicate the storm:

Fundamental terms:

- strong updraft development
- constant environmental crossflow
- stable stratification of stratosphere
- updraft temperature
- updraft rotation
- non-hydrostatic model

Neglected terms and approximations:

- Coriolis force
- vertical wind shear
- water vapor and latent heat
- cloud microphysics and precipitations
- boundary layer and topography
- incompressible fluid
- Boussinesq approximation
- unstable stratification of troposhpere

The decision of what contributions to be neglected, is determined not only by the importance of these effects in the formation of supercell storms, but also by numerical stability reasons (as it is for the unstable stratification, which is critical to manage numerically) and by the availability of data to initialize the simulation. Water vapor and vertical wind shear, which are also crucial for the development of supercells, are not implemented in this thesis due to the larger uncertainty on data and the complexity of these contributions.

Furthermore, as it will be explained also later in this work (see Section 3.6, 3.7), in order to investigate the separate effects of the crossflow, the thermal stratification (buoyancy) and updraft rotation, these contributions are added in different stages in the numerical model. Precisely, the first simulations do not consider thermodynamics and updraft rotation, which are included only in the final simulations.

Given this necessary information, the governing equations of the model are presented in Eq.3.11, written as they are used for the final simulations where all the fundamental contributions are included. The thermal stratification of the environment is described by the decomposition into a background θ_B and a perturbation T contribution (see Prandtl [61]): $\theta = \theta_B + T$. Assuming that the background temperature is a linear function of the height z (which is actually our case in both the stratosphere and troposphere) and β is the thermal expansion coefficient, one can define the square of the Brunt–Väisälä frequency $N^2 = \beta\, d\theta_B/dz$ as a constant. In this framework, the governing equations are written as in Eq.3.11, which are the continuity equation for an incompressible fluid, momentum equation and temperature equation. The fourth equation is solved *only* in the first simulations where temperature is absent: it describes the evolution of a passive scalar c, which simply helps to the visualization of the developing updraft into the crossflow and does not have any impact on the dynamics. Once temperature (which is instead an active scalar) is added, there is no need to use the equation for c anymore, so it will be neglected.

$$\begin{cases} \dfrac{\partial u_i}{\partial x_i} = 0 \\ \dfrac{\partial u_i}{\partial t} + u_j \dfrac{\partial u_i}{\partial x_j} = -\dfrac{\partial p^*}{\partial x_i} + \nu \dfrac{\partial^2 u_i}{\partial x_j \partial x_j} - g_i \beta T \\ \dfrac{\partial T}{\partial t} + u_i \dfrac{\partial T}{\partial x_i} = -\dfrac{N^2}{\beta g} u_i g_i + \alpha \dfrac{\partial^2 T}{\partial x_i \partial x_i} \\ \dfrac{\partial c}{\partial t} + u_i \dfrac{\partial c}{\partial x_i} = \alpha \dfrac{\partial^2 c}{\partial x_i \partial x_i} \end{cases} \tag{3.11}$$

where u_i are the velocity components, $p^* = (p - \rho g_i x_i)/\rho_0$ is the pressure deviation from the kinematic hydrostatic pressure, ρ_0 is the constant reference density, g_i is the gravity acceleration vector and $g = 9.81\,\mathrm{m/s^2}$ is its modulus, ν is the kinematic viscosity and α is the molecular thermal diffusivity. In absence of thermal stratification $\theta_B = \text{const.}$ and $N^2 = 0$.

When numerically solved in our model, temperature equation is multiplied by a factor βg, so that the variable of the equation becomes directly the *buoyancy* $b = g_i \beta T$, without changing anything in the physics of the system.

3.4 Non-dimensional numbers and parameters

The use of dimensionless numbers is ubiquitous in Computational Fluid Dynamics, because they allow to simplify equations, compare different systems, and predict the behavior of fluid flows. Systems with different values of the fields but the same dimensionless numbers are dynamically equivalent. Computationally, dimensionless numbers have the added benefit of providing numerical scaling of the system discrete equations. This is advantageous from a numerical point of view, because scaling the quantities can influence the rate of convergence, and proper scaling can lead to faster convergence: scaling the variables to obtain manageable values of the fields (not too large, not too small) is often a good practice. Furthermore, non-dimensional scaling provides a method for developing dimensionless groups that can give physical insight into the importance of various terms in the system of governing equations.

In this study, the relevant dimensionless numbers are:

- Reynolds number, which is the ratio of inertial forces to viscous forces:

$$R_e = \frac{V_{cf} D_u}{\nu} \tag{3.12}$$

  where V_{cf} is the cross-flow velocity, D_u the updraft diameter and ν the kinematic viscosity.

- velocity ratio, which represents the relative strength of the jet to the cross stream:

$$\kappa = \frac{V_u}{V_{cf}} \tag{3.13}$$

  where V_u is the updraft velocity.

- Strouhal number, useful to describe oscillating flow mechanisms, especially von Karman vortex streets:

$$S_t = \frac{f D_u}{V_{cf}} \tag{3.14}$$

  where f is the frequency of vortex shedding, D_u is the updraft diameter (in general, it is the characteristic dimension of the obstacle) and V_{cf} is the crossflow velocity.

- Prandtl number, which is the ratio between momentum diffusivity and thermal diffusivity

$$P_r = \frac{\nu}{\alpha} \tag{3.15}$$

  where ν is the kinematic viscosity and α the molecular thermal diffusivity.

- Froude number, which is the ratio of the crossflow inertia to the plume motion:

$$F = \frac{V_u}{\sqrt{\beta(T_u - T_{cf}) g D_u}} = \frac{V_u}{V_b} \tag{3.16}$$

  where V_u is the updraft velocity, β is the thermal expansion coefficient, T_u is the updraft temperature, T_{cf} is the crossflow temperature, g is gravity.

3.5 Algorithm and numerical schemes

The numerical simulation is performed with the open-source software OpenFOAM version 9. Open Source Field Operation and Manipulation (OpenFOAM) is a software for computational fluid dynamics (CFD), written in C++. It includes a collection of applications which perform a range of tasks in CFD. As well as performing calculations of the fluid dynamics, there are applications which configure and initialise simulations, manipulate case geometry, generate computational meshes, and process and visualise results (see OpenFOAM9 user guide [62]). OpenFOAM is shipped with a version of ParaView, an open source post-processing visualization engine, that includes a reader module to read data in OpenFOAM format. This enables visualization of solutions from OpenFOAM, with elements used commonly in CFD such as geometry surfaces, cutting planes, vector plots and streamlines.

The basic solver `buoyantBoussinesqPimpleFoam` has been customised to perform the LES, as in [41] (note that in [41] the buoyancy force was driven by salinity, not temperature as in this case). Conversely to [41], the sub-grid scale model is the classical Smagorinsky model [3] described in Section 3.2.2. The passive scalar equation has also been added manually to the solver. The resolution algorithm is PISO (Pressure implicit with splitting of operator) developed for the computation of unsteady flows, see Oliveira and Issa [63].

The governing equations are discretised in time using an implicit Euler backward scheme (that uses the variables at the previous two time steps, resulting in second order accuracy); in space (except for the advection terms in momentum, temperature and tracer equations) using a `Gauss linear` scheme, that is a second-order central difference scheme. The `Gauss` entry specifies the standard finite volume discretisation of Gaussian integration which requires the interpolation of values from cell centres to face centres. The interpolation scheme is then given by the `linear` entry, meaning linear interpolation or central differencing [62]. The discretisation of advective terms is a critical issue in LES, since they can lead to numerical instabilities in the region where the updraft acts as an obstacle for the crossflow and sharp interface develops. The temperature advection term and the tracer advection are discretised with the MUSCL scheme by van Leer [64] as it is implemented in OpenFOAM (`Gauss MUSCL`). It is a total variation diminishing (TVD) scheme of second-order accuracy, commonly used to solve hyperbolic partial differential equations. A TVD scheme is said to be monotonicity preserving because the following properties are maintained as a function of time:

- no new local extrema can be created within the solution spatial domain
- the value of a local minimum is non-decreasing, and the value of a local maximum is non-increasing

For momentum advection we used instead the `Gauss Gamma` scheme proposed by Jasak et al. [65] with $\gamma = 0.2$, which is a bounded version of central differencing. The time step is dynamically computed to satisfy the Courant–Friedrichs–Lewy condition $\mathrm{CFL} = U\Delta t/\Delta x < 0.5$, which ensures the stability and accuracy of the simulation ([66]).

The simulations are run on OPH cluster at Physics and Astronomy Department (DIFA), a parallel computing infrastructure directly accessible to its members. This infrastructure is made up of three different groups (or islands) of computing nodes with different hardware features and target usage. In particular the “Matrix” island is a set of nodes targeted to massively parallel jobs. The simulations are run in parallel on a high number of processors (56/112/168 depending on the simulation computational cost and

availability of computing nodes), and take many days to complete, almost two weeks for the most demanding ones.

3.6 Case geometry and computational mesh

The simplification of the real system involves also the geometry of the case in the numerical simulation. We try to set up a simplified mesh geometry starting from a classical CFD problem which has similarities with the one we are dealing with. Firstly, we set up the simulation in the supercell center-of-mass reference frame: due to the natural movement of the supercell, this choice avoids the escape of the system from the computational domain during the simulation. Then, the problem is reduced to a classical Jet In CrossFlow (JICF): the vertical jet simulates the updraft while the crossflow is the environmental wind. Buoyancy and rotation are added later to the JICF, to increase gradually the complexity of the simulated system. When buoyancy is added, we refer as bouyant JICF (BJICF). This configuration, despite its largely simplified geometry, can be very insightful and helps us to understand if the updraft could have behaved similarly to a solid obstacle for the tropospheric wind, to generate the shedding vortices in the wake. The vertical jet exits from a cylindrical nozzle of diameter D, placed at the bottom surface. The presence of the nozzle of finite height (see Cintolesi et al. [41]) is due to numerical stability reasons, because if the jet started directly from the ground, the computational cells at the border of the jet exit would likely generate numerical instabilities (velocity field start growing abruptly).

3.6.1 *Coarse Mesh*

The first simulation we perform will be addressed as *Coarse Mesh* hereafter. In this simulation the nozzle has diameter and height D, which is set equal to 20 km as will be explained in the following Section 3.7 concerning the initial conditions. The nozzle central-point is located in the centre-line with respect to the y-direction, at a distance $4D$ from the crossflow inlet (Fig.3.4). The domain is a parallelepiped, whose dimensions are large enough in order to contain the jet and allow the flow to become laminar at the boundaries, to avoid unwanted border effects in the simulation. The dimensions of the parallelepiped are: $(x,y,z)=(120D,\ 40D,\ 70D)$, see Fig.3.4a, Fig.3.4b. Then, we use a fine mesh around the jet exit (cells size $0.2D$ or smaller) and a coarser mesh elsewhere (cell size around $0.5D$). This choice is reasonable since the turbulent structures are smaller above the nozzle (when jet velocity magnitude is high) while they become larger when the plume penetrates the crossflow. The background mesh is composed by a uniform grid that discretises the computational domain in $200 \times 66 \times 116$ points in the x, y, z directions (respectively). The mesh is refined (width of cells is divided by a factor 2 in each direction at each level of refinement) in a zone around the nozzle, consisting of a box of dimensions $28D$, $6D$, $30D$, where the refinement is 6 km. Such a box has one face on the bottom of the computational domain, is centred with respect to the y-direction, and is placed at a distance of $x/D = 2$ from the inflow boundary (the yz-plane at $x = 0$). A thin region around the cylinder is additionally refined for better capturing the nozzle shape. The *Coarse Mesh* has ~ 2 million cells.

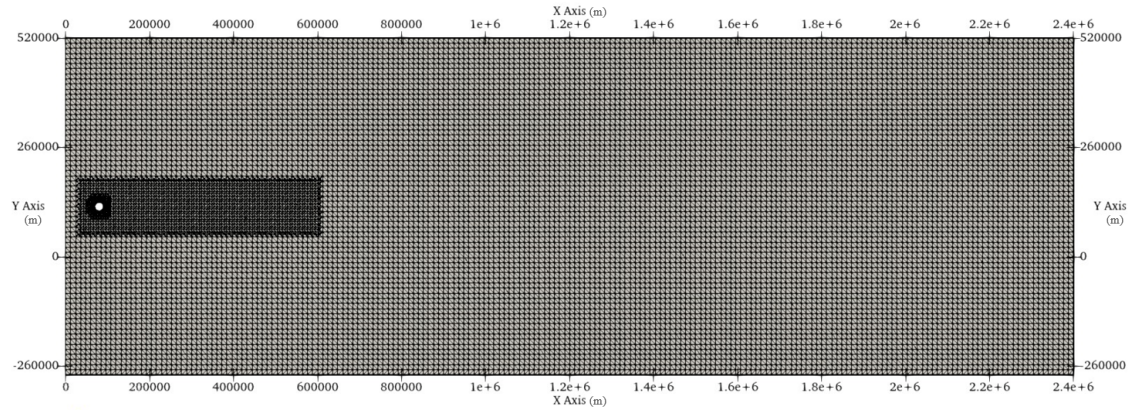

(a)

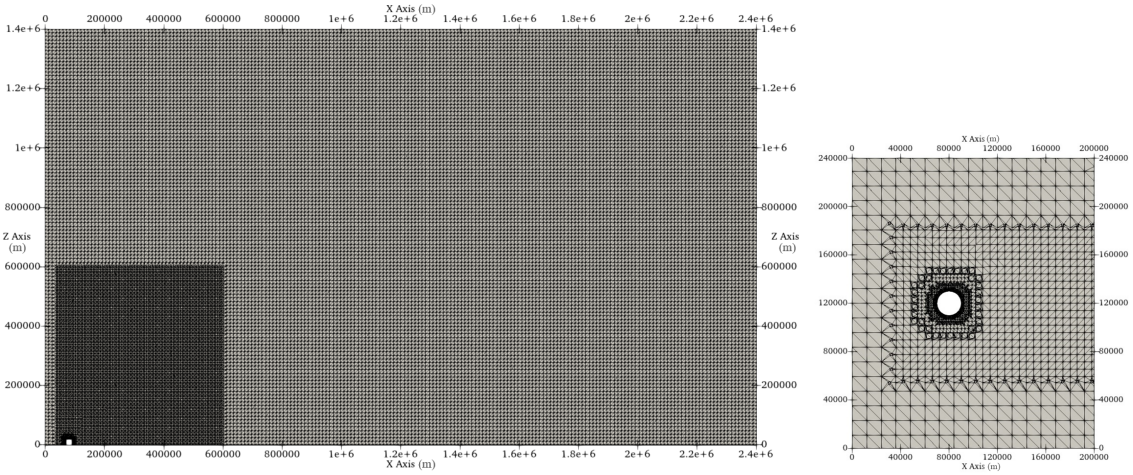

(b) (c)

Figure 3.4: Fig.3.4a: horizontal view of the *Coarse Mesh*, the white dot on the left is the cylindrical nozzle. The darker region is the refinement box where the cells are finer. Fig.3.4b: same as Fig.3.4a but on a vertical plane passing across the cylindrical nozzle. Fig.3.4c: focus on the nozzle region on a horizontal plane. The nozzle is the white circle, around it the different levels of refinement.

3.6.2 Refined meshes

Since the refinement region of *Coarse Mesh* which resolves the first part of the jet and its wake has 6 km resolution (which is very coarse), we perform a mesh refinement. This is done by creating four different meshes, with different resolution or extension of the refinement region, using the `snappyHexMesh` tool of OpenFOAM 9. Firstly, we apply a domain reduction in order to both save some cells necessary for the refinement and focus on a smaller portion of the system. This procedure is done by looking at the dimensions of the simulated jet in the *Coarse Mesh*, the exact procedure is reported in Section 4.2 with the analysis of the results. We finally obtain the following mesh dimensions, equal for all the four meshes generated: (x,y,z)=$(80D,\ 24D,\ 34D)$. The background mesh has resolution of 8 km, therefore the cells in the three directions are $200 \times 60 \times 85$. The position of the nozzle is not changed, but its height is decreased to 1 km in all simulations, to diminish its impact on the crossflow, and the value $D = 20$ km is kept fixed. All the simulations have a very thin refinement layer at 125 m resolution around the solid nozzle in order to capture better its shape. Given these common features, the four computational grids are:

- *Mesh_1*: first refinement box at 1 km resolution of dimensions $10D$, $4D$, $3D$ in the three spatial directions, is placed at a distance of $x/D = 2.5$ from the inflow face. Second refinement box at 500 m resolution of dimensions $5D$, $2.5D$, $1D$ in the three spatial directions, is placed at a distance of $x/D = 3$ from the inflow face. Both these boxes have one face on the bottom of the computational domain and are centred with respect to the y-direction.

- *Mesh_2*: only one refinement box at 500 m resolution of dimensions $7.5D$, $3D$, $2D$ in the three spatial directions, is placed at a distance of $x/D = 3$ from the inflow face. It has one face on the bottom of the computational domain and is centred with respect to the y-direction.

- *Mesh_3*: first and second refinement boxes at 1 km and 500 m resolution equal to *Mesh_1*. Third refinement box at 250 m resolution of dimensions $1.5D$, $1.5D$, $4/5\,D$ in the three spatial directions, is placed at a distance of $x/D = 3.5D$ from the inflow face. These measures of the 250 m resolution box are chosen ad hoc to contain the updraft only, from the ground to the maximum height observed from satellite measurement in the real case (~ 16 km).

- *Mesh_4*: first refinement box at 1 km resolution equal to *Mesh_1*. Second refinement box at 250 m resolution of dimensions $5D$, $2.5D$, $4/5\,D$ in the three spatial directions, is placed at a distance of $x/D = 3.5D$ from the inflow face. This simulation is the one with more computational cells (~ 6.3 millions).

In all these meshes, the refinement boxes at 250 m or 500 m are designed to capture all the wake where the vortices are observed in the real case (up to ~ 80 km downstream the updraft). A final simulation identical to *Mesh_4* but with the nozzle 20 km high (as it was in *Coarse Mesh*) is performed in order to check more accurately the effect of the solid cylinder on the wake. We refer to this last simulation as *High Cylinder*.

3.6.3 Final meshes

Finally, once performed the mesh assessment analysis (Section 4.2) that shows the better performance of *Mesh_4* compared to the others, the final simulations are set up. The mesh employed now is based on *Mesh_4*, but with some further changes. In fact, in these final simulations also the thermal stratification and rotation are implemented, that were not included in the previous cases. The stable stratification of stratosphere limits almost all the system to the first 15/25 km of atmosphere, therefore some changes in the mesh are applied in order to focus on this layer:

- the height of the 250 m refinement box is increased from $4/5\,D = 16$ km to 25 km, and the width from $2.5\,D = 50$ km to 70 km.

- the height of the 1 km refinement box is reduced from $3D = 60$ km to 40 km. This box cannot be completely removed, because it is important to guarantee a sufficiently smooth transition to the coarse background mesh.

- the dimension of the domain is reduced to (x,y,z)=$(30D,16D,8D)$=(600,320,160)km.

This mesh is referred as *EnhancedMesh_4*. The x and y dimensions of the domain are imposed similarily to Parello [67] for the case of the JICF. The velocity profile at the outlet is checked in order to see if the velocity field adjusts approximately to the unperturbed crossflow velocity, especially at the lateral borders: this is important to avoid numerical

instabilities that appear if the flow is still turbulent when approaching the boundaries. A sensitivity analysis is also performed using *EnhancedMesh_4*, by varying the the nozzle diameter with three values of D: 15 km, 20 km, 29 km. To allow the comparison between these three cases, the *EnhancedMesh_4* has not been scaled depending on D, but has been kept always fixed to the dimensions presented above. *EnhancedMesh_4* has $\sim$ 13.2 millions of computational cells. A view of *EnhancedMesh_4* on the horizontal and vertical planes is given in Fig.3.5, where are visible also the buffer layers between the three levels of refinement. The dark rectangles refer to the 250 m refinement region, which is too fine to be visualised.

Finally, one more mesh is created with exactly the same geometry of *EnhancedMesh_4*, but the refinement region at 200 m resolution instead of 250 m. Since the levels of refinement in `snappyHexMesh` scale as a power of 2, also the 1 km-resolution box becomes 800 m-resolution, and the 8 km-resolution background becomes 6.4 km-resolution. This mesh has $\sim$ 26.3 millions computational cells, and therefore it is used for one simulation only with $D = 29$ km due to its extremely high computational cost, to observe the possible effects of an increase in resolution of the 20%. We will refer to this mesh as *maxResMesh*.

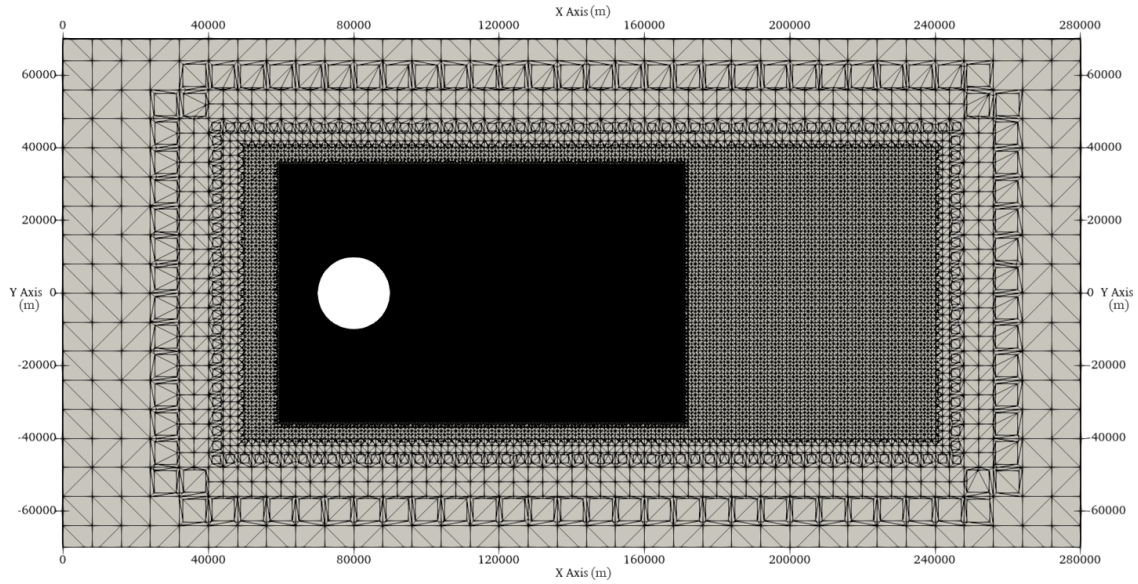

(a)

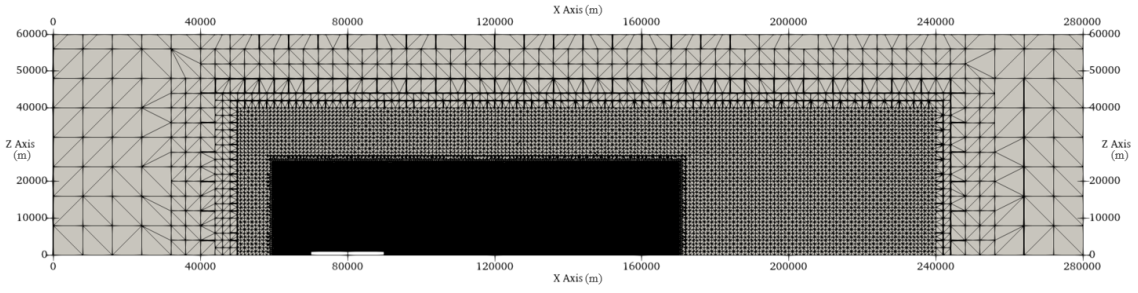

(b)

Figure 3.5: Fig.3.5a: horizontal view of the refined region of *EnhancedMesh_4*, in white the cylindric nozzle. Fig.3.5b: vertical view of the refined region of *EnhancedMesh_4*, in white, at the bottom, the cylindric nozzle.

To sum up, the following meshes are used in this thesis work: *Coarse Mesh*, *Mesh_1*, *Mesh_2*, *Mesh_3*, *Mesh_4*, *High Cylinder*, *EnhancedMesh_4* (same for three values of

$D = 15, 20, 29\,\text{km}$), *MaxResMesh*.

In all these simulations, the evolution of the flow can be controlled run time looking at the data from some probes located on specific points in the domain. This is a tool provided by OpenFOAM. The probes location is the same for all the different meshes, and focuses on the vertical jet and on its wake. In agreement with the real case, the probes taken as reference lie on a horizontal plane at $z = 7\,\text{km}$, which is in the middle of the vertical layer where the vortices are observed in the real case (see Section 2.3). These probes are shown in Fig.3.6. When necessary, during the analysis other probes are selected at different heights, but always on the same horizontal coordinates of the ones in Fig.3.6.

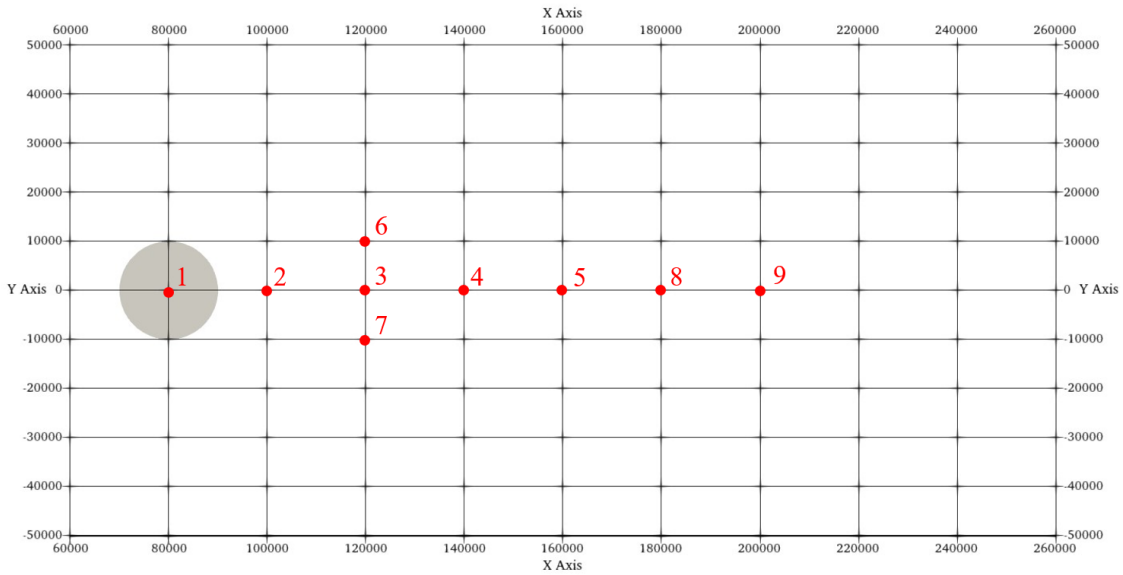

Figure 3.6: Probes location on the horizontal plane at 7 km height above the ground.

3.7 Initial and boundary conditions

In this Section we list the initial conditions imposed for all the different simulations performed, using the estimations given in Chapter 2. Considering the values in Tab.2.3 and Eq.3.12, 3.13 with $V_{cf} = V_{wind}^{CM}$, $V_u = w_{max}$ and $D_u = D$, the Reynolds number in the real case is equal to $R_e = 1.78 \cdot 10^{10}$ and the velocity ratio is $\kappa = 5.6$. Since the values of the observed quantities are still reasonably small, $O(10)$, the numerical scaling is not really necessary in this work. Therefore, the simulations are run with the non-scaled quantities.

As we explained in Section 3.3, different simulations are performed, starting from the case of a simple JICF and adding gradually the contributions of buoyancy and rotation. For the buoyancy-free and rotation-free simulations, the the system is actually a classical JICF and requires the imposition of the vertical jet velocity V_u (simulating the updraft), the crossflow velocity V_{cf} and the vertical jet diameter D, which is the diameter of the cylinder at the bottom. The values are listed in Tab.3.1. V_{cf} and D are coherent with the estimations from the real case in Tab.2.3. Since we neglect vertical wind shear, the value of the crossflow is the same at all altitudes. V_u, instead, is different from the estimation of w_{max}. This choice is due to the fact that w_{max} refers to the maximum updraft speed, which is usually observed in the upper levels of the cloud and is not representative of the entire updraft section. In fact, usually the maximum velocity occurs in a fairly uniform region in the middle of the updraft, and then it decreases almost radially. Thus, imposing an upward velocity of $w_{max} = 67\,\text{m}\,\text{s}^{-1}$ on the entire nozzle exit seems to be not realistic. So, finally

we choose as initial vertical velocity of the jet a smaller value equal to $V_u = 40\,\mathrm{m\,s^{-1}}$, that we judge more appropriate for low level upward speed in a supercell storm with similar updraft peak velocity [13]. A constant value of the passive scalar $c = 10$ is also imposed at the nozzle exit.

V_u (m/s)	D (km)	V_{cf} (m/s)	c	ν (m^2/s)	R_e	κ
40	20	12	10	$1.48 \cdot 10^{-5}$	$1.62 \cdot 10^{10}$	3.3

Table 3.1: Initial conditions for all the simulations with no buoyancy.

When buoyancy is added, the thermal stratification of the environment and the updraft temperature are needed to initialise the simulation. The unstable stratification of the troposphere is not considered in the simulation, because its presence causes the generation of ubiquitous convective cells all over the numerical domain and affects the quality of the simulation. In order to deal with this approximation, an alternative approach is used to reproduce the buoyancy force in the troposhpere, taking advantage from the fact that the variable in the temperature equation in Eq.3.11 is not the absolute temperature, but the temperature difference from the background flow. Therefore, we keep the stable stratification of the stratosphere equal to the observed one, with gradient $\Gamma_{strat} = 2.5\,\mathrm{K/km}$ for $z \geq 12700\,\mathrm{m}$, resulting in $N^2 = \beta\,\Gamma_{strat}$. On the other hand, we impose a *neutral* stratification ($N^2 = 0$) in the troposphere and a positive value of the buoyancy directly at the exit of the nozzle. This value (we call it b_u) must be chosen properly in order to reproduce the vertical acceleration caused by the unstable stratification over the whole troposphere: it is chosen as the mean deviation of the moist adiabatic temperature profile from the vertical environmental temperature profile, computed in Section 2.2.5 as $\overline{T_{diff}}$. Finally, since in our model we solve directly the equation for the buoyancy b (which is equal to the equation for T but multiplied by βg), we impose at the exit of the nozzle $b_u = \beta g \overline{T_{diff}} \sim 0.1913\,\mathrm{m/s^2}$. We point out here that the value of β varies with temperature. To take into account this effect, we use the tabulated values in [68]: at the jet exit, we use $\beta = 4.15 \cdot 10^{-3}\,\mathrm{K^{-1}}$, which is approximately the mean of β computed over the whole troposphere, given that the observed sea surface temperature is $T_{SST} \sim 26°\mathrm{C}$ and the temperature at the tropopause from ERA5 data is $T_{trop} \sim -65°\mathrm{C}$. For the computation of N^2 in the stratosphere, instead, we use $\beta = 4.9 \cdot 10^{-3}\,\mathrm{K^{-1}}$, which is approximately the value extrapolated for $T_{trop} \sim -65°\mathrm{C}$.

Furthermore, the implementation of buoyancy requires a change in the value of the vertical velocity to impose at the nozzle exit: if we kept $V_u = 40\,\mathrm{m/s}$, the accelerating buoyant effect in the troposphere would cause an extremely strong, unrealistic updraft ($\sim 100\,\mathrm{m/s}$). Therefore, we impose a suitable vertical velocity after running some short trial simulations, in order to see what value of V_u allows to reproduce a maximum vertical velocity similar to w_{max} in Section 2.2.1. This gives a final estimation of $V_u = 10m/s$.

Concerning rotation, in absence of vertical wind shear in our simulation, there is no hope for the simulation to develop spontaneously updraft rotation (Chapter 1). Therefore, rotation is imposed directly at the jet exit as a constant angular velocity $\omega_R = 2V_{rot}/D$, so that the tangential velocity reaches the maximum value of $V_{rot} = 25\,\mathrm{m/s}$ on the border of the nozzle, as in Tab.2.3.

In Tab.3.2 the initial conditions for the simulations with buoyancy and rotation. As explained in the previous Section 3.6, the value of D is changed to perform a sensitivity analysis, and consequently also ω_R varies. The other quantities are kept always fixed.

V_u (m/s)	D (km)	V_{cf} (m/s)	b_u (m/s^2)	Γ_{strat} (K/km)	ω_R (s^{-1})
10	15	12	0.1913	2.5	0.0033
10	20	12	0.1913	2.5	0.0025
10	29	12	0.1913	2.5	0.0017

Table 3.2: Initial conditions for all the simulations with buoyancy and rotation, for the three values of D imposed. Γ_{strat} is imposed from $z = 12700$ upward, which is the estimated tropopause height.

The boundary conditions are: inlet, constant velocity V_{cf} in x-direction and buoyancy (if present) $b = 0$; lateral and top boundaries, constant velocity V_{cf} in x-direction and zero-gradient for buoyancy. Bottom boundary is considered a solid surface, hence no-slip condition for velocity and zero-gradient for temperature are applied; the nozzle surface is a solid surface, too, but in order to minimize its contribution (which of course it is not present in the real atmosphere), we use a free-slip condition on velocity (i.e. no viscous boundary layer is present, the fluid flows freely on the surface) and zero-gradient for temperature. At nozzle exit, constant velocity V_u in z-direction; buoyancy b_u and rotation ω_R if present. Outlet, zero-gradient for velocity and buoyancy. Pressure is fixed at $p = 0$ at the outlet, while the zero-gradient condition is set elsewhere. The Van Driest wall-function [60] is applied near the bottom boundary to correctly damp the ν_{SGS} within the wall boundary layer.

All the simulations performed are run for a period of time established depending on the *characteristic time* t_c of the system, that is defined as the time that takes the crossflow to travel the whole length of the domain in streamwise direction, L_x from the inlet to the outlet:

$$t_c = \frac{L_x}{V_{cf}} \tag{3.17}$$

Typically, we set the execution time of the simulation to t_c equal to 2 or 3, in order to allow the flow to exceed the initial transient period and likely reach a statistical steady state.

Chapter 4

Methodological approach

The present work, in some aspects, represents a new research, both for the singular vortex pattern and for the CFD approach adopted in a meteorological deep convection event. In the present Chapter, a working methodology to approach the problem is suggested, starting from the qualitative results obtained with the *Coarse Mesh*, then describing the mesh refinement and finally adding the higher levels of complexity in the physics of the system.

4.1 *Coarse Mesh* analysis

The first step of the procedure provides for the use of the *Coarse Mesh* described in Section 3.6.1. The problem here is reduced to a classical JICF, that is widely examined in literature. The very low resolution of the computational grid avoids the proper description of the turbulent motions, thus many scales of turbulence are completely filtered out and any kind of analysis concerning the higher order statistics or the small scales structures of the flow won't be carried out at this moment. Anyway, this first stage is important to check the consistency and the stability of the simulation at extremely high Reynolds numbers ($R_e \sim 10^{10}$), which are usually not reached in numerical experiments of JICF. Therefore, we test the agreement of this simulation with the main features and vortex structures of JICF, especially the CVP described in Section 1.2.2. Furthermore, this simulation provides for an estimation of the jet dimensions, useful to perform the following mesh refinement and domain reduction.

The simulation is run successfully without evidence of numerical instability, starting from the initial time $t = 0$ until $t_c = 3$ (600000 s), computed from Eq.3.17. Once reached the statistical steady state, the simulation is then run for 200000 s more, and a time average of the fields is computed over this time window.

Firstly, an assessment of the jet trajectory is performed. The streamline starting from the center of the jet exit (known as the center streamline, [41]) is computed from the time averaged velocity field. The streamline trajectory is projected on the vertical centre plane (x-z) and the data are fitted with the theoretical power-law in Eq.1.9 with $\gamma = 1/2$, adding a simple constant β to reduce the constraint of the fit:

$$z = \alpha\, x^{\frac{1}{2}} + \beta \tag{4.1}$$

The fit is performed in the entrainment region for $z > z_M$ as defined in Eq.1.8. The results are shown in Fig.4.1, focusing on the first half of the domain. The jet trajectory is in good agreement with the theoretical profile, with only slight deviations.

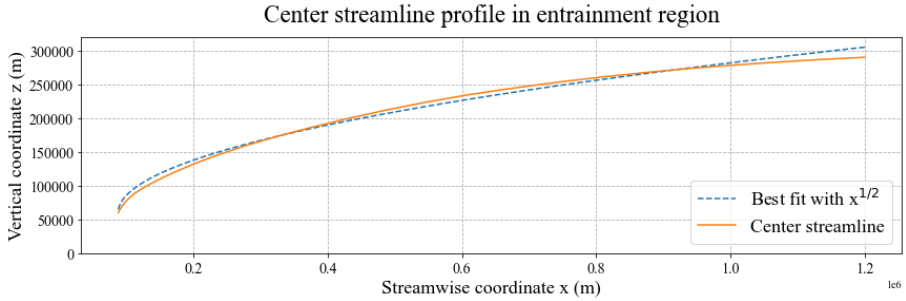

Figure 4.1: Plume trajectory at the vertical centre plane. Nonlinear interpolation of the simulated center streamline.

Other interesting elements can be pointed out by looking at the large scale vortices that appear in the system. As explained in Chapter 1, the most prominent feature of JICF is the counter-rotating vortex pair (CVP), therefore we expect that a good simulation should be able to reproduce this pattern. The analysis of turbulent features is usually performed by studying the vorticity and pressure isosurface [45] or pressure fluctuation isosurface [69]. The Q-criterion is here preferred to the above-mentioned ones after the analyses of Dubief and Delcayre [70]. Such method consists in the visualisation of the isosurfaces of the second invariant of velocity gradient tensor:

$$Q = \frac{1}{2}(\Omega_{ij}\Omega_{ij} - S_{ij}S_{ij}) \quad \text{where} \quad \Omega_{ij} = \frac{1}{2}\left(\frac{u_i}{x_j} - \frac{u_j}{x_i}\right) \tag{4.2}$$

This can be interpreted as the balance between rotational rate Ω_{ij} and strain rate S_{ij}. Hence, the isosurfaces of positive values are qualifed to be vortices delimiter. Fig.4.2 displays the $Q = 10^{-10}$ isosurface from two different angles. Several structures can be depicted, and especially Fig.4.2a is used to show the CVP, that is represented by the two large twisted tubes that tend to separate slightly going downstream. The Q isosurface is colored with the streamwise vorticity, that assumes positive and negative values on the right and left tube respectively, which is the result of the counter-rotation. The CVP can be observed also from vertical yz planes at different x positions, using the time averaged fields of the passive tracer c and U_z component of the velocity (Fig.4.3 and Fig.4.4). In Fig.4.3a and Fig.4.3b the structure of the time averaged passive tracer field shows an essentially symmetric CVP preserved along the streamwise direction. The counter-rotation is confirmed in Fig.4.4a and Fig.4.4b where a central region of positive velocity is surrounded by two symmetric regions with negative values. These results agree with the ones obtained by Parello [67] and Mahesh [42] for the JICF, at much higher resolution.

Finally, we can look also at the wake structures that appear in the simulation. The wake vortices are visible just behind the jet by looking at the Q isosurface in Fig.4.2b. Columns of vertical vortices arise from the bottom wall and arrive till the groove between the two branches of the jet, similar to the ones found by Cintolesi et al. [41] in the case of the BJICF. They persist downstream for all the length of the refinement region and until the half of the domain length. Looking at the color of the isosurface, which indicates the value of vertical vorticity, a succession of positive and negative vorticity can be observed, as typical of shedding vortices in the wake of solid obstacles. However, a deeper analysis of the origin of those vortices must be performed, because the high solid nozzle, even if free-slip, could play a role in the formation of such vortices. The present resolution is not sufficient for such investigation, thus we postpone this analysis to the following Section 4.2 with the refined mesh.

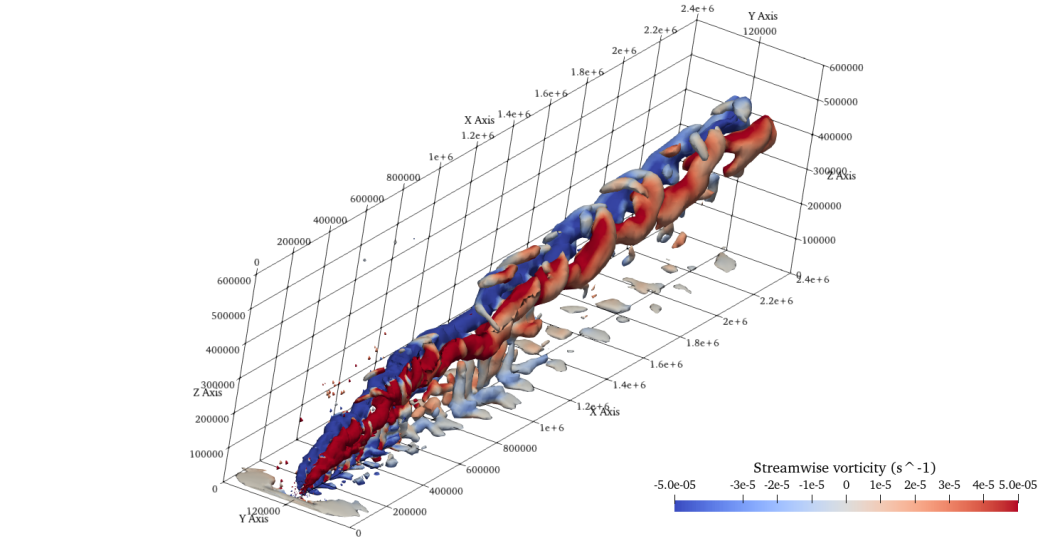

(a)

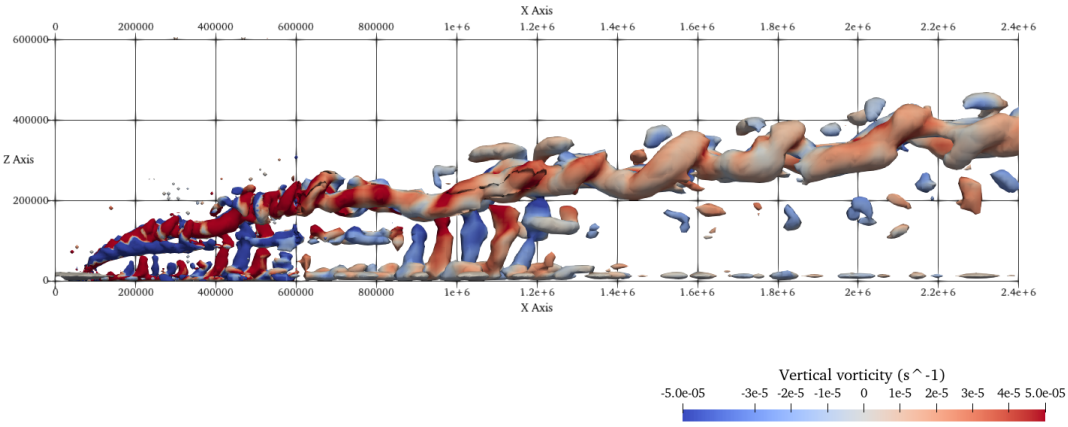

(b)

Figure 4.2: $Q = 10^{-10}$ isosurface from two different angles, colored with streamwise vorticity (Fig.4.2a) and vertical vorticity (Fig.4.2b).

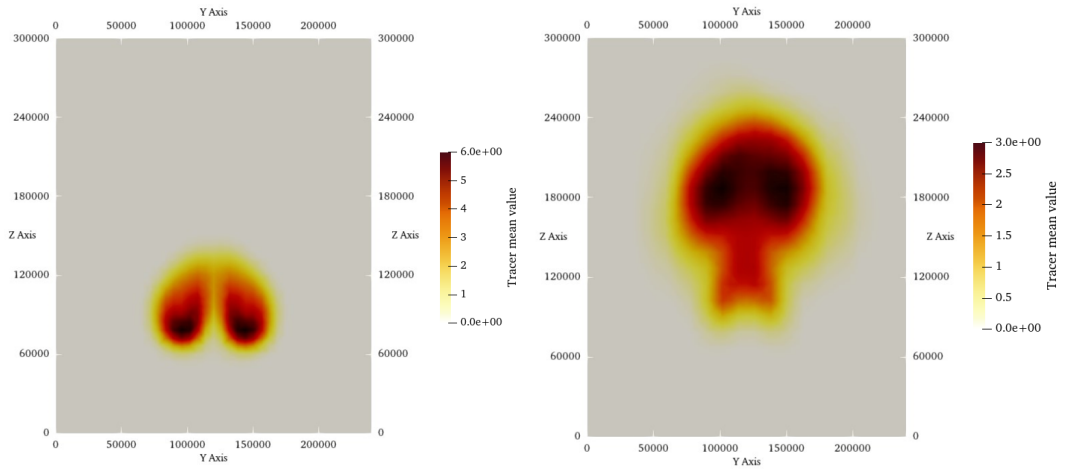

(a) (b)

Figure 4.3: Fig.4.3a: time average of the passive tracer c on a vertical plane at $x = 200\,\text{km}$. Fig.4.3b: time average of passive tracer c on a vertical plane at $x = 600\,\text{km}$. .

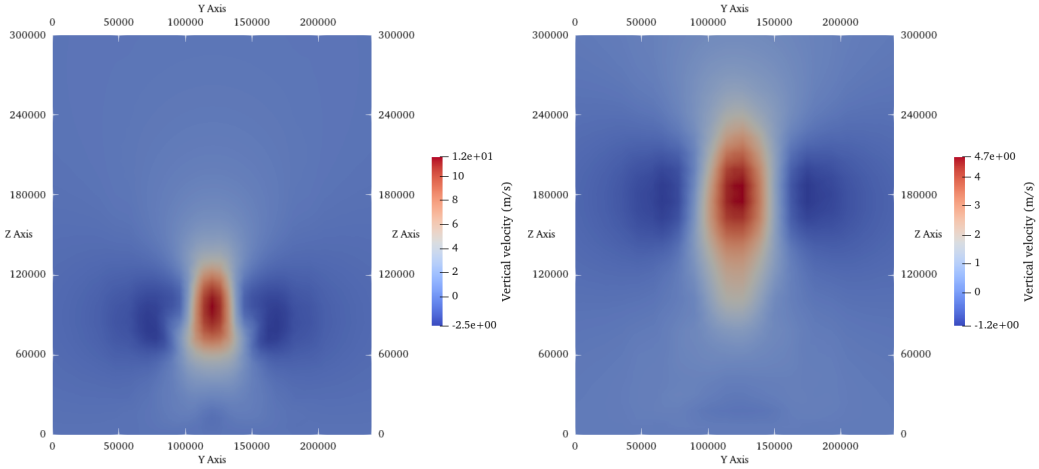

(a) (b)

Figure 4.4: Fig.4.4a: time average of vertical velocity on a vertical plane at $x = 200\,\text{km}$. Fig.4.4b: time average of vertical velocity on a vertical plane at $x = 600\,\text{km}$.

These overall results show a good agreement with the theory and the previous studies and we can conclude that, despite its low resolution, the *Coarse Mesh* is able to highlight the most relevant features of the momentum jet in cross flow. Therefore, in order to improve the numerical simulation accuracy and to better resolve the turbulent structures at smaller scales (above all, the possible formation of more evident wake vortices), we move forward with the mesh refinement.

4.2 Mesh refinement

The resolution of the computational mesh is a crucial element in LES, because it behaves as a spatial filter on the different scales of motion, determining the accuracy of the LES (see Section 3.2.2). According to [35], a grid spacing of 250 m or less is required for Large-Eddy Simulations to perform properly for the resolution of deep convective systems. Naturally, the computational cost increases rapidly with the mesh refinement, so we need to deal with our computational resources in order to choose an appropriate resolution that can be handled by the DIFA cluster. In this perspective, the four different computational grids presented in Section 3.6.2 are selected. These grids differ for their resolution and/or the extension of the refinement region, and require increasing computational cost: the purpose now is to perform a mesh assessment, comparing together the four different meshes, in order to choose the most suitable one. In this process of refinement, we also decrease the height of the free-slip cylinder to 1 km, to be more realistic in the description of the meteorological system.

Firstly, we apply a domain reduction in order to both save some cells necessary for the refinement and focus on a smaller portion of the system. This procedure must be done carefully in order to allow the flow to become laminar at the boundaries, so the domain dimension cannot be reduced too much. Using the information from the simulation with the *Coarse Mesh*, we select the isosurface of the tracer c corresponding to the 1% of the imposed value at the jet exit, as done in [41] (Fig.12). Then a qualitative measurement of the maximum width y_{max} and height z_{max} of this isosurface is performed with ParaView. The final width and height of the domain are chosen as $3\,y_{max}$ and $2\,z_{max}$ respectively,

resulting in the domain dimensions presented in Section 3.6.2: *Mesh_1*, *Mesh_2*, *Mesh_3*, *Mesh_4*. The length instead is set simply as 2/3 of the *Coarse Mesh* length.

The mesh assessment is done by selecting horizontal and vertical profiles of the time-averaged fields inside the refinement region. The time average is computed over 80000s ($\sim$1 day) once the simulation has run for 2 characteristic times. This interval is chosen after looking at the time series from the probes located inside the refinement region: at 2 characteristic times (but even much earlier) the instantaneous fields show turbulent fluctuations around a constant average value. This check is useful to assess qualitatively the realization of a statistical steady state. The results of the time-averaged profiles are shown in Fig.4.5.

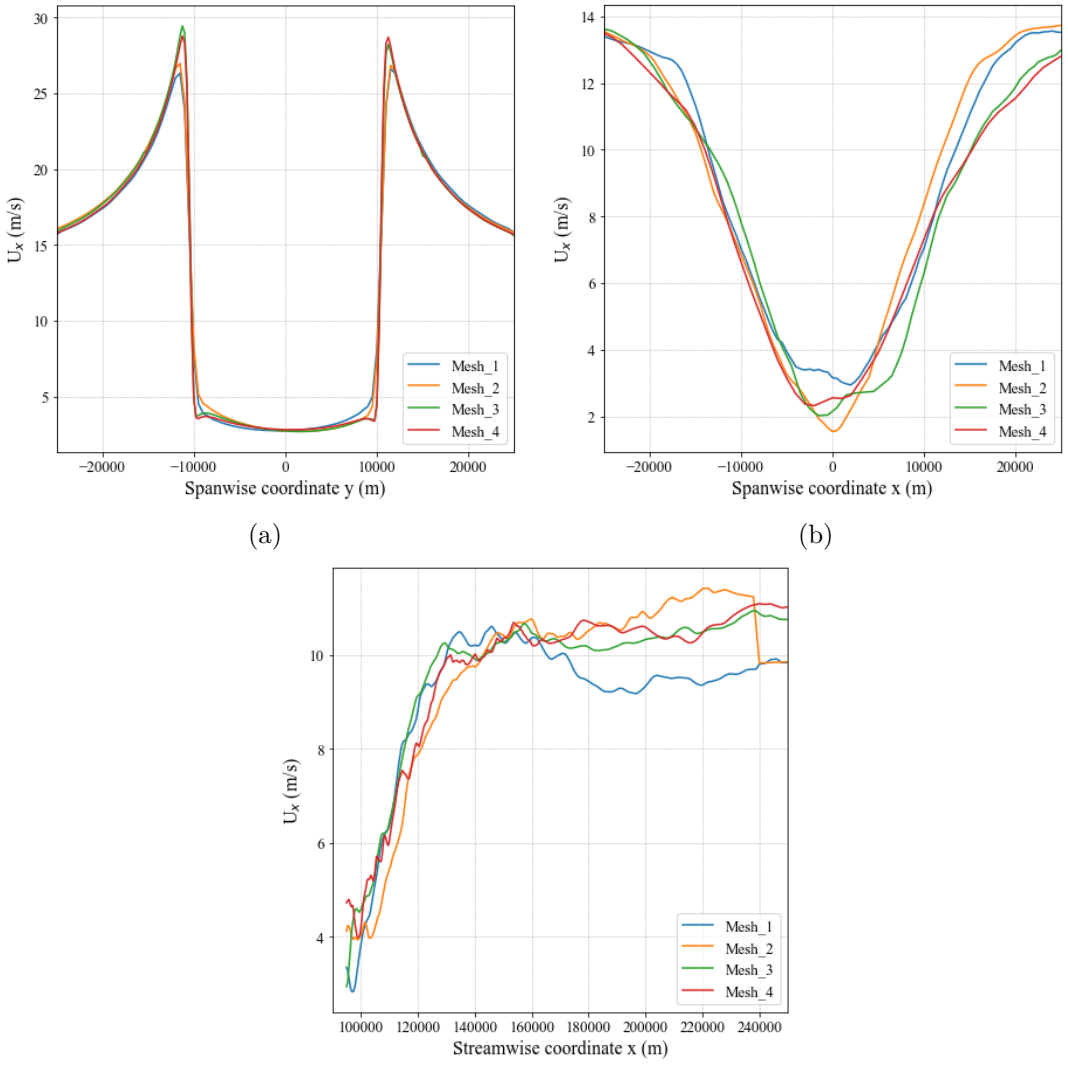

Figure 4.5: Fig.4.5a: time average of U_x on a spanwise direction at $x = 80\,\text{km}$ and $z = 7\,\text{km}$. Fig.4.5b: time average of U_x on a spanwise direction at $x = 120\,\text{km}$ and $z = 7\,\text{km}$. Fig.4.5c: time average of U_x on a spanwise direction at $y = 0\,\text{km}$ and $z = 7\,\text{km}$.

Three profiles are selected:

- a horizontal line in the spanwise direction at 7 km height and located at $x = 80\,\text{km}$, exactly above the jet exit (Fig.4.5a).

- a horizontal line in the spanwise direction at 7 km height and located at $x = 120$ km, that is 40 km downstream the jet (Fig.4.5b).
- a horizontal line in the streamwise direction at 7 km height and located at $y = 0$ km, exactly aligned with the jet wake (Fig.4.5c).

The 7 km height is chosen as a mean value in compliance with the real system, where the vortices are observed from the ground radar at vertical levels between 3 km and 10 km (Section 2.3). The results show a general agreement between the four simulations, with no marked differences. However, the *Mesh_3* and *Mesh_4* (which are the only ones with the resolution at 250 m) seem to perform slightly differently from the other two in some regions. More precisely, they resolve better the velocity profile in proximity of the jet (Fig.4.5a) and reveal a better agreement also in the wake if compared to the other two (Fig.4.5c). It is noteworthy that in Fig.4.5a all the simulations show the typical solid-obstacle profile of U_x, with two symmetric peaks on the left and the right of the central jet and a monotonous, smooth decrease on both sides to reach the value of the unperturbed crossflow far from the obstacle.

For a finer comparison between the four grids, in Fig.4.6 the Kolmogorov spectrum of turbulent kinetic energy (TKE) is plotted for each simulation. TKE is computed using the time series of the velocity field obtained from probe 3 in Fig.3.6 located in the middle of the wake. A Fast Fourier Transform (FFT) is applied and its square module is displayed in loglog plot. The black line in each graph indicates the $-5/3$ slope of the inertial subrange. No one of our grids is able to reach the 80% of the inertial subrange as an optimal LES should do, due to unavoidable limits of computational power (we are at the upper limit of resolution suggested by Bryan et al. [35]). We can assert that we are using an approach ascribable to the so-called Coarse LES, but anyway some studies still confirm the better accuracy of this coarse approach also compared to URANS, see [71]. Despite these limits of resolution, a non negligible portion of the $-5/3$ slope can be depicted, especially in *Mesh_1*, *Mesh_3* and *Mesh_4*, while *Mesh_2* does not show a clear trend.

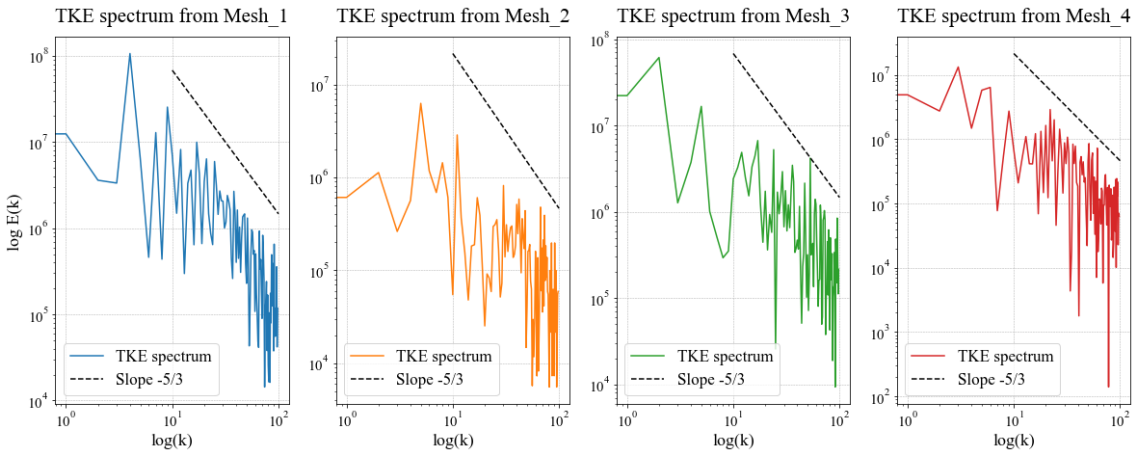

Figure 4.6: Kolmogrov spectrum computed from probe 3 for each simulation. Black dashed line indicates the -5/3 slope typical of the inertial subrange.

From these results we can conclude that *Mesh_3* and *Mesh_4* perform better if compared to the other two, especially *Mesh_2* seems to be the worst one. Furthermore in *Mesh_4*, compared to *Mesh_3*, the refinement at 250 m extends also to the wake region, without increasing too much the computational cost. Therefore, we select *Mesh_4* as the best one for our further analysis and the following steps.

4.3 *Mesh_4* analysis

In this Section, an analysis is performed to study the wake structures observed in the simulation with *Mesh_4*. The same mesh is also used to run the *High Cylinder* simulation, equal to the previous one, but with the cylinder of 20 km height as it was for the *Coarse Mesh*, in order to answer the question opened in Section 4.1: does the free-slip cylinder contributes to the generation of wake vortices? Is it then crucial to reduce the height of the cylinder to investigate the effect of the jet alone?

Firstly, we perform a Fourier analysis using time series of the magnitude of horizontal velocity $U_h = \sqrt{U_x^2 + U_y^2}$ from probes 3 and 6, to find the dominant frequencies in the time series. These two probes are selected because they are not too close to the jet and are located 40 km downstream the jet core, almost in the middle of the wake (considering that the vortices in the real case are observed until ~ 80 km downstream the supercell). In case of a regular vortex shedding, we should find a well-defined peak on a certain frequency in the power spectrum of the time signal. The FFT algorithm is employed, using the data from the same time window used for the mesh refinement analysis, then computing the module square of the FFT. The results are shown in Fig.4.7. From probe 3, a number of peaks (at least 4) of similar magnitude can be observed, without a clear evidence of a dominant frequency. Furthermore, from probe 6 a peak is found at wavenumber $k = 2$, which is however very low and refers to long period oscillations of the flow (~ 12 h).

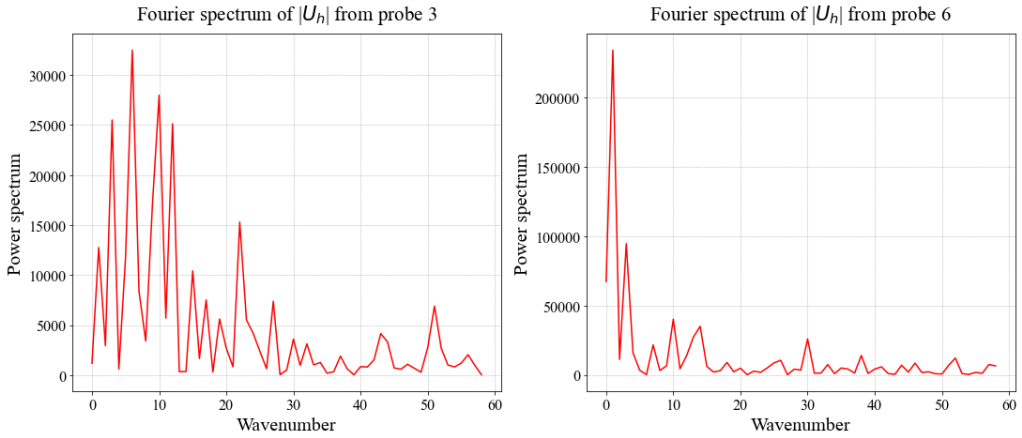

Figure 4.7: Power spectrum of time series of $|U_h|$, computed from Fast Fourier Transform algorithm with data from probes 3 and 6.

The comparison of power spectra with the velocity and vorticity fields displayed in Paraview, shows that these long-period oscillations do not refer to any vortex shedding, but are the result of the detachment of very incoherent regions from the vertical jet, where no evidence of regular vortices is found. An example is shown in Fig.4.8 with the contour plot of vertical vorticity, focusing on the wake region on a horizontal plane 7 km above the ground. Same results are obtained at other vertical levels.

Between the periods of detachment of the incoherent regions, well defined vortex structures appear at multiple levels. These vortices, that can be observed in Fig.4.9a from vertical vorticity contour plot as the three consecutive red spots detached from the right flank of the jet. From Q isosurface in Fig.4.10, they appear as "tornado-like" structures that occupy the whole column from the ground to the jet. Furthermore, no presence of tracer is found inside these vortices, as shown in Fig.4.9b which is taken at the same time of Fig.4.9a. Therefore, the vortices unlikely originate from the detachment of jet air.

These results are in agreement with the observations of Fric and Roshko [44] and Kelso et al. [43]. However, in our case the observed vortices do not exhibit the classical periodicity typical of von Karman wakes: they appear as trails of three/four vortices of the same sign instead of showing the alternation of VKVS past solid obstacles. In light of these results, we conclude that no similarities with the observed vortices in the Naples event are found with this configuration of the numerical simulation.

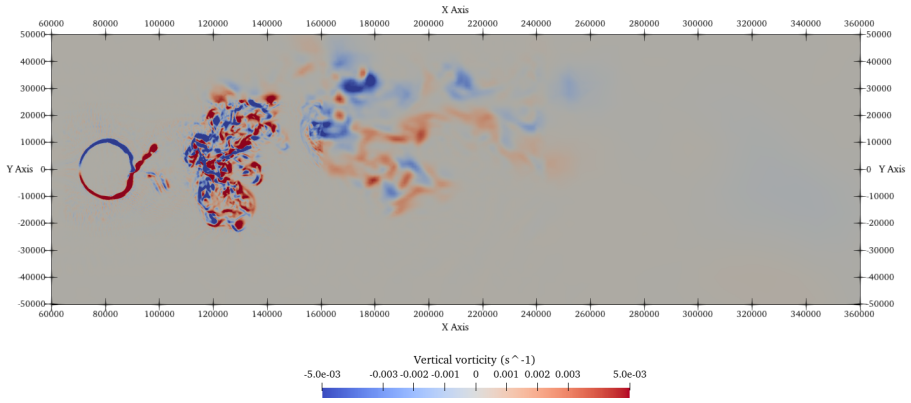

Figure 4.8: Contour plot of vertical vorticity at a representative time step, on a horizontal plane 7 km above the ground. The jet and the wake region are shown.

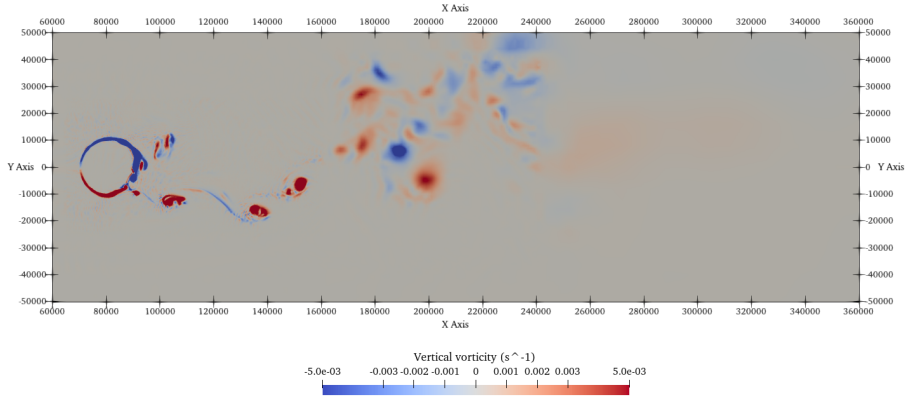

(a)

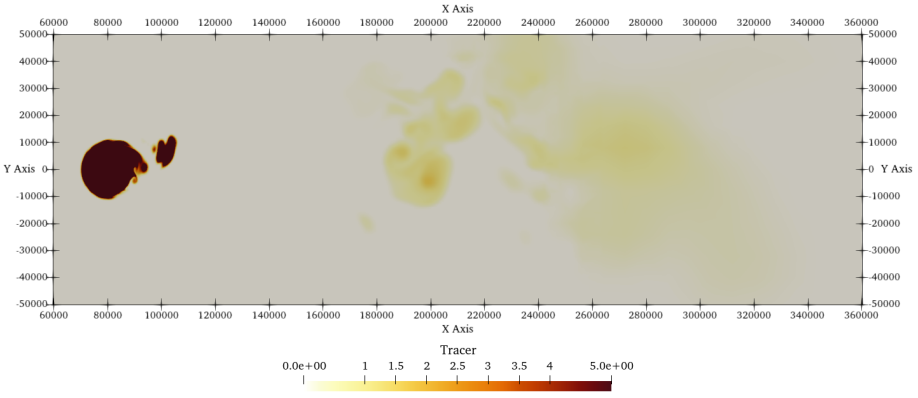

(b)

Figure 4.9: Fig.4.9a: horizontal plane with vertical vorticity contour plot, 7 km above the ground. Fig.4.9b: horizontal plane with passive scalar contour plot, 7 km above the ground, at the same time of Fig.4.9a.

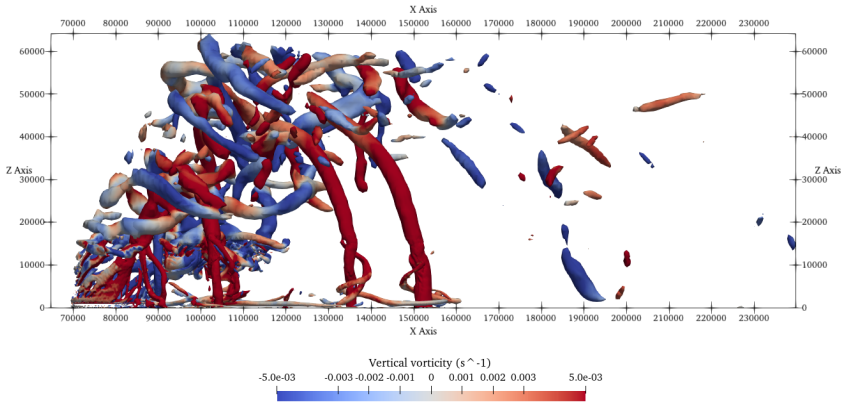

Figure 4.10: $Q = 10^{-5}$ isosurface, colored with vertical vorticity values, taken at the same time of Fig.4.9.

As final analysis of this Section, the same mesh is used to run the *High Cylinder* simulation with the cylinder 20 km-high, to investigate the effect of the solid cylinder on the wake structures. This was not possible with the *Coarse Mesh* due to the very low resolution. The power spectrum of $|U_h|$ is shown in Fig.4.11a only from probe 6 for sake of brevity: now a very sharp peak appears at wavenumber $k = 9$, corresponding to a period of ~ 9600 s. This is the result of a very regular vortex shedding similar to a classical von Karman vortex street, that is depicted for a particular timestep in Fig.4.11c. Coherent, alternated vortices start from the ground and arrive till the jet tilted downstream by the cross-flow. They seem to originate just behind the solid cylinder (see the first red vortex on the left in Fig.4.11c) and then, when advected downstream, they also grow in height once the connection with the jet is created. In order to investigate better the generation of these vortices, the velocity streamlines passing through a newly formed vortex are scrutinised (Fig.4.11b). The streamlines display a swirling structure that starts at the bottom and ends on the solid surface of the cylinder: the vertical jet exiting from the top of the cylinder seems to have no impact on their formation. Therefore, the solid cylinder, even if free-slip, plays a significant role in the vortex formation. So, in order to investigate the contribution of the jet alone, the dimension of the cylinder must be minimized, as we did in *Mesh_4*.

In conclusion, from the analysis in this Section we can assess that:

- the mere vertical jet in cross flow is not enough to generate the organised shedding vortices as observed in the real case. The simulated vortices appear in structure and shape consistent with the previous studies ([44],[43]), but their periodicity and alternation is very irregular and not compatible with the observed ones.

- the simulation with the high solid cylinder, even if free-slip, is able to generate well-organised vortices in the wake, with very regular periodicity. The generation of such vortices is found just downstream the solid cylinder near the bottom wall, which is the only patch where a no-slip condition is imposed. The vertical jet seem to play a marginal role in this case. In light of these results, we can suppose that also in the *Coarse Mesh* simulation, that has the same geometry of the *High Cylinder* one, the wake structures that we observe are likely generated primarily by the solid cylinder. Therefore, the lowering of the cylinder is crucial to observe the effect of the jet alone.

These results indicate the need to add higher levels of complexity in the physics of the system, since the simple vertical JICF is not sufficient for the generation of organized

wake vortices. In this thesis, we focus on the buoyancy and the updraft rotation typical of supercell storms.

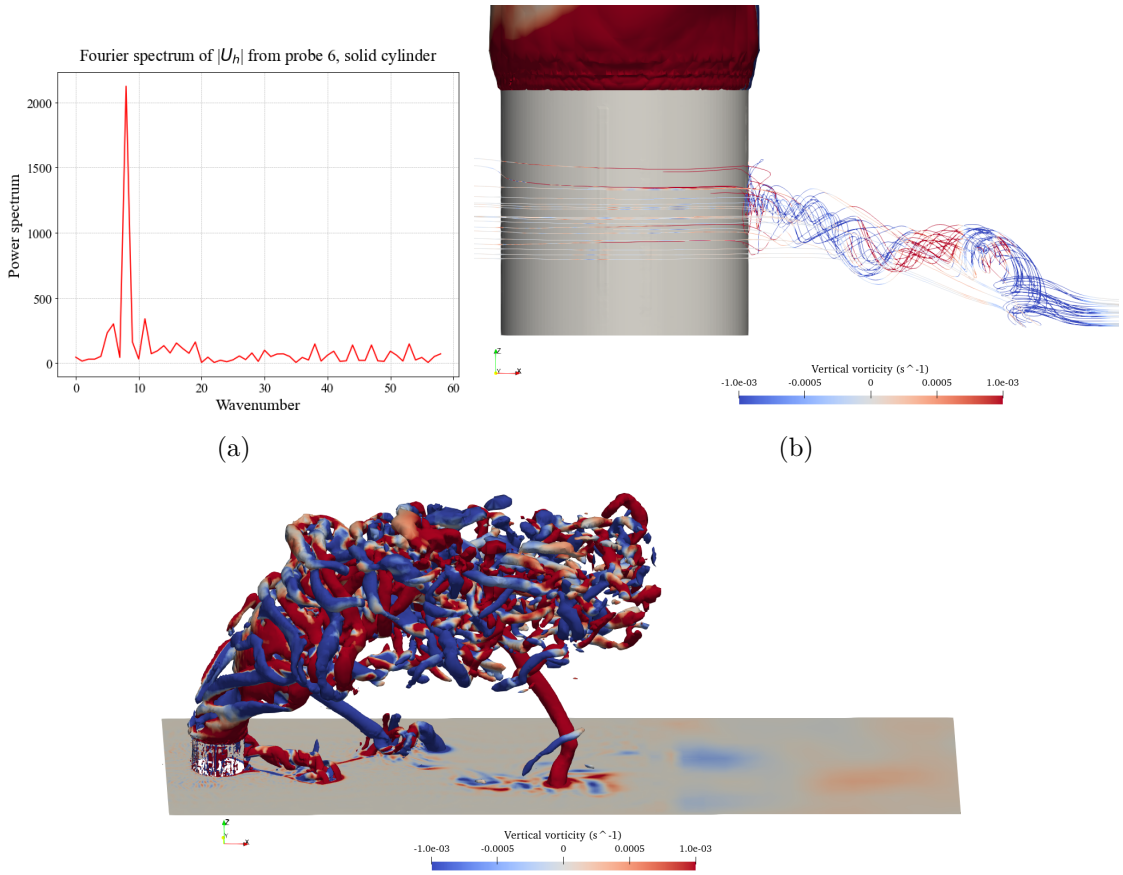

(a) (b)

(c)

Figure 4.11: Fig.4.11a: power spectrum of horizontal velocity module $|U_h|$ from probe 6. Fig.4.11b: streamlines of velocity field passing through a newly formed vortex behind the cylindrical nozzle (in grey). Fig.4.11c: $Q = 5 \cdot 10^{-5}$ isosurface colored with values of vertical vorticity; horizontal plane with vertical vorticity contour plot.

4.4 Buoyancy, rotation and sensitivity analysis

The convective motions in the atmosphere are driven by the buoyancy. Therefore, the implementation of the temperature equation is crucial and cannot be neglected. The presence of a thermal stratification of the environment is also pivotal to reproduce the tropopause and limit the vertical motions to the troposphere. As explained in Section 3.7, the description of thermal stratification is simplified, imposing a neutral stratification in the troposphere instead of an unstable stratification, in order to avoid instabilities in the simulation. The implementation of buoyancy leads to the generation of a BJICF, not a JICF anymore.

The second contribution we want to investigate in this thesis is the updraft rotation. The uncertainty on the estimation of the rotation is large, as well as the extension of the area interested by the rotation itself. It is useful to decouple the effect of rotation from the one related to the buoyancy, in order to understand the impact of these separate contributions on the updraft and especially on its wake.

Finally, given the high uncertainty on the estimation of the initial conditions, a sensitivity analysis can be performed by varying some critical parameters in the simulation, such as the updraft width, the crossflow velocity or the updraft velocity. In this work, we decide to investigate the sensitivity to updraft width variations, which are performed using different diameters D of the cylindrical nozzle at the basis.

In conclusion, to study all these aspects just presented above, six different simulations are run. Since the computational cost needed to run the simulations on *Mesh_4* is huge but still manageable, we decide to further increase slightly the dimension of the refinement region at 250 m resolution in *Mesh_4*, in order to resolve better the overshooting top and the wake. This new mesh is described in Section 3.6.3 as *EnhancedMesh_4*. Finally, one more simulation is performed with exactly the same geometry of *EnhancedMesh_4*, but the refinement region reaches 200 m resolution: we refer to this mesh as *MaxResMesh*.

In light of these considerations, the six simulations performed are listed in Table 4.1. The simulation from 1 to 5 are with *EnhancedMesh_4*, while the Sim.6 is run with *MaxResMesh*.

	Sim.1	**Sim.2**	**Sim.3**	**Sim.4**	**Sim.5**	**Sim.6**
Buoyancy	✓	✓	✓	✓	✓	✓
Rotation	✗	✗	✗	✓	✓	✓
***D* (km)**	20	29	15	20	29	29
Max. Res. (m)	250	250	250	250	250	200

Table 4.1: List of all the six final simulations performed.

The absence of the simulation with rotation and $D = 15$ km, as will be explained later in Chapter 5, is due to the results observed for Sim.4 and Sim.5, where the effect of rotation appears critical. Therefore, we decided not to use rotation with $D = 15$ km. All the simulations are run for 125000 s, which is 2.5 characteristic times according to Eq.3.17. This is fairly sufficient to the realization of a steady state. It is of course a much longer time window compared to the real system duration, but this is necessary in order to collect a sufficient statistics for the analysis of the wake in the steady state.

In the next Chapter, the analysis of the simulations in Tab.4.1 is be carried out.

Chapter 5

Final simulations analysis

In this Chapter, the results of the six final simulations are investigated, in which the supercell is simplified with a BJICF, with or without rotation. Firstly, in Section 5.1 we apply the same Fourier analysis to all the different simulations in order to identify the presence of regular and periodic structures in the wake. The comparison of the results among the six simulations, allows to select the one where the vortex shedding is better reproduced. This selected simulation is then investigated in deeper detail in Section 5.2 in order to study the origin of the periodic structures observed and if they are attributable to shedding vortices. In Section 5.3 an analysis is conducted to compute the geometrical and physical parameters related to the simulated vortices, to compare with the observed ones in the real case. Finally, in Section 5.4 we further check the consistency of the simulation in reproducing correctly other relevant meteorological features, such as the updraft maximum velocity, the overshooting top height and the generation of hydraulic jump and vertically propagating gravity waves in the lee of the OT.

5.1 Comparison between simulations

In Chapter 4 the analyses have been performed for the statistical steady state only. In this Chapter we would like to investigate all the different phases of the system evolution, starting from the updraft growth. This allows also to make a comparison with the observed Naples supercell, from SEVIRI data in the infrared band presented in Marra et al. [10].

Data from the probes located in the wake downstream the updraft, point out roughly three different phases of the motion:

- the updraft growth
- a transient period of adjustment
- the onset of turbulence in the wake with the shedding of more or less organised vortices depending on the simulation.

The first step of the analysis aims to the isolation of these three periods, with the same approach in all the six simulations. Unfortunately, very little literature can be found about this kind of analysis, especially concerning the duration of the transient period. Therefore, an original method will be adopted.

The updraft growth is estimated from a probe on the vertical of probe 1 in Fig.3.6, but located slightly above at the tropopause, at 13 km height. Vertical velocity U_z and buoyancy (b) time series are extracted from this probe, and multiplied together in order to obtain a scalar field $U_z b$. In this region, the buoyancy value is negative because the

updraft has already overshot into the stratosphere, while the vertical velocity is large and positive when the updraft reaches this level for the first time, because the effect of negative buoyancy is still small at 13 km. Therefore, the value of $U_z b$ has to be large and negative at the moment of the updraft impact. So we look for the first negative minimum in the time series of $U_z b$, and refer to the corresponding time as the instant when the updraft hits the tropopause (the calculation neglects the first 2 minutes of simulation where we observe some very small fluctuations around zero not compatible with the updraft presence). The results are presented in Tab.5.1 for all the six simulations. The data in Marra et al. [10] provide an estimation of ~ 20 min (see Fig.2.2), from the first moment when the SEVIRI satellite observes the updraft formation up to the time when it reaches the tropopause. Therefore, are in good agreement for the majority of the six simulations. In Fig.5.1 the results are reported with the red line only for the three simulations without rotations, for sake of brevity. In all simulations it is possible to notice the presence of a large fluctuation few minutes after the red line position. This is explainable considering that the red line is obtained with data on the vertical of the updraft at 13 km height, while the time series is plotted for probe 3 located 40 km downstream the updraft, where the perturbation induced by the updraft growth arrives delayed.

	Updraft reaching tropopause (min)	**End of transient (hours)**
Sim.1	23	3.4
Sim.2	20	3.1
Sim.3	18	3.5
Sim.4	22	1.8
Sim.5	20	2.4
Sim.6	29	2.3

Table 5.1: Duration of updraft growth and transient period for all the six simulations performed. Results are reported with two significant digits. The times are computed from the beginning of the simulation at $t = 0$.

The beginning of the transient period is fixed at the end of the updraft growth. However, the estimation of the duration of the transient period is more complicated to carry out. The transient behaviour avoids the calculation of statistics representative of the whole interval of time, because the statistical steady state is still not reached. Firstly, for this analysis the data from probe 3 in Fig.3.6 are used for the simulations with no rotation, while when rotation is present we use data from probe 6, because the cyclonic rotation tends to tilt the turbulent wake on the left so we judge probe 6 more reliable. These two probes are assumed good indicators of the properties of the whole wake region for their location in the middle of the wake. The approach we use is to divide the time series into short intervals of 20 minutes each, for which we assume that the statistical properties of turbulence do not change appreciably (that is the realization of the Taylor's frozen turbulence hypothesis). Then the Root Mean Square velocity (RMS) is computed for each of these 20min intervals as:

$$RMS_U = \sqrt{\langle U'U' \rangle} \tag{5.1}$$

where the square brackets indicate the time average and U' is the velocity fluctuation from the time average. The onset of turbulence is observed as a very sharp transition from the

time series of the probes (see Fig.5.1); therefore the end of the transient period is fixed, for each simulation, at the beginning of the i^{th} 20min interval which satisfies the condition:

$$RMS_U^i > 3\,RMS_U^{i-1} \tag{5.2}$$

In other words, we select the time when the corresponding RMS is statistically different from the previous one. The uncertainty on these estimations is evaluated as ±20min, the length of the short time intervals. This method is applied for all the six simulations (Tab.5.1), with good results, as shown in Fig.5.1 with the green lines: the position of these lines roughly coincides with the onset of large fluctuations attributable to the turbulent regime. The results show that the presence of rotation brings forward the onset of turbulence in the wake. In absence of rotation, is evident also that the increase in updraft diameter brings forward the onset of turbulence, too. If compared to the real case, where the vortices in the wake are observed starting from 1.5/2 hours from the beginning of the event, it is clear that almost all the simulations tend to overestimate the duration of the transient period.

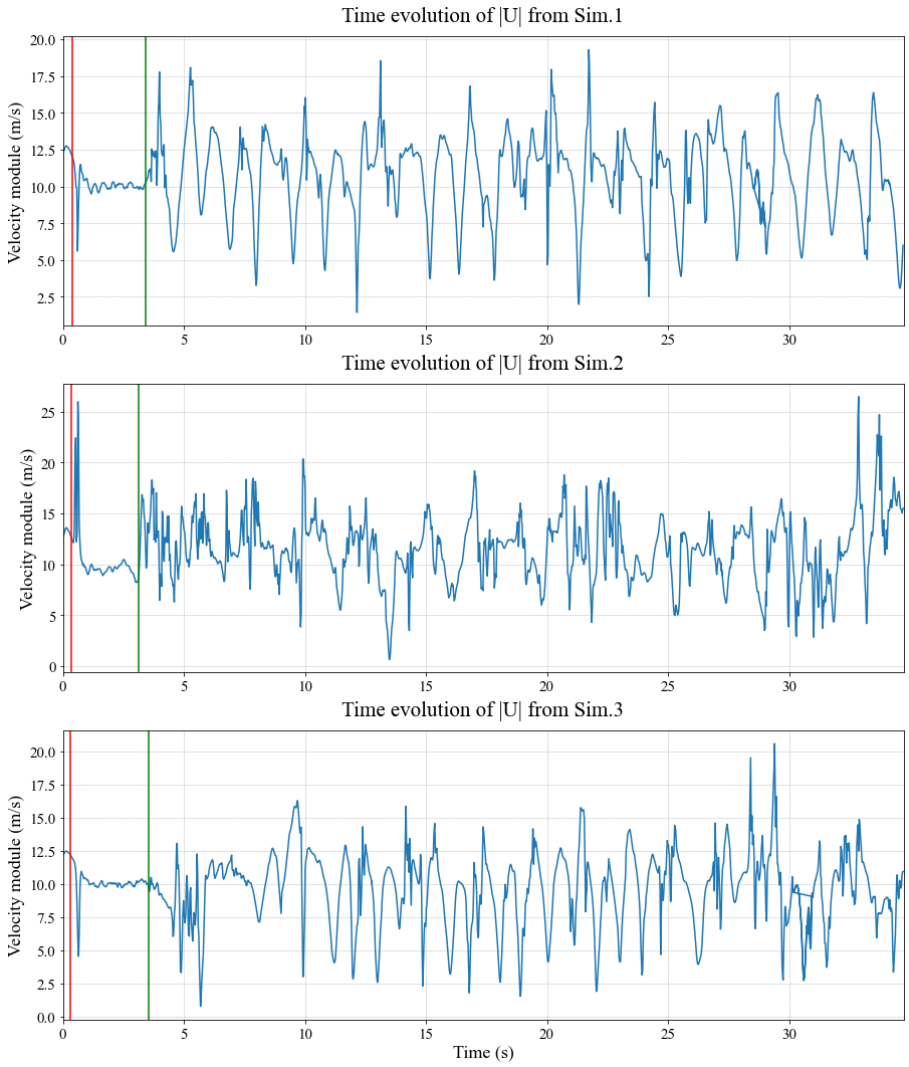

Figure 5.1: Time series from probe 3 in Sim.1, Sim.2 and Sim.3. In red line the instant corresponding to the updraft reaching the tropopause; in green line the instant corresponding to the end of the transient period.

Once identified the end of the transient period, we can focus the analysis on the following interval when turbulence arises in the wake in the form of more or less organized structures. In this Section, a Fourier analysis is performed as in Section 4.3, using data from probes 3 and 6 for each simulation, starting at the end of the transient period up to the end of the simulation (125000 s). Probes 3 and 6 are used as reference, but the results do not change significantly using probes on the same horizontal coordinates but at different vertical levels between 3 km and 10 km (not shown here for sake of brevity). This is a first evidence of a vertical homogeneity of the wake structures in this layer, which will be shown better in Section 5.2 through the Q isosurfaces.

The results highlight a marked difference between the simulations with rotation (Sim.4, Sim.5, Sim.6) or without (Sim.1, Sim.2, Sim.3). If rotation is absent, sharp peaks are identified in the power spectrum, especially from Sim.1 and Sim.3. This is coherent with the regular shedding of vortices from the updraft, as it was for the solid cylinder in Fig.4.11a. The periodicity can be guessed also looking at raw data in Fig.5.1, where especially Sim.1 is the one which shows the most periodic pattern all over the time window.

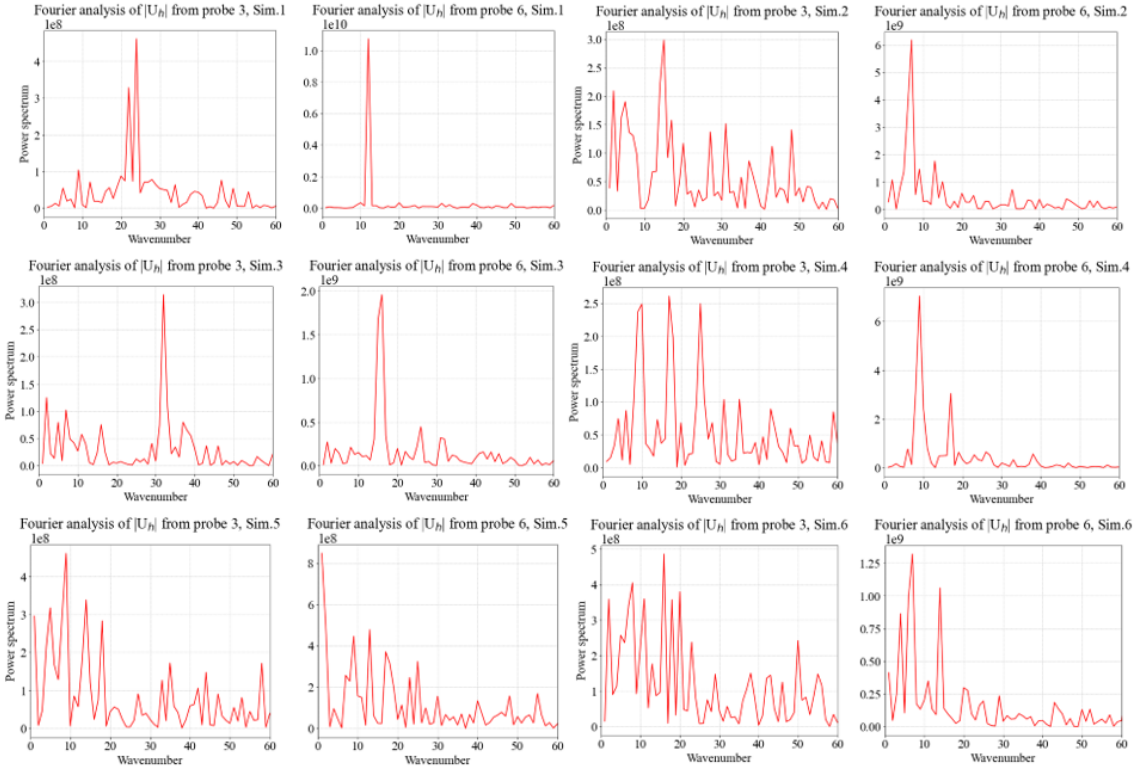

Figure 5.2: Power spectra of horizontal velocity module $|U_h|$ from probes 3 and 6 for each of the six simulations investigated. The y-axes have different units in the different power spectra.

If rotation is present (Sim.4, Sim.5, Sim.6), many different peaks of similar amplitude are found in the power spectrum, which can be interpreted as an absence of a clear, regular periodicity in the wake region. This behaviour can be found in almost all the other probes (not shown here), and also looking at the velocity field on horizontal planes in Paraview does not reveal any evidence of a regular vortex shedding, but only a turbulent, incoherent wake develops downstream the updraft. Only in Sim.4, probe 6, a more evident peak is reproduced by the power spectrum. Further investigations reveal that this pattern is ascribable to the shedding of consecutive vortices of the same sign (anticyclonic) for the

majority of the time evolution, so not compatible with the observations. Therefore, a strong cyclonic rotation seems to favour the formation of anticyclonic vortices, which arise from the left flank of the updraft. This result is coherent with Kumjian et al. [72], but does not match with the observations of the Naples supercell. In Fig.5.3, an example of the just mentioned behaviour at a representative frame. The presence of vortices is visible from the sharp variation from negative to positive streamwise velocity going in the y direction, which indicate the presence of a local rotation.

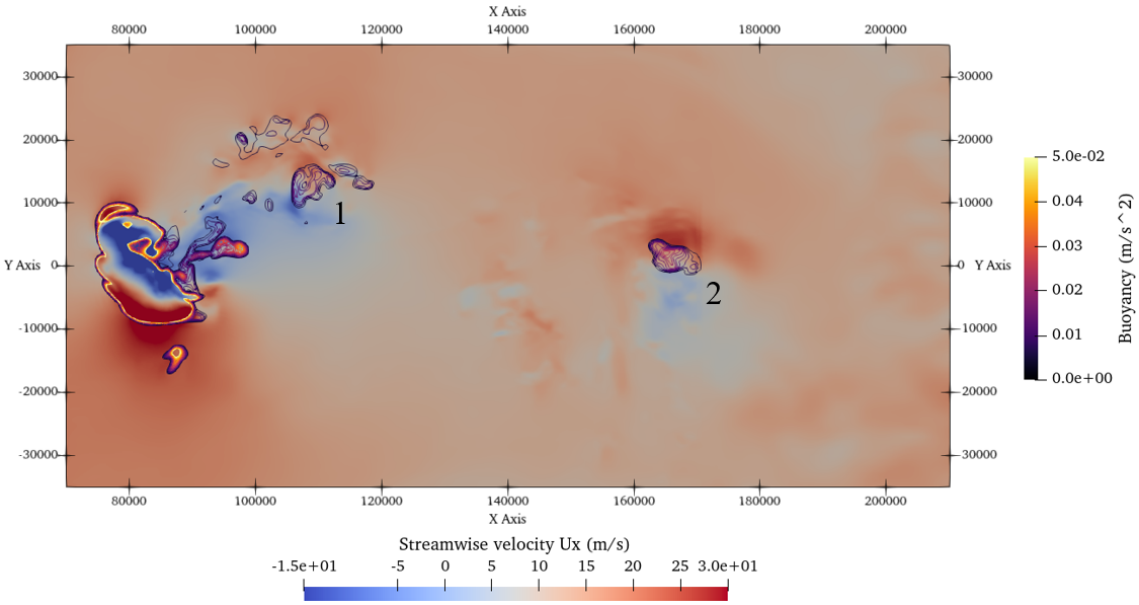

Figure 5.3: Plot of streamwise velocity U_x with contour plot of buoyancy, on a horizontal plane at $z = 7\,\text{km}$ height. The numbers 1 and 2 identify the two consecutive anticyclonic vortices in the wake.

From this frequency analysis, we conclude that:

- Sim.1, Sim.2 and Sim.3 are the ones where a marked periodicity is found, coherent with the shedding of periodic vortices in the wake. Compared to the results in Section 4.3 (especially, Fig.4.7), here the addition of buoyancy and tropopause seems to play a crucial role in the generation of periodic wake structures. The exact nature of these periodic structures will be investigated in detail in the next Section 5.2. It is also worth noting that in all the three simulations, the wavenumber corresponding to the peak in probe 3 is twice the wavenumber observed in probe 6. This is indeed compatible with von Karman-like vortices, due to the fact that probe 3 feels the effect of vortex shedding from both sides of the updraft, while probe 6 registers only the passage of vortices on the left side, resulting in a halved frequency.

- the presence of rotation destroys much of the regular periodicity in the wake, especially for large values of the updraft diameter. With $D = 20\,\text{km}$ (Sim.4), the rotation seems to favour the formation of anticyclonic vortices at expense of the cyclonic ones. The uncertainty on the estimation of updraft rotation from Doppler radar is very large, therefore an overestimation of its magnitude is likely, and this could contribute to affect the results. The effect of a smaller rotation is not investigated in this thesis. In any case, at this level, the rotation does not seem to play a relevant role in the generation of vortices, therefore the analysis of wake structures will focus only on Sim.1, Sim.2 and Sim.3 in the following Sections.

As final analysis of this Section, the comparison is performed between Sim.5 and Sim.6, which have the same geometry but different resolution (the former is run with *EnhancedMesh_4*, the latter with *MaxResMesh*). Although these two simulations have the rotation implemented, which is critical for the development of periodic structures as explained above, it is worth studying the effect of a 20% increase of the resolution, so that it could be applied also to the other simulations in case of positive results. The study is conducted as in Section 4.2, with the comparison of time averaged profiles of U_x and TKE spectra. From the profiles in Fig.5.4 we observe that the main features are preserved in both simulations and no important differences can be noticed.

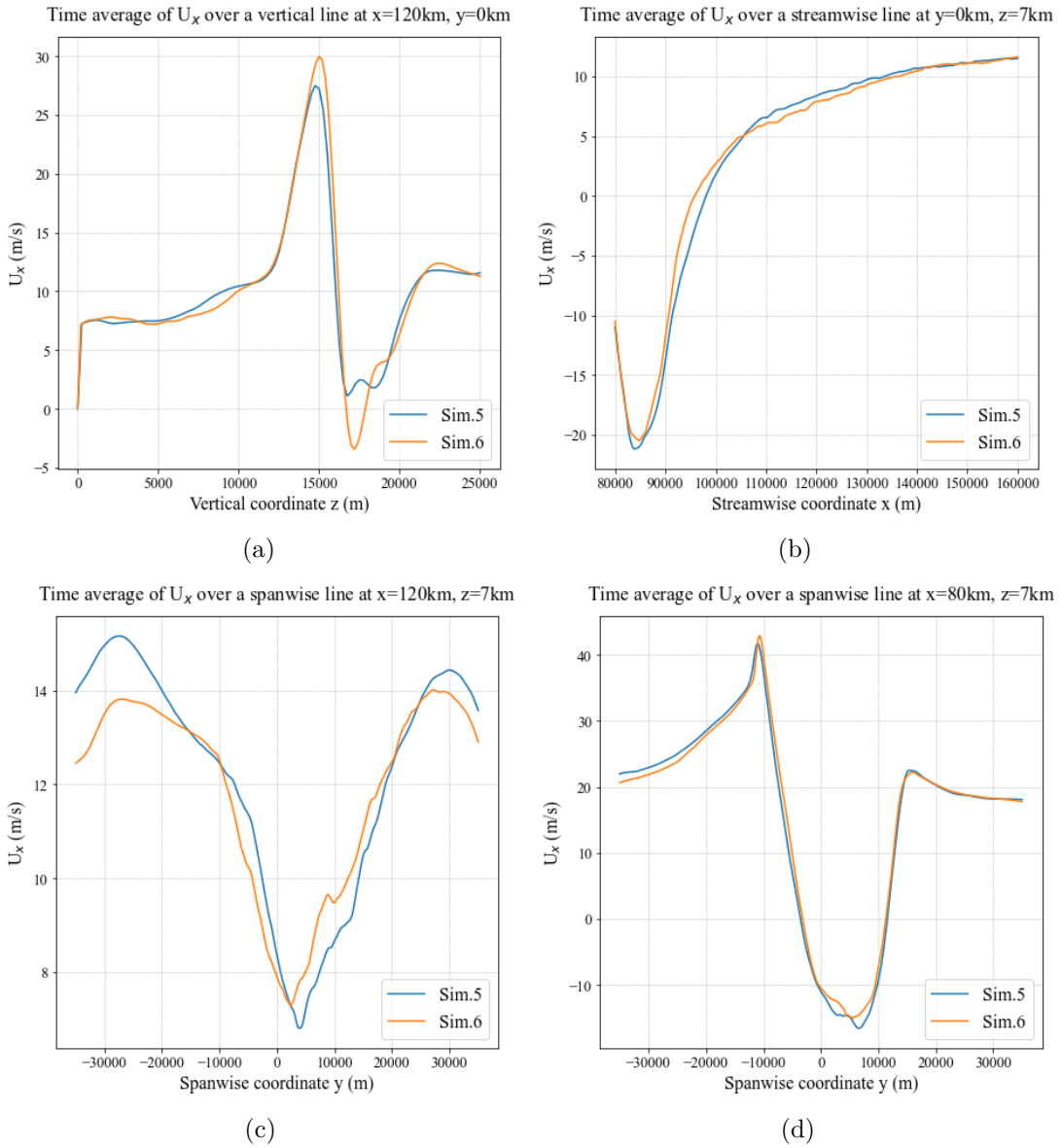

Figure 5.4: Fig.5.4a: time average of U_x on a vertical direction at $x = 120\,\text{km}$ and $y = 0\,\text{km}$. Fig.5.4b: time average of U_x on a streamwise direction at $y = 0\,\text{km}$ and $z = 7\,\text{km}$. Fig.5.4c: time average of U_x on a spanwise direction at $x = 120\,\text{km}$ and $z = 7\,\text{km}$. Fig.5.4d: time average of U_x on a spanwise direction at $x = 80\,\text{km}$ and $z = 7\,\text{km}$.

Sim.6 seems to describe better the region above the tropopause where a strong variation in the U_x is present (Fig.5.4a), which results also in an inversion of the flow at $\sim 17/18\,\text{km}$.

This behaviour in the lee of the overshooting top will be investigated better in Section 5.4, but we can anticipate that it is likely the result of the presence of the overshooting top upstream, which acts as an obstacle for the cross-flow, inducing the typical decrease in pressure in the region behind as the crossflow separates around the overshooting top (see flow behind obstacles in Section 1.2). Both simulations can reproduce well the asymmetry generated by cyclonic rotation in Fig.5.4d, to compare with Fig.4.5a. The most evident differences emerges from Fig.5.4c, even though the overall trend is respected. Finally, the Kolmogorov spectrum in Fig.5.5 does not show important differences, too, since the -5/3 slope is well visible in both simulations.

From this analysis, we conclude that no relevant differences or remarkable improvements are observed between Sim.5 and Sim.6. This is a good demonstration that also the 250 m resolution is a valid choice for the numerical simulation of the system taken into account. However, due to the presence of rotation, the periodicity in the wake is lost in both simulations, therefore we cannot assess if the increase in resolution has some impact on the organised wake structures.

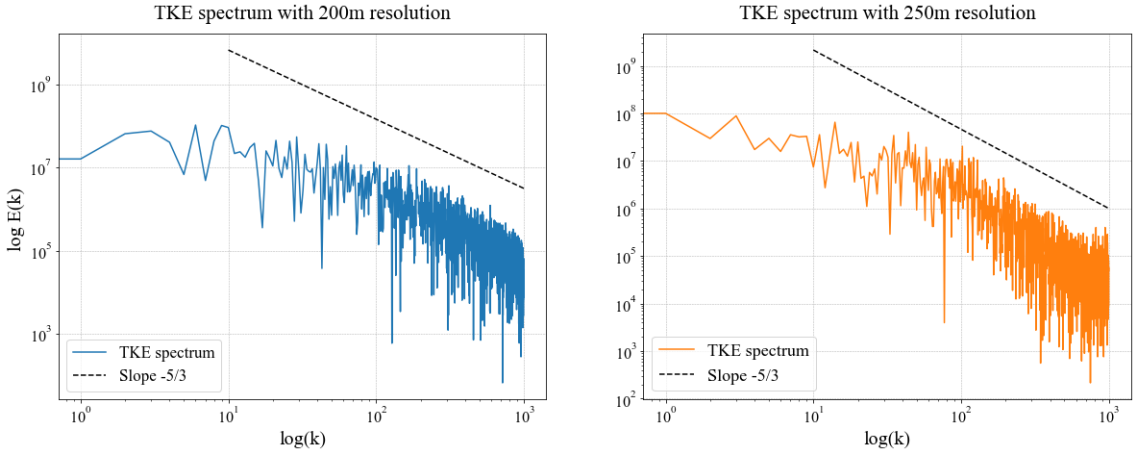

Figure 5.5: Kolmogorov spectrum computed from probe 3 for Sim.5 and Sim.6. Black dashed line indicates the -5/3 slope typical of the inertial subrange.

5.2 Shedding vortices analysis: physical origin

In light of the results of the previous Section 5.1, now the focus is put on the simulations without rotation (Sim.1, Sim.2, Sim.3) to investigate the features of the periodic structures in the wake observed from Fourier analysis. We firstly analyse the origin of these structures, in order to determine also if they are real vortices or simply incoherent regions that shed from the updraft with a regular periodicity (this cannot be established by the Fourier analysis only). The following analysis focuses on Sim.1 only, which is the one that reveals the most regular pattern from the FFT, but the procedure has been applied equally to Sim.2 and Sim.3 with same results. Using Paraview it is possible to visualise the output of the simulation every 5 minutes, which is the selected write interval. The observation of the velocity field on the usual horizontal plane at 7 km altitude (Fig.5.6a), taken at one representative instant of time, reveals a regular generation of vortices from the right and left flanks of the updraft, with three vortices that are visible in this frame (the first at $x \sim 110000$ m, the second at $x \sim 160000$ m and the third at $x \sim 230000$ m). The alternation of vortices with opposite sign is now correct, as shown by the plot vertical vorticity (Fig.5.6b), conversely to what we obtained from the *Mesh_4* simulation with

no buoyancy. Fig.5.6b also reveals many structures at small scale, but the three vortices mentioned above (two positive and one negative) emerge as the most prominent elements in the wake. One of the two positive vortices appears almost dissipated as it is located at the end of the buffer region of the mesh at 1 km resolution. Therefore these vortices persist longer than the observed ones, which are observed approximately until 80/100 km from the supercell core: in the real event a number of perturbations can affect the propagation of the vortices, such as the presence of topography or the variation in environmental conditions, which are not present in the numerical simulation. The three vortices depicted from Fig.5.6b do not have sharp borders as for the case of the solid cylinder (Fig.4.11c); however, one property that distinguishes the three vortices from the other smaller structures is the evident presence of buoyancy inside them, as shown from contour lines in Fig.5.6a. This behaviour differs completely from what observed in the vortices analysed in Fig.4.9a and Fig.4.9b in Section 4.3, and suggests another mechanism of generation.

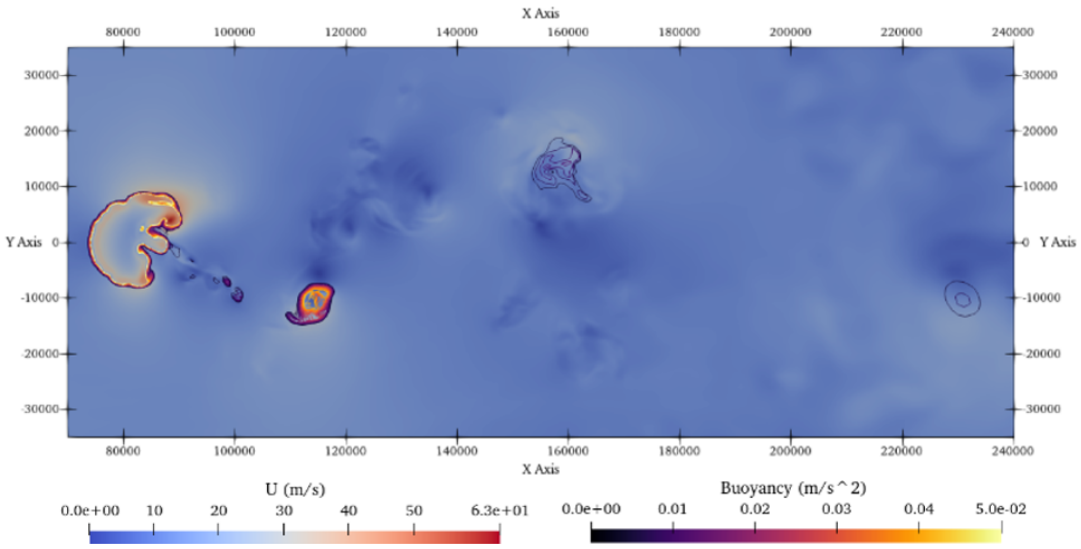

(a)

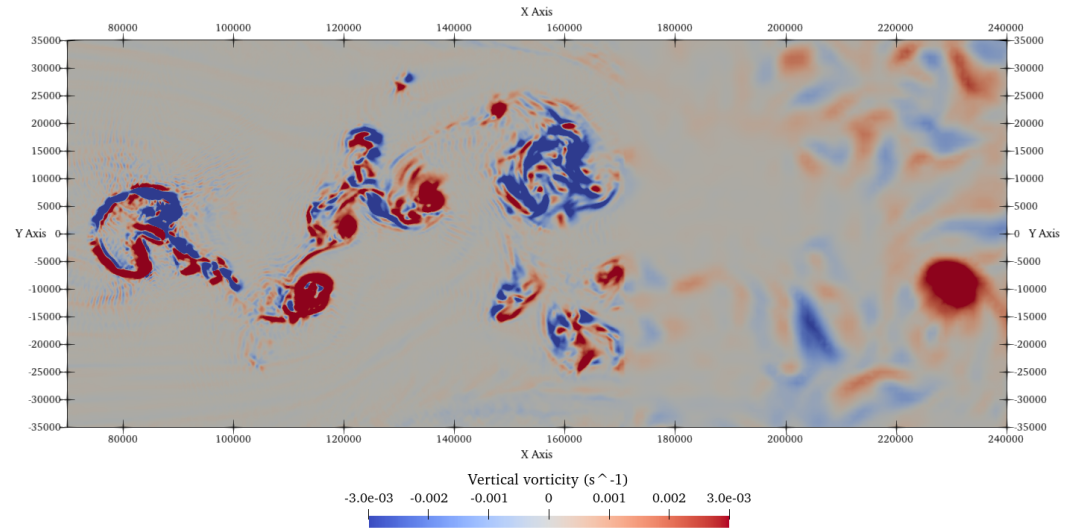

(b)

Figure 5.6: Fig.5.6a: plot of velocity field magnitude U and contour lines of buoyancy on a horizontal plane at 7 km height, taken at a representative frame. Fig.5.6b: plot of vertical vorticity on a horizontal plane at 7 km height, taken at the same instant of Fig.5.6a.

To investigate the origin of these vortices, we select one vortex taken as an example in the time series, always referring to Sim.1 but no differences are observed with Sim.2 and Sim.3. Fig.5.7 contains five plots of buoyancy and streamwise velocity taken every 15 minutes on the 7 km height plane, showing the generation of an anticyclonic vortex on the left side of the updraft. At time t_0 the vortex starts to generate, and appears as a branch protruding from the main updraft with a hook shape, which results from the anticyclonic recirculation. Under the drag of the crossflow, the protruding branch develops further at $t_0 + 15$min; the entrainment of environmental air gradually cools the new vortex and reduces the value of buoyancy inside it; the complete process of detachment lasts about 45 minutes, and finally the vortex is advected downstream in the wake by the cross-flow.

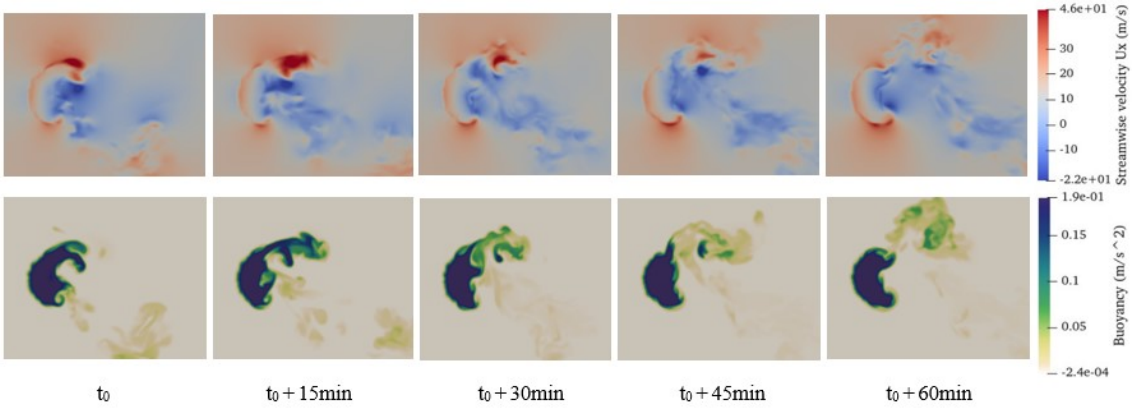

Figure 5.7: Streamwise velocity and buoyancy plot at five different frames taken every 15 minutes, on a horizontal plane at 7 km height, showing the process of vortex generation.

This process of generation is also investigated by the visualization of streamlines passing through a sphere of 2 km radius located in the centre the vortex at time t_0+30min. This sphere completely falls into the vortex, so that it is possible to estimate the main contributions to the vortex formation. In Fig.5.8a, the swirling structure of the upward anticyclonic vortex is well visible; the streamlines originate partially from the updraft itself (which are the ones that also contain buoyancy) and partially from the crossflow which is entrained in the updraft and deflected upward by the vertical flow. Moving downstream, the streamlines reach the tropopause and stop their vertical motion and reach the equilibrium, contributing to the formation of the anvil. This analysis allows to distinguish between the classical von Kármán vortices and the ones reproduced by the numerical simulation: even though the pattern observed in the wake is very similar in both cases (see Fig.5.6a), the origin of the vortices is different. While the classical VKVS originating from solid obstacles involves the generation of vorticity from the shear produced in the viscous boundary layer, here the vortex formation resembles the one found in Cintolesi et al. [41] at the origin of the CVP in the case of a BJICF. In agreement with the analysis proposed by Denev et al. [69], the vertical plume above the nozzle acts as an obstacle for the crossflow and generates a recirculation region in the plume rear. Differently from the case of solid obstacle, the plume pulls upward the fluid producing a vertical velocity that combines with the rotating motion of the recirculation vortices and gives rise to helicoidal vertical flows.

Interesting to observe the difference with the case of the solid cylinder, where the bottom surface played an important role in the vortex generation (Fig.4.11b), while now it does not seem to influence the formation of the vertical vortex, which develops directly above the nozzle and it is driven by the entrainment of environmental air into the updraft.

This mechanism of formation also differs significantly from the one observed in [44] and [43] in the case of JICF, where the formation process begins just downstream and to either side of the jet, with separation of the crossflow bottom boundary layer and no evident contribution of the jet air. Our results, however, do not necessarily contradict this theory: as it is highlighted by the authors in [44] and [43], a fundamental hypothesis for they results is the absence of vorticity production at the jet-crossflow interface, that occurs when the jet and crossflow have the same density (which is not our case, due to the presence of buoyancy).

Finally, the plot of the $Q = 5{\cdot}10^{-4}$ isosurface (Fig.5.8b) taken at t_0+60min, reveals the vertical development of the vortex (in blue, at $x \sim 100000\,\mathrm{m}$), which occupies the whole column from the ground to the lower part of the anvil. This is coherent with observations from ground radar, where the vortices are observed at three inclinations in PPI mode, resulting in a vertical development of the vortices that spans at least from 3 km to 10 km.

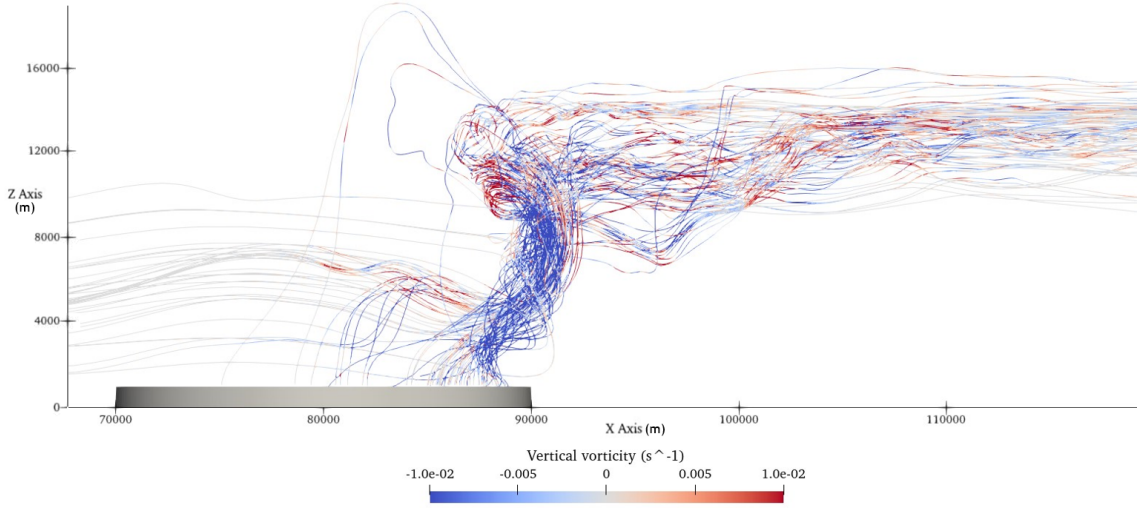

(a)

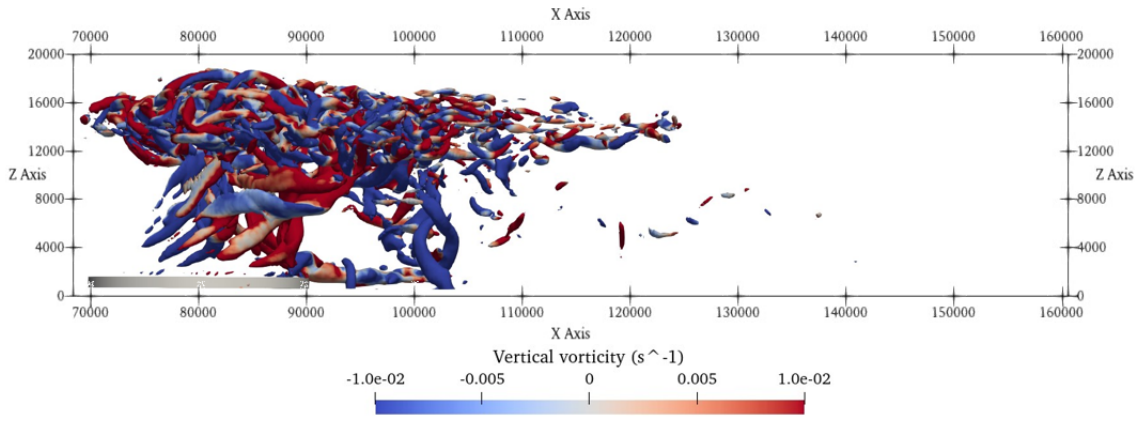

(b)

Figure 5.8: Fig.5.8a: streamlines passing through a sphere of radius 2 km located in the centre of a newly born vortex taken as example. Fig.5.8b: $Q = 5 \cdot 10^{-4}$ isosurface, colored with vertical vorticity values, showing a newly born anticyclonic vortex. In grey, the solid cylindrical nozzle on the bottom from which the updraft exits.

5.3 Shedding vortices analysis: frequency and structure

Once established the origin and the development of the simulated vortices, now we need to compute the geometrical parameters and the shedding frequency, in order to compare our results with the real Naples event. We remind that we are focusing on the vortices observed approximately from ground radar in the time window 08:00-09:00 UTC. More precisely, the quantities to compute for the vortices are:

- period T and frequency of shedding
- streamwise velocity V when advected by the cross-flow
- distance between vortices with the same sign l
- distance from the central axis h

The computation of the simulated period of shedding (T) is straightforward after the Fourier analysis performed in Section 5.1: the ratio between the time duration of the analysed period and the wavenumber corresponding to the highest peak in the power spectrum, gives the period associated with the vortex shedding. Concerning the frequency, which is defined simply as T^{-1}, it is useful however to express this quantity in terms of non-dimensional numbers, as typical of many CFD problems. In this case, we use the Strouhal number defined in Eq.3.14, therefore we need an estimation of the updraft diameter (D_u). Conversely to the non-buoyant case, where no density difference exists between the updraft and the crossflow, the updraft diameter tends to decrease with height when buoyancy is introduced, reaching a minimum at in the middle-high troposphere. Therefore, it should be incorrect to use the value of the nozzle diameter D as representative of the updraft diameter. The approach we use is to apply a time average starting from the end of the transient period, and then extract a profile of the vertical velocity over a line in spanwise direction, at $z = 7\,\text{km}$ and $x = 83.5\,\text{km}$ (3.5 km downstream the center of the nozzle, to take into account the tilt of the updraft due to the action of the crossflow). This procedure is applied with Sim.1, Sim.2 and Sim.3; in Fig.5.9 the profile obtained with Sim.1. D_u is then computed as the distance between the two y coordinates where the vertical velocity is equal to zero (dashed red lines in Fig.5.9). Firstly, it is worth noting that the updraft mean profile of vertical velocity is not coherent with expectations and previous studies with Cloud Resolving Models ([34], [73]), because the peak of vertical velocity is not located at the center of the updraft but near its borders. This is due to the gradient of buoyancy which is maximum at the borders of the updraft where the warm air interacts with the cold crossflow air, and gives rise to higher vertical velocity. To correct this effect, a more realistic buoyancy profile should be imposed at the updraft exit or the latent heat release should be considered, but this is not investigated in this thesis, and is suggested as future development.

The results of D_u estimation for the three simulations are reported in Tab.5.2; the values of the period T and Strouhal number S_t are reported in Tab.5.3 together with the other parameters corresponding to the vortices. Coherently with the theory of von Kármán-like vortices, the period increases with the increase of the diameter. The Strouhal number for all the three simulations is in good agreement with the results of Fric and Roshko [44] for the JICF, where the values of S_t are found approximately between 0.1 and 0.2 for a wide range of velocity ratio κ. The comparison with the real Naples event, however, reveals a marked difference in the period of the observed and simulated vortices, which of course affects also the Strouhal number: if the observed period is about 45min $\sim$ 2700 s, Sim.1 simulates a period which is 3.5 times longer, Sim.2 even 6.1 times longer,

Sim.3 is 2.6 times longer. The simulated periods are more similar to the results obtained for VKVS shedding from solid islands [12]. This difference from the observed event can be due to many reasons, for example the lack of many contributions in the physics of the system which are not included in the simulation. We can suppose also that the strong, unrealistic peak of vertical velocity found at the border of the updraft (Fig.5.9), could affect the mechanism of formation of the vortices explained in Section 5.2. In this perspective, a better description of the updraft borders could influence also the process of vortex formation and the period of vortex shedding.

	D_u (km)	D (km)
Sim.1	17.2	20
Sim.2	24.8	29
Sim.3	14.6	15
Real case	22 ± 3	-

Table 5.2: Estimated updraft diameter D_u compared to the nozzle diameter D for Sim.1, Sim.2, Sim.3.

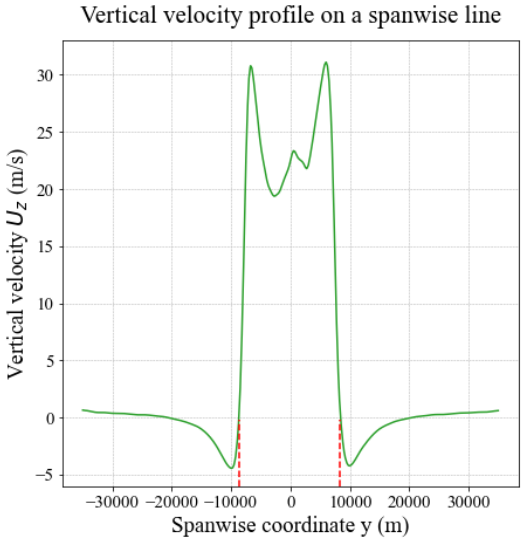

Figure 5.9: Vertical velocity profile for Sim.1 on a spanwise line at $x = 83500\,\text{m}$ and $z = 7000\,\text{m}$. Dash red lines identify the estimated updraft borders.

Now we focus on the estimation of vortices velocity V when advected by the crossflow in the updraft wake. This analysis requires the direct detection of the vortices. An algorithm can be developed to automatically detect vortices in the wake, based on the typical signatures that we discussed before (values of vertical vorticity, presence of buoyancy, vertical development, local minima of pressure, ...). Such algorithm should be trained on different simulations in order to test its validity, and it goes beyond the purposes of this thesis, therefore it is suggested as a future implementation. In this analysis, we perform a simple manual detection of the vortices on the usual plane at 7 km height: the choice of analysing the properties of the vortices on this plane only, does not imply a loss of generality, thanks to the vertical homogeneity of the vortices described with Fig.5.8b. The manual detection is done by looking at three different fields: the streamwise velocity U_x, the spanwise velocity U_y and the buoyancy b. The U_x field, in presence of a cyclonic (anticyclonic) vortex, shows a sharp transition from positive (negative) to negative (positive) values going in the y direction. An example can be found in Fig.5.7 for an anticyclonic vortex. The U_y field, in presence of a cyclonic (anticyclonic) vortex, shows a sharp transition from negative (positive) to positive (negative) values going in the y direction. The procedure is the same for Sim.1, Sim.2 and Sim.3: in order to collect a sufficient statistics, we select a time window when six vortices are produced (three cyclonic and three anticyclonic), and perform the manual detection of the center of each vortex with Paraview, using frames every 5 minutes of evolution. For each vortex, the analysis is performed starting when the vortex

has just detached from the updraft ($\sim 20\,\text{km}$ downstream), and until it reaches $\sim 80\,\text{km}$ downstream the updraft, coherently with the observations of the real case. The results are plotted in Fig.5.10 for Sim.1 as example. For Sim.2 the detection is more complicated because the vortices are less evident than in the other two cases.

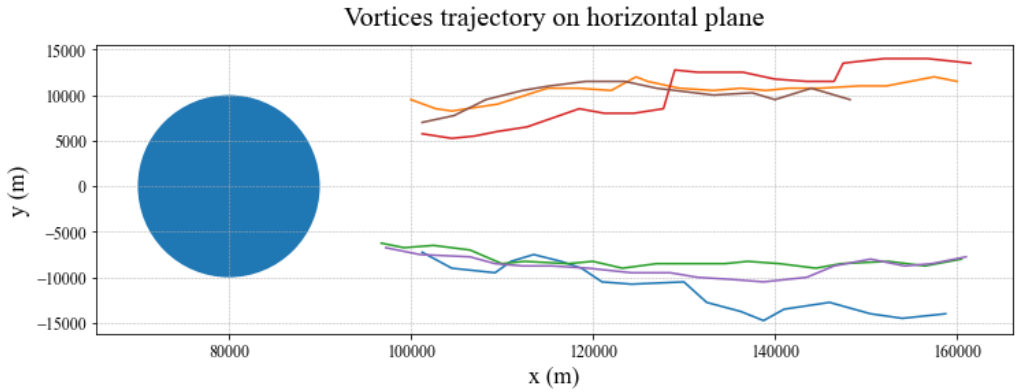

Figure 5.10: Trajectories of six vortices in Sim.1, obtained at 7 km above the ground. In blue, on the left, the position of the solid cylinder at the updraft basis.

The velocity is computed, for each vortex, as:

$$v^i = \frac{x^i - x^{i-1}}{\Delta t} \tag{5.3}$$

where $\Delta t = 300\,\text{s} = 5\,\text{min}$ and x^i is the x position of the vortex at i^{th} frame. The final estimation of vortices velocity is given by the mean of all v^i from all the different vortices, with the corresponding error of the mean. The result V is shown in Tab.5.3. The comparison with the observed value obtained from the data of Guidetti [14] reveals an overall agreement, especially for Sim.1, with a slight underestimation in all three simulations. This can be taken as a confirmation of the goodness of the crossflow estimation, which is responsible of the advection of the vortices in the wake.

Once computed the velocity V, the calculation of the distance l between vortices of the same sign is straightforward, using the value of the period T: $l = V \cdot T$. The result in Tab.5.3, obviously, shows a higher value of l compared to the observed one, due to the overestimation of T that we explained before.

	Real case	**Sim.1**	**Sim.2**	**Sim.3**
$\boldsymbol{V}$ **(m/s)**	12.6 ± 1.3	11.6 ± 0.4	10.9 ± 0.6	10.7 ± 0.3
$\boldsymbol{l}$ **(km)**	33.0 ± 1.2	109 ± 3	176 ± 10	73 ± 2
$\boldsymbol{T}$ **(min)**	44 ± 5	157	272	117
$\boldsymbol{h}$ **(km)**	9.4 ± 0.6	9.8 ± 0.2	11.5 ± 0.6	6.0 ± 0.2
$\boldsymbol{S_t}$	0.694	0.153	0.127	0.173

Table 5.3: Comparison between the vortices properties in the real case and in numerical simulations. T values in Sim.1, Sim.2, Sim.3 are not affected by error because they are estimated directly from the wavenumber of the peak in Fourier analysis, which is assumed without error.

Finally, the computation of the distance from the central axis h is again obtained as the mean of all the $|y^i|$ coordinates of the six vortices at each frame considered. The result in Sim.1 is in very good agreement with the observations of the real case, while Sim.2 and Sim.3, respectively, overestimate and underestimate the observed value. This step concludes the comparison between the simulated vortices and the observed ones; in the following, last Section the analysis of other relevant meteorological features is carried out, in order to further check the consistency of the numerical simulation with the real case study and previous analyses found in literature.

5.4 Relevant meteorological features

The comparison with the observed Naples supercell is performed by looking also at other key quantities representative of the event. One of these, the updraft diameter, has already been computed in Section 5.3 for the calculation of the Strouhal number. Furthermore, some recent studies in literature using CRM at very high resolution (e.g. [13]) have found interesting results concerning the solid-like behaviour not only of the updraft but also the overshooting top. In this context, in this Section we want to compute and investigate the following aspects:

- updraft maximum vertical velocity simulated
- overshooting top height
- hydraulic jump in the lee of the overshooting top
- vertical propagating gravity waves generated by the interaction of the overshooting top with the environmental crossflow

The analysis of these features focuses on the Sim.1 only, which has been taken as reference also for the vortex generation. The updraft maximum vertical velocity w_{max} in Sim.1 is obtained considering the simulated event after the end of the transition period, and computing through the OpenFOAM utility `cellMax` the maximum vertical velocity in each output file, written every 5 min of simulation (that results in 376 consecutive times). Then, an average of all maximum vertical velocities is computed with the corresponding error; the result is reported in Tab.5.4 together with the one estimated in Chapter 2 for the real case. The agreement is really good, even though this is not surprising since, when buoyancy has been implemented, the vertical velocity at the nozzle exit has been tuned manually in order to reproduce more accurately the value of the maximum vertical velocity, as explained in Section 3.7. Anyway, this is a positive confirmation of the goodness of our choice.

The overshooting top height is estimated from a time average of the buoyancy field starting from the end of the transient period. The location of the overshooting top is computed as the one corresponding to the coldest pixel in the simulation, which resembles the procedure emplyoed in satellite-based measurements at infrared frequency (e.g. SEVIRI). The location of the minimum of the time averaged buoyancy field is found with the `cellMin` utility, and it results in $z = 19.125 \sim 19$ km (see Tab.5.4). This value overestimates of about 3 km the one obtained from satellite observations in Marra et al. [10]. This can be partially due to the approximated vertical profile of the Brunt-Vaisala frequency imposed in the simulation, and also to the absence of drag by the hydrometeors. Another important reason can be found in the lack of water vapor and latent heat in our simulation, which simplifies a lot the dynamics of the OT.

	D_u (km)	w_{max} (m/s)	OT height H (km)
Real case	22 ± 3	67	16.25
Sim.1	17.2	67.0 ± 0.2	19.125

Table 5.4: Comparison between the updraft properties in the real case and in numerical simulation Sim.1.

The presence of the overshooting top influences strongly the dynamics of the region above the anvil. Since the top raises some kilometers (3/4) above the anvil, it represents an important obstacle to the crossflow. This results in the formation of some interesting phenomena, which are typical of the mountain chains or isolated mountains when interacting with an environmental wind under certain conditions of stability and vertical profile of the wind. In this thesis we investigate the onset of the hydraulic jump in the lee of the overshooting top, comparing the results with O'Neill et al. [13], and the generation of vertical propagating gravity waves.

Hydraulic jumps occur when fluid flows too fast for gravity waves to travel upstream, wherein the fluid becomes unstable and suddenly readjusts to a turbulent, slower flow. This is one of the processes generating strong windstorms downslope the mountain chains. As done in [13], the visualization of streamlines is useful to investigate the contributions to the formation of the jump. The analysis is performed with the time averaged fields. In Fig.5.11a we select two lines (here visible as points due to the frontal view), oriented in spanwise direction, 20 km long and centered on $y = 0$: the first one (A) is located ~ 10 km upstream the overshooting top; the second one (B) is located ~ 10 km downstream the overshooting top, almost at the same height of the anvil. On each line, 50 seed points are generated and each of them is the origin of a streamline. For line A, the streamline are computed only in the forward direction, while for line B in both forward and backward directions. In Fig.5.11b, a top view of the streamlines generated from line A, with the plot of the buoyancy in background showing the cold, negatively buoyant OT in dark green. The results show that the streamlines from A divide in two main groups:

- some upstream stratospheric air diverges around the overshooting top, as typical of isolated topographic obstacles, reconnect some km downstream (Fig.5.11b) and remains almost at the same height (see the streamlines at $z \sim 20$ km in Fig.5.11a).
- some stratospheric air above the OT's central axis acquires a negative buoyancy, accelerates and sinks downstream the top. Some of these streamlines are trapped in a recirculation just in the lee of the overshooting top: this allows the development and formation of a rotor between the anvil below and the smooth stratospheric flow above (see Fig.5.11a, above the point B). The recirculation can be seen also from the blue color of the streamlines in Fig.5.11b, indicating negative values of U_x. This behaviour is compatible with the onset of a hydraulic jump. Interesting to note how this element is observed in the time averaged field, therefore it is a stationary feature of the flow which is not filtered out by the time average.

These results are coherent with the ones found in [13]. A more detailed analysis, which is beyond the purposes of this thesis, should involve the study of breaking gravity waves through the visualization of isentropes, in order to investigate better the onset of the hydraulic jump.

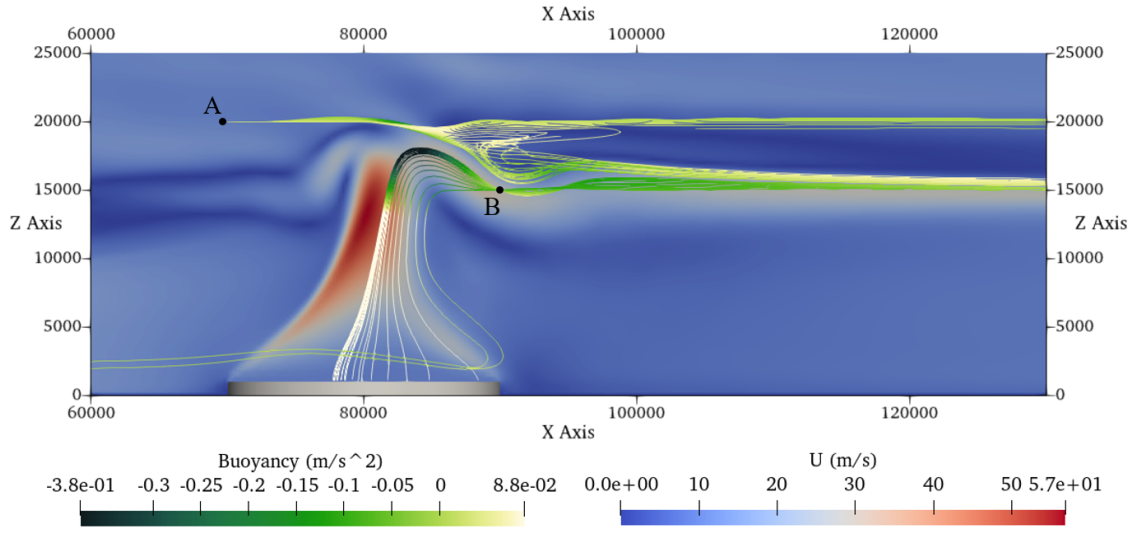

(a)

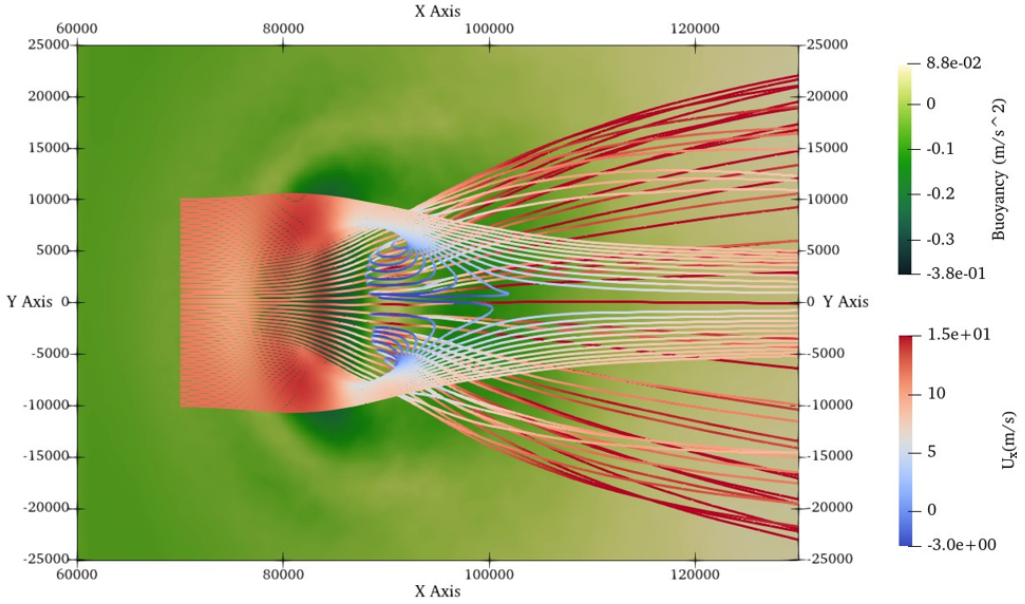

(b)

Figure 5.11: Fig.5.11a: streamlines computed from two spanwise source lines, 20 km long, centered at $y = 0$, with 50 seed points each: line A at $x = 70$ km, $z = 19$ km; line B at $x = 90$ km, $z = 15$ km. Streamlines are colored with buoyancy values, the vertical plane with velocity magnitude U. In grey the solid cylindrical nozzle. Fig.5.11b: top view of the streamlines originating from source line A, colored with values of streamwise velocity U_x. In the background, plot of the bouyancy showing the OT region.

From the streamlines passing through line B in Fig.5.11a, we observe that almost all the streamlines originate from the updraft: they start with strong positive buoyancy, then overshoot into the stratosphere, become negatively buoyant and descend downstream with high velocity. No contribution here comes from the crossflow in the stratosphere or upper troposphere. On the other hand, if point B was moved vertically of 1 km only (not shown here), which is inside the hydraulic jump observed through the streamlines from A, almost all the streamlines would have originated from the crossflow. This result reveals that: the hydraulic jump is composed for the vast majority of stratospheric air, and that the mixing

of stratospheric air with updraft air is small in this region (or if there is, it is filtered out by the time average calculation). The streamlines passing through B, perform also a weak damped oscillation visible downstream the OT: the air parcels undergo a damped oscillation after their descent from the OT and approach an equilibrium height attributable to the height of the anvil. This result is coherent with Schlesinger [74] for the case where no hydrometeors drag is considered (as it is in our simulation).

Furthermore, from Fig.5.11a two more features of the supercell storm, but in general of all the kinds of thunderstorms, are reproduced by the simulation: the anvil and the *back sheared anvil*. The former is visible at $\sim 15\,\text{km}$ height downstream the storm, as the level where the streamlines adjust to the equilibrium. The back sheared anvil is visually similar to the anvil, but it develops on the opposite side of the updraft (upstream) and has a much shorter length. It is visible under the position of point A, as a "tongue" extending from the upper levels of the updraft.

Finally, the impact of the overshooting top on the environmental flow is studied also in terms of gravity waves generation. It is widely known in meteorology that the interaction of tropospheric wind with topographic obstacles can trigger the development of internal gravity waves downstream the obstacle, known as lee waves. Wind passing over topographic obstacles receives a vertical pulse and kinetic energy is transformed into potential energy; buoyancy force is the restoring force for internal gravity waves, which tries to readjust the perturbed fluid to equilibrium. In a stable air mass, a vertically perturbed air parcel (e.g. by vertical lift in a mountain range) will have the tendency to come back to its initial position because the air parcel cools when lifted and warms up compared to the surrounding air temperature when dragged down. Therefore, a necessary, albeit not sufficient, condition for internal gravity waves to exist is the presence of a stable stratification ($N^2 > 0$). The theory of lee waves (a complete description can be found in [16]) is based on the values assumed by the *Scorer parameter* $\ell(z)$, which combines the Brunt-Vaisala frequency N with characteristics of the vertical crosswind profile U:

$$\ell^2(z) = \frac{N^2}{U^2} - \frac{1}{U}\left(\frac{d^2U}{dz^2}\right) \tag{5.4}$$

When $\ell^2(z)$ decreases strongly with height, conditions are favorable for *trapped lee waves*, that have horizontal wavelengths of 5 - 35 km and are trapped in a layer with high stability and moderate wind speeds. Trapped waves occur when wind speed above the mountain increases sharply with height and when stability decreases in the layer just above the mountain top. When $\ell^2(z)$ is nearly constant with height, conditions are favorable for *vertically propagating gravity waves*, which typically extend vertically for many km and are tilted backwards with height towards the obstacle. When $\ell^2(z)$ increases with height, the conditions are not favorable for the development of gravity waves. The Scorer parameter is useful also to obtain a simple expression for different quantities related to lee waves, such as the wavelength (the distance between two points with same phase), defined as $\lambda = 2\pi/\ell(z)$.

Here we try to investigate if the overshooting top is able to trigger vertical propagating gravity waves compatible with the ones produced by an isolated mountain after the interaction with the crossflow. The OT in fact raises about $3/4\,\text{km}$ above the anvil and has a horizontal development of $\sim 15/20\,\text{km}$, which is similar to the dimension of a high mountain. The case in our simulation is a limit situation where $\ell^2(z) = \ell^2 = N^2/U^2 = \text{const}$, therefore favorable to vertically propagating gravity waves. The plot of the time-averaged velocity field in Fig.5.12a reveals the presence of the typical pattern of vertical propagating

gravity waves above the OT, which appear as slanted, periodic bands in the velocity field. Firstly, we notice that these waves are stationary, because they are visible in the time-averaged field. Then, in order to check the similarity of these gravity waves with the ones generated by real topographic obstacles, we estimate the wavelength of the waves extracting the profile of the U_{xz} velocity along the white line in Fig.5.12a, where $U_{xz} = \sqrt{U_x^2 + U_z^2}$ is the velocity on the xz plane. This line is approximately orthogonal to the wave front and it is 28.28 km long. The result is shown in Fig.5.12b. Then a simple Fourier analysis is applied at the U_{xz} profile data in order to find the wavelength of the dominant frequency in the signal. As it can be observed also from Fig.5.12b, the dominant wavenumber is $k = 4$, which results in a wavelength equal to $\lambda_{sim} = 7.07$ km. From the theory explained above, the expected period of vertically propagating waves for topographic obstacles is $\lambda = 2\pi/\ell$, that for our case becomes $\lambda = 6.88$ km. The difference between λ and λ_{sim} is only the 2.7%, therefore the agreement is really good. We conclude that the similarity between the OT gravity waves and the theory of lee waves produced by solid topography is remarkable, at least concerning the wavelength of the waves.

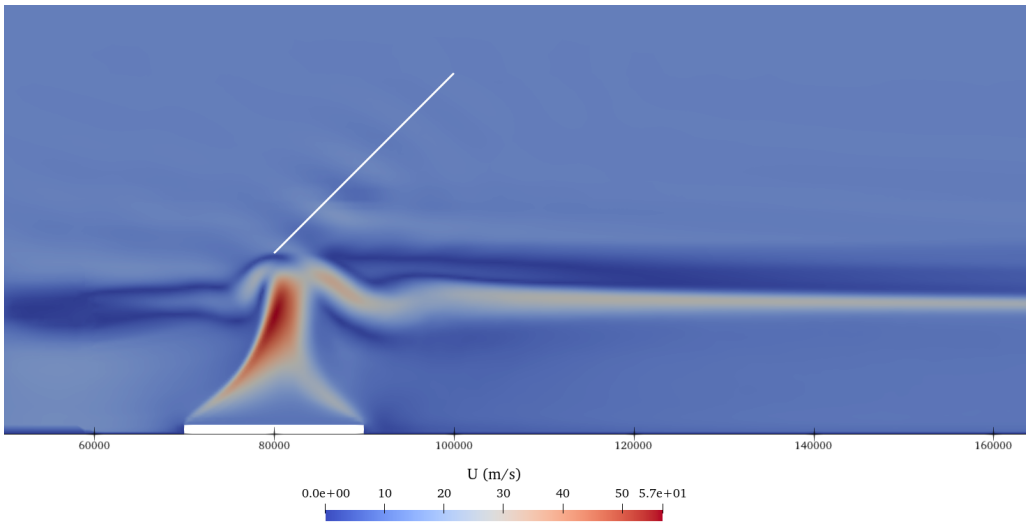

(a)

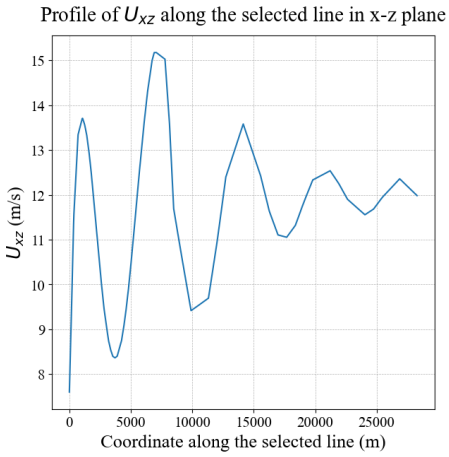

(b)

Figure 5.12: Fig.5.12a: plot of velocity magnitude U showing vertical propagating gravity waves above the overshooting top. White line indicating the selected profile where the profile of U_{xz} is extracted. Fig.5.12b: profile of U_{xz} on the white line in Fig.5.12a.

Conclusions and final remarks

This work focuses on the exceptional supercell storm that stroke the city and the Gulf of Naples on September 5th, 2015. This event, which showed extremely rare intensity for the Mediterranean area, generated an unusual shedding of vortices in the wake of the storm towards the coast in the front side of the system, resembling the pattern of a von Kármán vortex street past a solid body (e.g. a circular cylinder), although no solid obstacles are present in this case. No similar atmospheric phenomena have ever been reported in literature, making the Naples supercell a unique case study. The event is investigated with a numerical simulation in order to improve the understanding of shedding vortices, comparing the results with the observations of the real case study. This task is pursued by setting up a Large-Eddy Simulation, which is an high-resolution simulation approach and represents an application, still little used in meteorology, of high-resolution simulations to such large and complex phenomena. The simulations are performed with OpenFOAM v9 software, run on OPH cluster at Physics and Astronomy Department in Bologna.

The computational domain is centered in the center-of-mass of the supercell and simplified in its most essential elements (the vertical updraft and the environmental wind) starting from the classical problem of a buoyant jet in cross flow (BJICF), where a high thermal gradient and vertical velocity exit a tiny and wide cylindrical nozzle. Thermal stratification (buoyancy) and updraft rotation are added in a second stage as further levels of complexity. The initial and boundary conditions of the numerical simulation (namely, updraft diameter, updraft vertical velocity, crossflow velocity, updraft rotation, thermal stratification) are estimated in this work, combining information from GPM-CO GMI satellite, ground radar in Monte il Monte, Abruzzo, and ERA5 reanalysis data, starting from the work of Marra et al. [10] and Guidetti [14].

The comparison with the vortices in the real case gives the following results, obtained from simulations with a maximum spatial resolution of 250 m:

- **physical contributions:** the preliminary simulation of the jet in crossflow without thermal stratification is not sufficient to generate a regular vortex shedding as the one observed. The thermal stratification, that limits the vertical motions in the first 15/20 km of atmosphere, is crucial for the formation of vortices in the wake. The presence of a cyclonic rotation hampers the formation of regular shedding vortices in case of large updraft diameter, and favours the formation of anticyclonic vortices in the wake in case of smaller updraft diameter.

- **vortices generation:** the buoyant updraft acts as an obstacle to the crossflow, in a way similar to the solid cylinders. However, the mechanism of formation differs from the classical von Kármán vortex streets and seems to be driven by the entrainment of crossflow air into the updraft. The presence of the updraft generates recirculation vortices in its downstream flank, where both updraft and crossflow air are mixed together. The updraft then pulls upward the fluid producing a vertical velocity that

combines with the rotating motion of the recirculation vortices and gives rise to helicoidal vertical flows, that are finally advected downstream in the wake. This process is similar to the one at the basis of the counter-rotating vortex pair in the BJICF [41].

- **similarities with the real case:** a sensitivity analysis is performed by varying the nozzle diameter D: the alternation of vortices of different sign is correctly guessed; the mean distance of the vortices from the central axis (9.8 km) is compatible with the real case when the nozzle diameter is $D = 20\,\text{km}$; the vortices velocity (11/12 m/s) is well reproduced for all the values of D; the vortices display a vertical development and occupy the majority of the troposphere thickness; they persist at least until $\sim 80\,\text{km}$ from the updraft core, coherently with the observations from ground radar.
- **differences from the real case:** some features of the vortices are not well reproduced, especially the period of shedding: it coherently increases by increasing the updraft diameter, as happens for solid obstacles, but it always overestimates the real value. The best agreement is found for $D = 15\,\text{km}$ with an overestimation of the real period of 2.6 times. This brings obviously to overestimate the mean distance between vortices of the same sign. The beginning of the simulated vortex shedding (~ 3 hours) is also overestimated, if compared to the real one.

As final analyses, the output of the numerical simulations is examined also looking at other relevant features of the system. We found that the updraft diameter tends to decrease in the middle troposphere as a consequence of the entrainment, and this effect is stronger if D is larger; the updraft maximum vertical velocity is in perfect agreement with the estimations, although the peak of velocity is found at the borders and not in the core; the overshooting top (OT) height is slightly overestimated of 2/3 km, probably as a consequence of the simplifications introduced in the model (e.g. the absence of heat exchange by water change of phase). The presence of the OT also influences the region immediately downstream, above the tropopause, with the formation of a recirculation compatible with the onset of a hydraulic jump [13]. The effect of the OT of the supercell is observed also in the stratosphere where standing, vertically propagating gravity waves appear, with a wavelength in remarkable agreement with the one observed for isolated mountains, suggesting a solid-like behaviour of the overshooting top itself. The features observed are summarised in Fig.5.13.

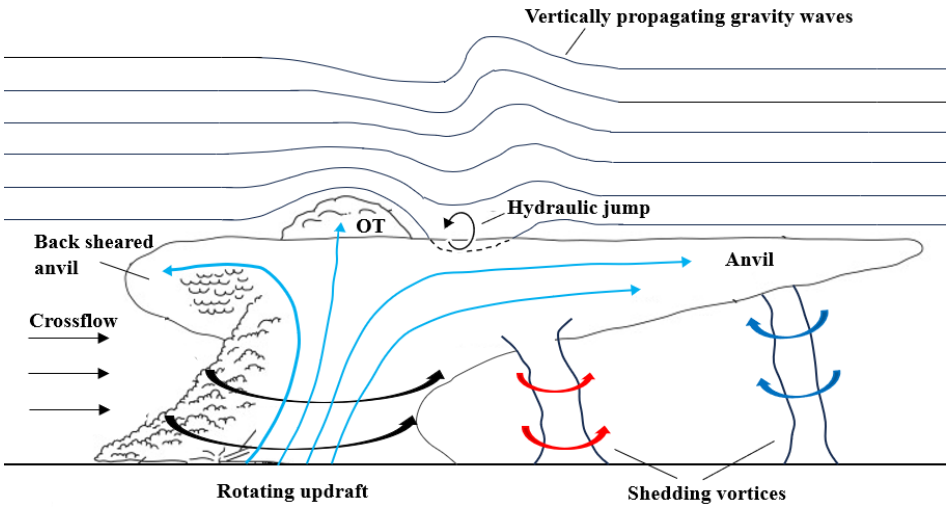

Figure 5.13: Summary of the main features reproduced by the numerical simulation.

The simplifications introduced in the simulation limit the description of the complex updraft dynamics, especially the updraft vertical velocity profile, and have some impact on the vortex generation mechanism. This leads to many possible future developments to improve the critical aspects pointed out before. In this perspective, the implementation of water vapor and latent heat into the model seems to be worth considering. Secondly, the presence of vertical wind shear in the crossflow, crucial for the development of supercell storms, can be added into the model to verify its impact on the updraft and the wake region.

The results of this thesis present the application of high resolution Large-Eddy Simulation to an extreme meteorological event and shed some light on the formation of shedding vortices past supercell storms, which still reserve unrevealed aspects to be discovered.

References

[1] Charney J.G., Fjortoft R., and von Neumann J. Numerical integration of the barotropic vorticity equation. *Tellus*, 2(4):237–254, 1950.

[2] Kolmogorov A.N. Local structure of turbulence in an incompressible viscous fluid at very high reynolds numbers. *Soviet Physics Uspekhi*, 10(6):734, 1968.

[3] Smagorinsky J. General circulation experiments with the primitive equations. *Monthly Weather Review*, 91(3):99 – 164, 1963.

[4] Lilly D.K. The representation of small scale turbulence in numerical simulation experiments. *IBM Scientific Computing Symposium on Environmental Sciences*, pages 195–210, 1967.

[5] Lilly D.K. Models of cloud-topped mixed layers under a strong inversion. *Quarterly Journal of the Royal Meteorological Society*, 94(401):292–309, 1968.

[6] Lebo Z.J. and Morrison H. Effects of horizontal and vertical grid spacing on mixing in simulated squall lines and implications for convective strength and structure. *Monthly Weather Review*, 143(11):4355 – 4375, 2015.

[7] Deardorff J.W. Preliminary results from numerical integrations of the unstable planetary boundary layer. *Journal of Atmospheric Sciences*, 27(8):1209 – 1211, 1970.

[8] Huang W. et al. Comparison of the vertical distributions of cloud properties from idealized extratropical deep convection simulations using various horizontal resolutions. *Monthly Weather Review*, 146(3):833 – 851, 2018.

[9] Khairoutdinov M.F. et al. Large-eddy simulation of maritime deep tropical convection. *Journal of Advances in Modeling Earth Systems*, 1(4), 2009.

[10] Marra A.C. et al. Observational analysis of an exceptionally intense hailstorm over the mediterranean area: Role of the gpm core observatory. *Atmospheric Research*, 192:72–90, 2017.

[11] Chopra K.P. and Hubert L.F. Mesoscale eddies in wake of islands. *Journal of Atmospheric Sciences*, 22(6):652 – 657, 1965.

[12] Horváth Á. et al. Evolution of an atmospheric kármán vortex street from high-resolution satellite winds: Guadalupe island case study. *Journal of Geophysical Research: Atmospheres*, 125(4):e2019JD032121, 2020.

[13] O'Neill M.E. et al. Hydraulic jump dynamics above supercell thunderstorms. *Science*, 373(6560):1248–1251, 2021.

[14] Guidetti L. *Observation of vortexes in thunderclouds and perspectives for their numerical modeling.* University of Bologna, Master Degree thesis, 2021.

[15] Byers H.R. and Braham R.R. Thunderstorm structure and circulation. *Journal of Atmospheric Sciences*, 5(3):71 – 86, 1948.

[16] Markowski P. and Richardson Y. *Mesoscale Meteorology in Midlatitudes.* John Wiley and Sons, 2010.

[17] Chisholm A.J. and Renick J. The kinematics of multicell and supercell alberta hailstorms, alberta hail studies, 1972, reseach council of alberta hail studies rep. 1972.

[18] Marwitz J.D. The structure and motion of severe hailstorms. part 1: Supercell storms. *Journal of Applied Meteorology and Climatology*, 11(1):166 – 179, 1972.

[19] Browning K.A. and Donaldson R.J. Airflow and structure of a tornadic storm. *Journal of Atmospheric Sciences*, 20(6):533 – 545, 1963.

[20] Fujita T. and Grandoso H. Split of a thunderstorm into anticyclonic and cyclonic storms and their motion as determined from numerical model experiments. *Journal of Atmospheric Sciences*, 25(3):416 – 439, 1968.

[21] Schlesinger R.E. A three-dimensional numerical model of an isolated deep convective cloud: preliminary results. *J. Atmos. Sci.*, 32(5):934 – 957, 1975.

[22] Schlesinger R.E. A three-dimensional numerical model of an isolated thunderstorm: Part 1. comparative experiments for variable ambient wind shear. *J. Atmos. Sci.*, 35(4):690 – 713, 1978.

[23] Schlesinger R.E. A three-dimensional numerical model of an isolated thunderstorm. part 2: Dynamics of updraft splitting and mesovortex couplet evolution. *Journal of Atmospheric Sciences*, 37(2):395 – 420, 1980.

[24] Newton C.W. and Newton H.R. Dynamical interactions between large convective clouds and environment with vertical shear. *Journal of Atmospheric Sciences*, 16(5):483 – 496, 1959.

[25] Fankhauser J.C. Thunderstorm-environment interactions determined from aircraft and radar observations. *Monthly Weather Review*, 99(3):171 – 192, 1971.

[26] Wilhelmson R. The life cycle of a thunderstorm in three dimensions. *Journal of Atmospheric Sciences*, 31(6):1629 – 1651, 1974.

[27] Klemp J.B. and Wilhelmson R.B. The simulation of three-dimensional convective storm dynamics. *Journal of Atmospheric Sciences*, 35(6):1070 – 1096, 1978.

[28] Klemp J.B. and Wilhelmson R.B. Simulations of right- and left-moving storms produced through storm splitting. *Journal of Atmospheric Sciences*, 35(6):1097 – 1110, 1978.

[29] Tripoli G.J. and Cotton W.R. The use of lce-liquid water potential temperature as a thermodynamic variable in deep atmospheric models. *Monthly Weather Review*, 109(5):1094 – 1102, 1981.

[30] Tripoli G.J. and Cotton W.R. The colorado state university three-dimensional cloud/mesoscale model-1982. part i: General theoretical framework and sensitivity experiments. *J. Rech. Atmos.*, 16:185–219, 1982.

[31] Wang P.K. Johnson D.E and Straka J.M. Numerical simulations of the 2 august 1981 ccope supercell storm with and without ice microphysics. *Journal of Applied Meteorology and Climatology*, 32(4):745 – 759, 1993.

[32] Bryan G.H. and Fritsch J.M. A benchmark simulation for moist nonhydrostatic numerical models. *Monthly Weather Review*, 130(12):2917 – 2928, 2002.

[33] Nowotarski C.J. et al. Properties of a simulated convective boundary layer in an idealized supercell thunderstorm environment. *Monthly Weather Review*, 142(11):3955 – 3976, 2014.

[34] Nowotarski C.J. et al. Supercell low-level mesocyclones in simulations with a sheared convective boundary layer. *Monthly Weather Review*, 143(1):272 – 297, 2015.

[35] Bryan G.H. et al. Resolution requirements for the simulation of deep moist convection. *Monthly Weather Review*, 131(10):2394 – 2416, 2003.

[36] Khairoutdinov M. and Randall D. High-resolution simulation of shallow-to-deep convection transition over land. *Journal of the Atmospheric Sciences*, 63(12):3421 – 3436, 2006.

[37] Kundu P.K. and Cohen I.M. *Fluid Mechanics*. Elsevier Science, 2004.

[38] Williamson C.H.K. Vortex dynamics in the cylinder wake. *Annual Review of Fluid Mechanics*, 28(1):477–539, 1996.

[39] Nunalee C. and Basu S. On the periodicity of atmospheric von kármán vortex streets. *Environmental Fluid Mechanics*, 14, 02 2014.

[40] Fischer H. et al. Mixing in inland and coastal waters. *Academic Press*, 1979.

[41] Cintolesi C. et al. Turbulent structures of buoyant jet in cross-flow studied through large-eddy simulation. *Environmental Fluid Mechanics*, 2018.

[42] Mahesh K. The interaction of jets with crossflow. *Annual Review of Fluid Mechanics*, 45(1):379–407, 2013.

[43] Kelso R.M. et al. An experimental study of round jets in cross-flow. *Journal of Fluid Mechanics*, 306:111–144, 1996.

[44] Fric T.F. and Roshko A. Vortical structure in the wake of a transverse jet. *Journal of Fluid Mechanics*, 279:1–47, 1994.

[45] Yuan L.L. et al. Large-eddy simulations of a round jet in crossflow. *Journal of Fluid Mechanics*, 379:71–104, 1999.

[46] Berg W. Gpm gmi common calibrated brightness temperatures collocated l1c 1.5 hours, 13 km v07. *Goddard Earth Sciences Data and Information Services Center (GES DISC)*, Greenbelt, MD, USA, 2022.

[47] Kalnay E. *Atmospheric Modeling, Data Assimilation and Predictability*. Cambridge University Press, 2002.

[48] Davies-Jones R.P. Discussion of measurements inside high-speed thunderstorm updrafts. *Journal of Applied Meteorology and Climatology*, 13(6):710 – 717, 1974.

[49] Marinescu P.J. et al. Updraft vertical velocity observations and uncertainties in high plains supercells using radiosondes and radars. *Monthly Weather Review*, 148(11):4435 – 4452, 2020.

[50] Adler R.F. and Fenn D.D. Thunderstorm intensity as determined from satellite data. *Journal of Applied Meteorology*, 18(4):502 – 517, 1979.

[51] Heymsfield A. and Wright R. Graupel and hail terminal velocities: Does a "supercritical" reynolds number apply? *Journal of the Atmospheric Sciences*, 71(9):3392 – 3403, 2014.

[52] Peters J. M. et al. *An analytic formula for entraining CAPE in mid-latitude storm environments.* arXiv:2301.04712, 2023.

[53] Shi J. et al. Radar-based automatic identification and quantification of weak echo regions for hail nowcasting. *Atmosphere*, 10(6), 2019.

[54] Marion G.R. et al. Using overshooting top area to discriminate potential for large, intense tornadoes. *Geophysical Research Letters*, 46(21):12520–12526, 2019.

[55] French M.M. et al. High-resolution, mobile doppler radar observations of cyclic mesocyclogenesis in a supercell. *Monthly Weather Review*, 136:4997–5016, 2008.

[56] Snyder J.C. et al. Observations of polarimetric signatures in supercells by an x-band mobile doppler radar. *Monthly Weather Review*, 141(1):3 – 29, 2013.

[57] Wang P.K. Moisture plumes above thunderstorm anvils and their contributions to cross-tropopause transport of water vapor in midlatitudes. *Journal of Geophysical Research: Atmospheres*, 108(D6), 2003.

[58] Yang Z. Large-eddy simulation: Past, present and the future. *Chinese Journal of Aeronautics*, 28(1):11–24, 2015.

[59] Lesieur M. Turbulence in fluids. Springer Science, 2012.

[60] Van Driest E.R. On turbulent flow near a wall. *Journal of the Aeronautical Sciences*, 23(11):1007–1011, 1956.

[61] Prandtl L. Führer durch die strömungslehre. pages 373–375, 1942.

[62] Greenshields C. *OpenFOAM v9 User Guide.* The OpenFOAM Foundation, London, UK, 2021.

[63] Oliveira P.J. and Issa R.I. An improved piso algorithm for the computation of buoyancy-driven flows. *Numerical Heat Transfer, Part B: Fundamentals*, 40(6):473–493, 2001.

[64] Van Leer B. Towards the ultimate conservative difference scheme. v. a second-order sequel to godunov's method. *Journal of Computational Physics*, 32(1):101–136, 1979.

[65] Jasak H. et al. High resolution nvd differencing scheme for arbitrarily unstructured meshes. *International Journal for Numerical Methods in Fluids*, 31(2):431–449, 1999.

[66] Trivellato F. and Raciti Castelli M. On the courant–friedrichs–lewy criterion of rotating grids in 2d vertical-axis wind turbine analysis. *Renewable Energy*, 62:53–62, 2014.

[67] Parello M. *High-fidelity simulation of a jet in crossflow*. Politecnico di Milano, Master Degree thesis, 2021.

[68] The engineering toolbox. air - density, specific weight and thermal expansion coefficient vs. temperature and pressure. 2003.

[69] Denev J.A. et al. Large eddy simulation of a swirling transverse jet into a crossflow with investigation of scalar transport. *Physics of Fluids*, 21(1):015101, 2009.

[70] Dubief Y. and Delcayre F. On coherent-vortex identification in turbulence. *Journal of Turbulence*, 1:N11, 2000.

[71] Benhamadouche S. and Laurence D. Les, coarse les, and transient rans comparisons on the flow across a tube bundle. *International Journal of Heat and Fluid Flow*, 24(4):470–479, 2003.

[72] Kumjian M.R. et al. The evolution of hail production in simulated supercell storms. *Journal of the Atmospheric Sciences*, 78(11):3417 – 3440, 2021.

[73] Schlesinger R.E. Mature thunderstorm cloud-top structure and dynamics: a three-dimensional numerical simulation study. *J. Atmos. Sci.*, 41(9):1551 – 1570, 1984.

[74] Schlesinger R.E. Overshooting thunderstorm cloud top dynamics as approximated by a linear lagrangian parcel model with analytic exact solutions. *J. Atmos. Sci.*, 47(8):988 – 998, 1990.